Hydro-Fractured Reservoirs:

A Study Using Double-Difference Location Techniques

by

Daniel Scott Kahn

Department of Earth and Ocean Sciences
Duke University

Date:_____

Approved:

_____
Lincoln Pratson, Co-Supervisor

_____
Peter Malin, Co-Supervisor

_____
Peter Haff

_____
Eylon Shalev

Dissertation submitted in partial fulfillment of
the requirements for the degree of Doctor
of Philosophy in the Department of
Earth and Ocean Sciences in the Graduate School
of Duke University

2008

ABSTRACT

Hydro-Fractured Reservoirs:

A Study Using Double-Difference Location Techniques

by

Daniel Scott Kahn

Department of Earth and Ocean Sciences
Duke University

Date:_____

Approved:

_____
Lincoln Pratson, Co-Supervisor

_____
Peter Malin, Co-Supervisor

_____
Peter Haff

_____
Eylon Shalev

An abstract of a dissertation submitted in partial
fulfillment of the requirements for the degree
of Doctor of Philosophy in the Department of
Earth and Ocean Sciences in the Graduate School
of Duke University

2008

Copyright by
Daniel Scott Kahn
2008

Abstract

The mapping of induced seismicity in enhanced geothermal systems presents the best tool available for understanding the resulting hydro-fractured reservoir. In this thesis, two geothermal systems are studied; one in Krafla, Iceland and the other in Basel Switzerland. The purpose of the Krafla survey was to determine the relation between water injection into the fault system and the resulting earthquakes and fluid pressure in the subsurface crack system. The epicenters obtained from analyzing the seismic data gave a set of locations that are aligned along the border of a high resistivity zone ~2500 meters below the injection well. Further magneto-telluric/seismic-data correlation was seen in the polarity of the cracks through shear wave splitting. The purpose of the Basel project was to examine the creation of a reservoir by the initial stimulation, using an injection well bored to 5000 meters. This stimulation triggered a M3.4 event, extending the normal range of event sizes commonly incurred in hydro-fractured reservoirs. To monitor the seismic activity 6 seismometer sondes were deployed at depths from 317 to 2740 meters below the ground surface. During the seven-day period over 13,000 events were recorded and approximately 3,300 located. These events were first located by single-difference techniques. Subsequently, after calculating their cross-correlation coefficients, clusters of events were relocated using a double-difference algorithm. The event locations support the existence of a narrow reservoir spreading form the injection well. Analysis of the seismic data indicates that the reservoir grew at a uniform rate

punctuated by fluctuations which occurred at times of larger events, which were perhaps caused by sudden changes in pressure. The orientation and size of the main fracture plane was found by determining focal mechanisms and locating events that were similar to the M3.4 event. To address the question of whether smaller quakes are simply larger quakes scaled down, the data set was analyzed to determine whether scaling relations held for the source parameters, including seismic moment, source dimension, stress drop, radiated energy and apparent stress. It was found that there was a breakdown in scaling for smaller quakes.

Contents

Abstract iv

List of Tables ix

List of Figures x

1.Double-Difference Locations: Theory and Applications 1

1.1 Introduction 1

1.1.1 Geothermal Energy 1

1.1.2 Locating Seismic Events 4

1.1.3 Organization 7

1.2 Double-Difference 8

1.2.1 Algorithm 8

1.2.2 Tests 12

1.3 Cross-Correlation 17

1.3.1 Description of the Calculation 17

1.3.2 Demonstration 19

1.4.1 Data acquisition 21

1.4.2 Data Overview 22

1.4.3 Cross-correlation analysis 23

1.4.4 Double-difference analysis of data 27

1.4.5 Dynamics – time evolution 32

1.5 Puna data 34

1.6 Basel Data- Cementation results 36

1.7 Conclusion 43
2. Basel Main Stimulation: Characterizing the Hydro-Fractured Reservoir 47
2.1 Introduction 47
2.2 Overview of Basel 49
2.3 Stimulation 50
2.4 Data Acquisition 52
2.5 Data Analysis 53
2.5.1 Cross-correlation 54
2.5.2 Single- to Double- Difference 57
2.6 Results 60
2.6.1 Location of events 60
2.6.2 M3.4 cluster 61
2.6.3 Time evolution of events 61
2.7 Discussion and Analysis 64
2.7.1 Reservoir size and shape 64
2.7.2 Time evolution of events 65
2.7 3 Fault Size 67
2.8 Focal Mechanisms 69
2.8.1 Procedure 69
2.8.2 Results 72
2.8.3 Discussion 73
2.9 Conclusion 73

3. Source Scaling Relations 94
3.1 Introduction 94
3.2 Source Scaling Relations 96
3.3 Brief Review of Previous Techniques 99
3.4 Basel Reservoir 101
3.4.1 Data Acquisition 101
3.4.2 Data Analysis 102
3.4.3 Results 104
3.4.4 Discussion 109
3.5 Conclusions 113
Appendix 1: Seismic Study of the Krafla Geothermal Field 127
A1.1 Project Overview 127
A1.2 Krafla Geothermal Power Plant 129
A1.3 Field Instrumentation 130
A1.4 Instrumentation set-up and maintenance 137
A1.5 Data and Preliminary Results 141
A1.6 Conclusion 149
Appendix 2: Otterbach 2 - Sonde Design 151
References 157
Biography 163

List of Tables

Table 1: Basel Station Properties 37

Table 2: Velocity Model 74

Table 3: Arrival Time Correction 74

Table 4: Focal Mechanisms 75

Table 5: Geospace GS-1 Seismometer Specifications 133

Table 6: Station Locations 139

List of Figures

Figure 1: Map view of grid events and double-difference locations 14

Figure 2: Mammoth event locations 16

Figure 3: Cross-correlation and coherence 20

Figure 4: Cross-correlation and coherence in Krafla 24

Figure 5: Signals after shift has been applied 25

Figure 6: Maximum cross-correlation between events 25

Figure 7: Location of Krafla events with connectivity lines 27

Figure 8: Double-difference locations for Krafla events 29

Figure 9: Single-difference locations for Krafla 30

Figure 10: Maximum correlations for Krafla events 31

Figure 11: Average correlations for Krafla events 32

Figure 12: Time sequence of Krafla events 34

Figure 13: Double-difference locations from Puna data 35

Figure 14: Average correlation of Puna events 36

Figure 15: Map of Basel Stations 39

Figure 16: Double-difference locations for cementation process 41

Figure 17: Sample signal from Basel cementation 42

Figure 18: Locatable events 77

Figure 19: Seismographs from OT1 and OT2. 78

Figure 20:Seismographs of events in the M3.4 cluster. 79

Figure 21: Microseism Cloud 82

Figure 22: M3.4 Cluster 84

Figure 23: Time evolution of microseism cloud. 85

Figure 24: Growth of reservoir. 86

Figure 25: Trajectory of the means of the groups. 87

Figure 26: Comparison of the injection flow rate to the reservoir "size" 87

Figure 27: Comparison of the pressure at the X-tree to the reservoir size. 88

Figure 28: Comparison of the cumulative injected fluid to the reservoir size. 88

Figure 29: Data from figure 28 with trend line subtracted 89

Figure 30: Rotated cross-section plots of M3.4 cluster. 90

Figure 31: Focal mechanism of the M3.4 event. 91

Figure 32: Beach ball focal mechanisms for selected events. 92

Figure 33: Histograms of focal mechanism parameters. 93

Figure 34: Sample fit of the velocity spectrum to the Boatwright model. 114

Figure 35: Static stress drop vs moment for th P-wave in the M3.4 cluster 115

Figure 36: Seismic moment vs source radius for the P-wave in the M3.4 cluster. 116

Figure 37: Radiated energy vs seismic moment for the P-wave in the M3.4 cluster. 117

Figure 38: Static stress drop vs seismic moment for the S-wave in the M3.4 cluster. ... 118

Figure 39: Seismic moment vs source radius for the S-wave in the M3.4 cluster 119

Figure 40: Radiated energy vs seismic moment for the S-wave in the M3.4 cluster 120

Figure 41: Static stress drop vs seismic moment for the P-wave in the full cluster. 121

Figure 42: Seismic moment vs source radius for the P-wave in the full cluster..... 122

Figure 43: Radiated energy vs seismic moment for the P-wave in the full cluster. 123

Figure 44: Static stress drop vs seismic moment for the S-wave in the full cluster. 124

Figure 45: Seismic moment vs source radius for the S-wave in the full cluster..... 125

Figure 46: Radiated energy vs seismic moment for the S-wave in the full cluster. 126

Figure 47: The GeoWatch recorder 131

Figure 48: Seismic Detector Response Curve 136

Figure 49: The anchoring assembly components..... 139

Figure 50: Electrical Connections..... 139

Figure 51: Raw data of one of the earthquake events by 6 seismometers. 144

Figure 52: The locations of the epicenters and seismometer stations..... 145

Figure 53: Cross-section of epicenter location 146

Figure 54: Equal-area projection of epicenter locations for station 28..... 147

Figure 55: Equal-area projection of epicenter locations for station 28..... 148

Figure 56: A set of rose diagrams 149

Figure 57: Theoretical response of HS-1 sensor in OT2 151

Figure 58: On axis view of housing for OT2 near end caps 154

Figure 59: On-axis view of housing for OT2 in center section 155

Figure 60: Tilt for sensor in OT2..... 155

Figure 61: Longitudinal view of housing..... 156

Chapter 1

1.Double-Difference Locations: Theory and Applications

1.1 Introduction

1.1.1 Geothermal Energy

Geothermal energy has long been a source of power in regions which are volcanically active. At those sites, hot magma sits close to the surface and is readily tapped by injecting water or brine and recovering hot pressurized water from which steam is generated to spin turbines. These sites represent rather inexpensive sources of energy, and for that reason are aggressively mined. In Iceland, for example, 87% of the heating needs and 17% of the electrical needs are supplied by geothermal sources.

In order to be economically and technically productive, it is necessary that temperatures on the order of 200C be available at depths of approximately 5000 m. Temperature gradients range from 30 C/km to 100 C/km. These parameters do not require nearby volcanic activity but are available in select regions. Preliminary studies have taken place in France, Japan, Germany, Great Britain, the United States, Australia, and Switzerland. These procedures go by a variety of names, including: Deep Heat Mining, Hot Dry Rock, Hot Wet Rock, and Enhanced Geothermal System. The studies have been promising, with energy production being pursued at several sites. An understanding of the formation highly fractured reservoirs is critical to the success of future projects.

The recovery of heat from these high temperature strata is pursued through the high-pressure injection of fluid into the rock. In order for there to be sufficient thermal contact, fractures forming narrow conduits must be opened and remain open after the release of pressure. The fractures should be at least 200 meters apart so that cooling from neighboring cracks does not occur (Tenzer, 2001). These fractures must be small enough that heat exchange is efficient and sufficiently plentiful so that only moderate pressures are required to inject and produce ample supplies of hot water. Approximately ten such fractures are needed for economic operation. The heat exchange surface area, the area "through" which the water flows, should be between 3 and 10 km^2. The target for the pressure is 40Mpa (400 atmospheres) to yield 50 liters per second to produce 30Mwatts (Tenzer, 2001). The more information about reservoir formation that is available the more likely it is that injection and production wells can be drilled efficiently.

There are several probes available to examine the formation and structure of the reservoir. Core samples, resistivity (Formation Imager (FMI)/Microscanner (FMS)), optical (Acoustic Borehole Televiewer (BHTV)), Ultrasound Borehole Imager (UBI), petrographical studies, stress measurements, wire logs, gas and fluid studies are all complementary approaches to understanding the makeup of the reservoir and surrounding rock. In addition, the opening of the fractures produces seismic signals as a result of the cracking and sliding of rock. These signals can be used to identify the location, size, structure, and stress pattern of the reservoir.

There have been numerous studies that have tried to determine the connection between water injection (or other fluid injection, such as oil) and earthquake swarms (see

for example Schulte-Theis Hartwig (1995), Brandsdóttir et al (1994), Genmo et al (1995), Healy et al (1968), and Ohtake (1974)). One such study was done in the Nojima fault zone in Japan by Tadokoro et al (2001). This fault zone had a very large earthquake in 1995, and they began injecting water into the zone in 1997 for the "healing process". Before injecting water they set up a network of seismometers throughout the area. Three unique aspects of the fault zone were observed by doing this: 1) The water-induced earthquakes were in the same zones as normal seismicity which means there is an inhomogeneity in the crust; 2) There was successive rupturing on the fault probably due to water migration in the weak fault area; 3) Low b-values of 0.6, much lower than normal earthquakes in the area, were recorded. This helps support the idea that water reduces the effective stress so that fault slip is easier, causing earthquakes.

Another prominent study took place much closer to Krafla, in the Svartsengi geothermal field in Iceland. The conclusion of Davis and Frolich (1993) was that the injection pressure into Svartsengi was insufficient to cause induced seismicity. There are now permanent seismic stations operating to monitor the local microseisms.

These studies, as well as many of the others, are based on the theories involving water injection and its ability to reduce the normal stress between plates. The initial hypothesis developed by Hubbert and Rubey (1959), suggests that increasing fluid pressure in pores decreases friction allowing plate movement. When the fluid pressure in a fault zone approaches lithostatic pressure the normal stress across the fault becomes small (Healy et al, 1968). In other words, when the magnitude of the fluid pressure approaches the weight of the rock, the fluid can give an upward force that can support the

weight of the rock, and act as a lubricant between both surfaces. This would create a situation where the fault would slip more easily.

It is of critical importance to determine the dynamics of the hydro-fractured reservoir. It is understood that the fractures which open for the flow of fluid are the result of pre-existing faults in the crust that are locked until the injection pressure opens them by lubricating the cracks. Knowing how the reservoir opens up through test injections could suggest injection locations for enhanced energy recovery. In Soultz-sous-Forets, indications of two distinct reservoirs separated by a less permeable region was found. The current study will be a step forward toward understanding the dynamics of reservoir formation.

1.1.2 Locating Seismic Events

There are a variety of techniques for determining the location of seismic events. The simplest starting point is to compare the arrival times of S- and P-waves. By measuring the time difference between the arrival times of the two phases and knowing the speeds of the phases, it is straightforward to determine the distance of the event from the receiver. With the travel times, t_p and t_s, as inputs, the distance to an event is (assuming constant velocities for the phases):

$$R = V_p * t_p = V_s * t_s \quad (1)$$

This yields,

$$t_s = (V_p/V_s) * t_p. \quad (2)$$

The time delay can be written as,

$$t_s - t_p = (V_p/V_s)*t_p - t_p = ((V_p/V_s)-1)t_p, \quad (3)$$

so

$$R = \frac{V_p (t_s - t_p)}{\left(\frac{V_p}{V_s}\right) - 1} \quad (4)$$

If the "measured" distances are given by R_i, the coordinates of the seismic stations are given by B_i , and the location of the event, which is being determined, is $S = (S_x, S_y, S_z)$, then the desired **S** minimizes:

$$\sum F_i^2(S) \equiv \sum \left[R_i - \left\{ (S_x - B_{xi})^2 + (S_y - B_{yi})^2 + (S_z - B_{zi})^2 \right\}^{1/2} \right]^2 \quad (5)$$

The location, in the least squares sense, is the best "intersection" of spheres centered on the stations with radii equal to the measured distances. This requires at least three stations which receive both phases from the event. This is a nonlinear-least-squares problem, which is most easily solved by solving an approximate linear problem, through standard inverse techniques.

This method can be improved if the velocity profile is known. Two types of 1-dimensional (vertical) models are layered structures and velocity-gradient models. In this case, the traveltime is determined by finding the ray parameter from the assumed event location and the receiver locations. The ray parameter is then used to find the travel time.

This technique is limited because of the restriction that the only events that can be located have to be identified at least four stations that receive both S- and P- waves. The amount of available data can be increased if instead of using the S-P time delay, one uses the arrival time of each phase. In this algorithm, the unknowns are the location and

origin time of the event. The arrival time minus the origin time gives the traveltime, which can be calculated from knowledge of the ray parameter. In this algorithm, the minimization is of the function,

$$\Sigma F_i^2(S) \equiv \Sigma(t_i(S)-T_i(S))^2 \equiv \Sigma\{(\textit{calculated arrival time})-(\textit{observed arrival time})\}^2 \quad (6)$$

A least-squares inversion technique which iteratively adjusts the location as well as the origin time is used for the determination of the event location. This technique gives more "intersecting spheres" to use for location and does not require the participating stations to receive both wave phases. This technique is what will be referred to as the standard, single-difference location technique.

There are several sources of error which limit the accuracy of location algorithms:

A) Arrival time measurement – Whether the arrival times are chosen manually or numerically, there are limitations from sampling rates, noise and consistent identification of the arrival.

B) Model error in the velocity structure – Inherent in the methods described is the velocity of the phases. These can be estimated from a variety of sources but are only approximately known. Furthermore, inhomogeneities can affect results.

C) Sensor Network – The placement of receivers plays an important role in the location of events. Ideally, the stations should be well spaced "around" the event.

D) Determination of Phase – The difficulty in identifying the phase of the wave being "picked" is important because different phases have different wave speeds.

Through the use of cross-correlation techniques and the use of the double-difference formulation, the first two sources of errors can be significantly reduced. In general,

arrival times are either manually or automatically picked. In either situation, errors in individual arrival time measurements contribute significantly to the errors in hypocenter location. The measurement error can be reduced if *differences* in arrival times are employed (rather than absolute times) using time-domain cross correlation and/or cross-spectra techniques. This is done by converting the arrival times into time differences between common phases of different earthquakes received at the same station. Arrival times for a set of events considered simultaneously can better constrain the relative locations between events through a double-difference routine. Because the phases of two nearby quakes traverse similar paths, their traveltime difference will not be significantly affected by model error in the velocity structure. These two techniques reduce the error from arrival and from velocity structure model error.

1.1.3 Organization

The organization of this chapter is a s follows. In Section 2, the double-difference technique is described. The tests that were performed to verify the algorithm are outlined. In Section 3, the relation of cross-correlation and coherence to double-difference techniques are described. Synthetic examples to test the algorithm are displayed and limitations of the calculations are discussed. The application of the double-difference location techniques to Krafla data set is described in Section 4 and to the Puna data set in Section 5. Application to the Basel hydro-fractured reservoir is described in section 6. Section 7 presents a discussion and conclusion.

1.2 Double-Difference

1.2.1 Algorithm

The double-difference technique gets its name because it involves the difference of observed and calculated arrival times that are then differenced for separate events. The formulation I will follow was first implemented by Waldhauser and Ellsworth (2000). To begin the discussion, I write the arrival time as the origin time plus the travel time.

$$t = \tau + \int u ds = \tau + T \tag{7}$$

Here τ is the time of origin of the earthquake and u (=1/v) is the slowness which is integrated over the path. T is defined as the traveltime. Since the traveltime has a nonlinear dependence on the event location a truncated Taylor series is commonly used to linearize the equation:

$$\Delta m \cdot \frac{\partial T}{\partial m} + \Delta m \cdot \frac{\partial \tau}{\partial m} = \Delta m \cdot \frac{\partial t}{\partial m} \tag{8}$$

Here m is a vector describing the earthquake location (x,y,z,τ) and origin time, $\Delta\mathbf{m}=(\Delta x,\Delta y,\Delta z,\Delta\tau)$.

The difference between the observed and the theoretical (calculated) arrival time for event i received at station k is given by:

$r^i_k = (t^{obs}-t^{cal})^i_k =$

$$r_k^i = \Delta m^i \cdot \frac{\partial \tau}{\partial m} + \Delta m^i \cdot \frac{\partial T}{\partial m} = \Delta \tau^i \cdot \frac{\partial \tau}{\partial \tau} + \left(\Delta x^i \cdot \frac{\partial T_k^i}{\partial x} + \Delta y^i \cdot \frac{\partial T_k^i}{\partial y} + \Delta z^i \cdot \frac{\partial T_k^i}{\partial z} \right) \equiv \left(\frac{\partial t_k^i}{\partial m} \right) \cdot (\Delta m^i)$$

(9)

Recall that τ is the origin time which does not depend on x,y,z, but only on τ, and the traveltime, T, is independent of the time of origin.

The double difference is defined by (Waldhauser & Ellsworth, 2000):

$$dr_k^{ij} = (t_k^i - t_k^j)^{obs} - (t_k^i - t_k^j)^{cal} \tag{10}$$

Therefore, the following equation is the linearized double-difference of arrival times,

$$\frac{\partial t_k^i}{\partial m} \Delta m^i - \frac{\partial t_k^j}{\partial m} \Delta m^j = dr_k^{ij} \tag{11}$$

where m is the x,y,z, and τ at the origin and t is the arrival time, based on a velocity model.

This can be written in matrix form, which for 4 events and one station k is given in brief below. (The z and Δτ derivatives for four events has been deleted because of space constraints). There are 4N columns (where N is the number of events) and M rows (where M is the number of event-pairs). It should be noted that seldom, if ever, do all stations record all of the events, so the size of the actual matrix must be adjusted for each circumstance.

$$\begin{pmatrix} \frac{\partial t_k^1}{\partial x} & -\frac{\partial t_k^2}{\partial x} & 0 & 0 & \frac{\partial t_k^1}{\partial y} & -\frac{\partial t_k^2}{\partial y} & 0 & 0 \\ \frac{\partial t_k^1}{\partial x} & 0 & -\frac{\partial t_k^3}{\partial x} & 0 & \frac{\partial t_k^1}{\partial y} & 0 & -\frac{\partial t_k^3}{\partial y} & 0 \\ \frac{\partial t_k^1}{\partial x} & 0 & 0 & \frac{\partial t_k^4}{\partial x} & \frac{\partial t_k^1}{\partial y} & 0 & 0 & -\frac{\partial t_k^4}{\partial y} \\ 0 & \frac{\partial t_k^2}{\partial x} & -\frac{\partial t_k^3}{\partial x} & 0 & 0 & \frac{\partial t_k^2}{\partial y} & -\frac{\partial t_k^3}{\partial y} & 0 \\ 0 & \frac{\partial t_k^2}{\partial x} & 0 & \frac{\partial t_k^4}{\partial x} & 0 & \frac{\partial t_k^2}{\partial y} & 0 & -\frac{\partial t_k^4}{\partial y} \\ 0 & 0 & \frac{\partial t_k^3}{\partial x} & -\frac{\partial t_k^4}{\partial x} & 0 & 0 & \frac{\partial t_k^3}{\partial y} & -\frac{\partial t_k^4}{\partial y} \end{pmatrix} \begin{bmatrix} \Delta x_1 \\ \Delta x_2 \\ \Delta x_3 \\ \Delta x_4 \\ \Delta y_1 \\ \Delta y_2 \\ \Delta y_3 \\ \Delta y_4 \end{bmatrix} = dr_k^{ij} \quad (12)$$

$\frac{\partial t_k^1}{\partial x}$ type derivatives are the changes in travel times with change in x, y, z and are calculated numerically.

If I label the matrix **G**, the vector $\Delta\mathbf{m}$, and the double differences **dr(m)**, then the equation to solve for m is

$$G(\Delta m) = dr(m) \quad (13)$$

The solution for Δm, which minimizes the square of the residual, $(G\,\Delta m - dr(m))^2$, is found through standard inverse techniques. Symbolically, the solution for Δm is given by,

$$\Delta m = \left(G^T G\right)^{-1} G^T dr(m) \quad (14)$$

The new values for $\mathbf{m_{S+1}=m_S+\Delta m}$ and is iterated until the change in the residual is below a fixed tolerance (tol=1e-6 seconds).

The double difference not only gives relative positions, but has been shown to yield absolute positions if noise is limited (Waldhauser & Ellsworth, 2000).

The inversion technique has several practical difficulties. The first of these is that the resulting matrix is sparse. In each row only 8 of the 4N elements (where N is the number of events) are non-zero. This can lead to instabilities in the solutions. The stability of the result was enhanced by using a routine by Page and Saunders (1982) for sparse linear equations and sparse least squares. This routine regularizes the matrix by using a damping factor, whose value was determined by a compromise between speed and precision. A damping factor of zero would take full steps between iterations, while a damping of nearly one takes very much smaller steps. A damping of 10^{-6} proved to be a reasonable compromise.

The size of the matrix also can give problems, depending on the number of events and stations. In many cases, stations do not receive all phases of the events and so rows of zeros appear. To reduce the size of the matrix and to eliminate unnecessary rows, a separate matrix which keeps track of which station receives which event was created. The double-difference matrix is then collapsed to include only needed rows.

While the double-difference algorithm has proven to be a powerful means of finding event locations, it does have limitations and drawbacks. Compared to the standard routine, the double-difference algorithm is slow. The standard routine calculates locations one event at a time and, for 40 stations, it might take up to 30 seconds (for 20 iterations) per event. In the double difference routine, all event locations in the cluster are calculated simultaneously. For 20 iterations, a 64 event cluster can take two hours (depending on how many signals are received). Moreover, the number of iterations is determined by the "weakest link", while in the standard routine better defined events will

have fewer iterations. The Stanford group using a Spark workstation at 300 MHz can do inversions of a million signals at 5 minutes per iteration (Waldhauser & Ellsworth, 2000).

It is important to recognize that the double difference technique reliably gives only relative positions of the events. This occurs since only differences of arrival times are used. It is therefore important to have some means of orienting the cluster once it is determined. This can be done through the use of known events or by using an absolute location routine to identify the most certain event locations, in terms of uncertainty ellipsoids, as anchor points.

1.2.2 Tests

The first test was to determine whether the code would work on ideal data. Synthetic arrival times were prepared (5 events) and varying initial event locations were selected. The code was able to locate the events with better than centimeter accuracy when the starting point was within a range of approximately 2 kilometers of the actual location. At distances further than that, the relative position of the events was correct (a straight line, for example), but the absolute positions became less accurate.

The next step was to use a different model velocity structure in the double-difference code than was used to compute the arrival times. This would simulate modeling error. With increased "error" (up to 10% in the velocity gradient) the absolute positions moved, but again the relative positions were relatively stable (~10 meters). The same result occurred when a random arrival-time error was included (maximum

magnitude 0.005s); however, the positions became less accurate as the random error increased. For an error of 0.05 seconds, the relative positions had inaccuracies ~50m.

The algorithm was then used to locate sites on a grid of 6x6x12 with a spacing of 300m. The arrival times were calculated at each of ten stations (a subset of stations from the Mammoth data set below). Since this "cluster" is larger than memory of the current computer would accommodate, the cluster was broken into sub-clusters of varying sizes: 8,16, and 32. Each sub-cluster, has one event in common with a neighboring sub-cluster, and all events is the sub-cluster are shifted so the common event has the same position in both calculations. This procedure is carried out because the double-difference technique gives relative but not absolute positions and this shifting keeps the positions of the sub-clusters self-consistent. The positions of the calculated "events" were within 20 meters of the synthetic events (see Figure 1). If the velocity model is changed by 10% between the calculation of the arrival times and the calculation of the event locations, the maximum error in the locations increased to approximately 30 meters.

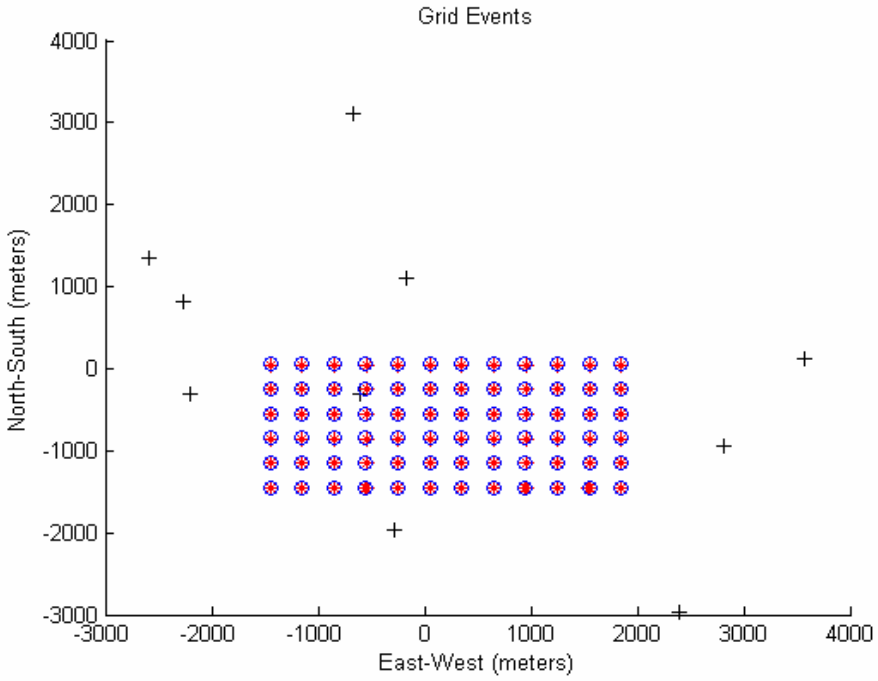

Figure 1: Map view of grid events and double-difference locations
The arrival times were calculated at the stations (+) for the events (o). The double-difference locations are shown for all six layers as (*).

A different model velocity structure was then used in the double-difference code than that which was used to compute the arrival times. The gradient term, c, in the velocity V=Vo+cz was changed by 20%. This would simulate modeling error. With increased "error" the absolute positions moved, but again the relative positions were relatively stable (~10 meters). The same result occurred when a random arrival-time error was included (maximum magnitude 0.005s); however, the positions became less accurate as the random error increased. For an error of 0.05 seconds, the relative positions had inaccuracies ~100m and the overall grid shape was lost.

The double-difference code was also tested on data acquired from the studies in Mammoth, California. Since I did not have access to the raw data and could not

determine similarity, I used all events that were recorded. The data had arrival times with a precision of 0.01 seconds and station locations given with a precision of 10 meters. There were 42 stations yielding results. Furthermore, I had no knowledge of the velocity structure and used our "Iceland" locator program (using a linear gradient model) to estimate a reasonable P-wave velocity. I used two sets of initial conditions, a) the initial event sites were selected from my single-difference locator program, and b) the same initial event site was chosen for all events in the vicinity of the anticipated location. Both sets of initial conditions gave similar relative positions, but shifts in absolute positions were on the order of 100 meters. After using the double-difference routine to calculate the relative positions, the center of the cluster was compared to the center of Stanford's cluster and a shift of approximately 250 meters was used to equate the two centers. The results of the double-difference code were surprisingly good considering the limitations on arrival times, station locations and velocity structure. The standard deviation of the residual was ~0.025s. The absolute and relative locations are a major improvement over the "Iceland" single-difference routine I wrote and show good consistency with Stanford's double-difference site location for this data (Figure 2). I also varied the velocity structure, as above, and the relative event locations were stable.

To test whether Duke's double-difference routine would be useful in the Basel HDR Project, I reduced the number of receiving stations to 4 (from 42) and searched for locations. The absolute positions suffered the most, while the relative positions showed less deterioration. The difficulty here was that many pairs of quakes had identical time differences (using only 0.01 second resolution) and therefore did not contribute to the

location. In fact, when I tried this program with only two stations, only two of seven test locations were found because all of the other time differences were identical. From this I estimate that the double-difference algorithm can collapse the sites from a good locator program and the use of cross-correlation/coherence routine to actual fracture sites with an accuracy on the order of tens of meters.

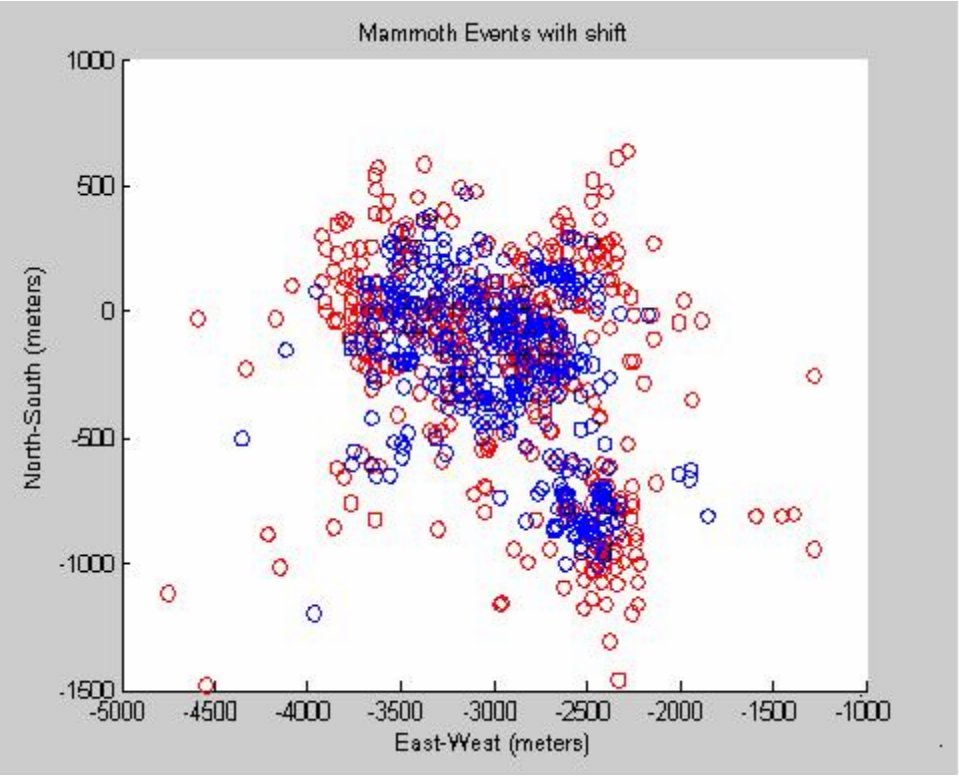

Figure 2: Mammoth event locations
Comparison of Mammoth locations found from Stanford's double-difference algorithm (blue) and Duke's double-difference algorithm (red). Events were shifted so that the centers of the two clusters agreed.

1.3 Cross-Correlation

1.3.1 Description of the Calculation

The time domain cross correlation is defined by

$$c(\tau) = n\int u_1(t)u_2(t+\tau)dt \tag{15}$$

Where u_1 and u_2 are two seismograms arriving at the same station from two different events. n is the normalization,

$$n = \frac{1}{\left(\int u_1(t)u_1(t)dt \int u_2(t)u_2(t)dt\right)^{1/2}} \tag{16}$$

When scanning over values of τ, the maximum value of $c(\tau)=C_c$ is called the correlation coefficient and the corresponding τ is the delay between the two seismograms.

The Fourier transform of $c(\tau)$ is equivalent to the cross spectrum.

$$C(f) = \mathfrak{F}[c(\tau)] ==n<U_i^*(f)U_j(f)> \tag{17}$$

Here U_1 and U_2 are the Fourier Transforms of u_1 and u_2, respectively. The absolute amplitude $|C(f)|$, after smoothing across nearby frequencies is called the coherence, m_{coh} (Schaff *et al*, 2004). In practice, I used a routine to calculate the magnitude-squared coherence, which varies from 0 to 1 and indicates how well two signals correspond at each frequency. This can be written in terms of the power spectral density P_{ij}, which is a measure of the distribution of the signal power as a function of frequency.

$$|C(f)|^2 = \frac{|P_{ij}(f)|^2}{P_{ii}(f)P_{jj}(f)} \tag{18}$$

where,

$$P_{ij} = \left\langle U_i^*(f) U_j(f) \right\rangle \tag{19}$$

is the cross power spectral density.

To measure the arrival time differences by cross-correlation requires a time frame window around the event. This can be accomplished manually, automatically, or theoretically. In the current case, a window centered at the triggered arrival time was used.

The similarity of two events is determined the cross correlation coefficient, C_c, or in the frequency domain the mean coherence, m_{coh} (the average coherence over a frequency range 2-12Hz). The coherence is a measure of how well signals correspond at different frequencies. Two events are considered similar when C_C>70% and m_{coh} > 90% (Schaff *et al*, 2004). That is, for those values, the events are considered connected in the double-difference sense. The similarity measure can be used to weight the various event pairs in the double-difference code so that more highly connected pairs will be more significant in the calculation of the hypocenter. It turns out that C_c is considered a better indicator of similarity than the coherence (Schaff *et al*, 2004). By using well-connected events, time differences more precise than the sampling rate can be obtained.

There are practical limits to the use of correlation techniques. The first of these limitations stems from the signal-to-noise ratio. When there is sufficient noise, the correlation becomes difficult to measure. This is particularly challenging when the seismometers are surface units rather than isolated in boreholes. If the noise is of high frequency, then a low-pass filter can be used to eliminate much of its effect. In the current correlation program, a Butterworth low-pass filter of order n=9 and a cutoff

frequency of 30 Hz was used. This filtering resulted in higher correlation and more accurate lag times.

The other difficulty is the separation of S- and P- phases. If the window used to evaluate the correlation includes both phases, then the correlation will be lower because a) the waves have different frequencies and b) the delay time from the P-wave to the S-wave will be different for different stations. As a result, the correlation, which is a measure of the similarity of the waves will be restricted. It is, therefore, of great importance to use windows which avoid including both phases. Two windowing programs are being used in our applications. (a) A trigger program, which uses a moving average calculation, identifies the onset of the signal and a window of ~0.5 seconds is used for the correlation. This technique can be used for P-wave correlations. (b) A widow surrounding the maximum amplitude point is created. This technique is most useful for S-wave correlations.

1.3.2 Demonstration

I have developed a program to calculate the cross-correlation and the coherence using signal processing routines in MATLAB. In the example below, I have used as input two signals $\sin(0.01\pi t)/(0.01\pi t)$ with a shift of 237 ms between them. With t in milliseconds, this corresponds to a frequency of approximately 5 Hz. The random noise has a maximum amplitude of 0.3. The cross-correlation shows a peak at 237ms, the offset between the signals (with no noise, the peak is 1). The coherence has a value of nearly 1

(exactly 1 in the absence of noise) in the window (2-12 Hz). In both cases, cross-correlation and coherence, the criteria for similarity are met (see Figure 3).

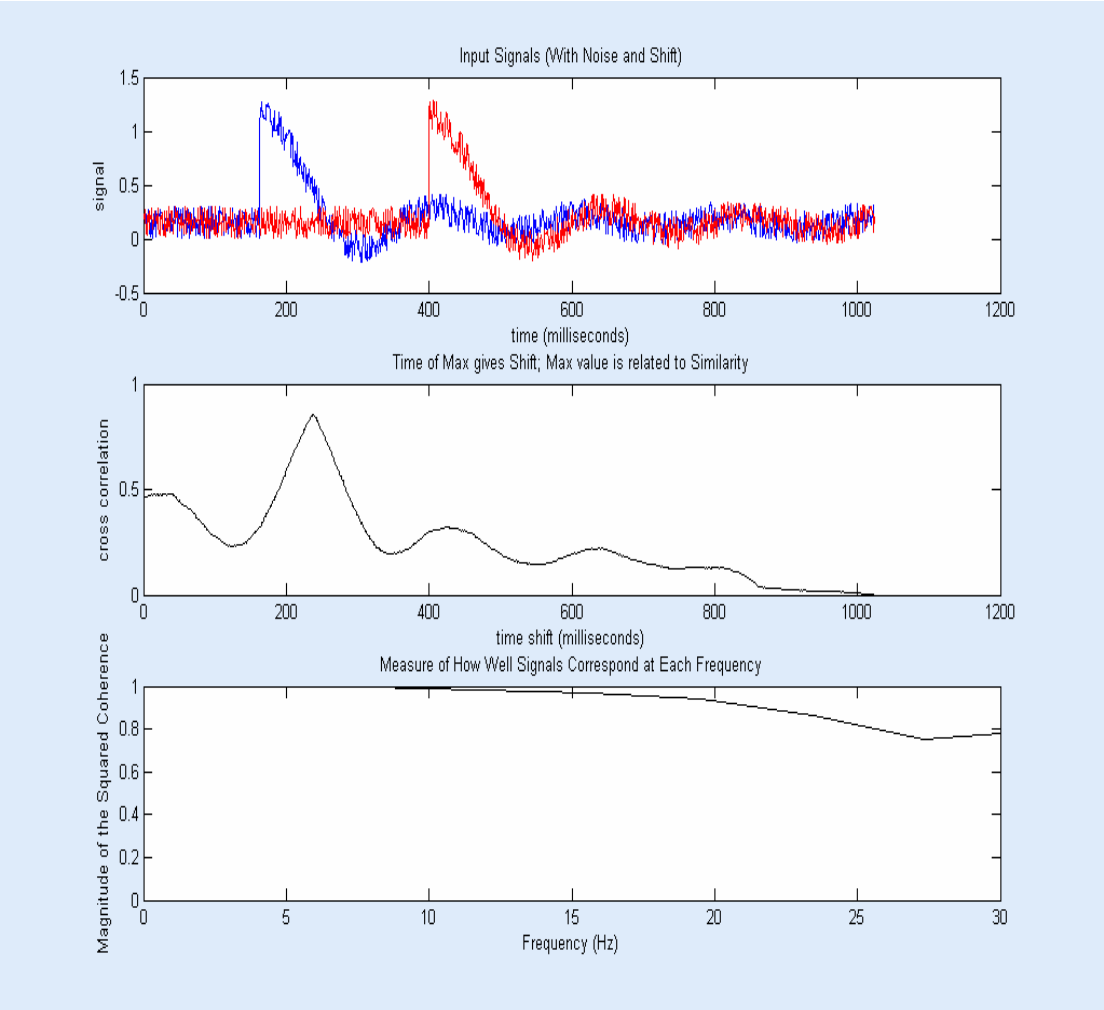

Figure 3: Cross-correlation and coherence
(a) Two signals with noise shifted by 237 ms. (b) Cross-correlation calculation showing peak at 237 ms. (c) Magnitude of the squared coherence as a function of frequency.

1.4. Krafla Data Set

1.4.1 Data acquisition

Iceland is an island country which straddles the mid-Atlantic spreading ridge, so that part of the island is on the North American Plate and part of it is on the Eurasian plate. Iceland is literally being torn apart as the plates separate. The separation is especially evident around Krafla, the site of this study, where displacements caused by rifting totaled almost seven meters between 1975 and 1984. New fissures appear and existing cracks continually widen, while magma occasionally breaks through during volcanic activity. Microearthquakes are commonplace. Therefore, the geography of this region is constantly changing.

A hotspot is also associated with Iceland giving the country access to a large amount of potential geothermal energy from the large magma reservoir below. This energy is extracted using geothermal power stations, which pump relatively cool water into the hotter subterranean regions using injection wells. The water returns as steam, which drives the power stations' turbines and generates electrical power. The water injection controls the amount of steam produced due to the fact it is the dominant source of water flux into the magma source. This water injection however is thought to control another phenomenon, earthquakes.

As part of a joint project between the University of North Carolina, Duke University, and the Krafla Geothermal Power Station, an array of twenty Geospace GS-1 sensors along with an array of twenty PASSCAL L-28 4.5-Hz sensors were placed in a 25km^2 area within the Krafla power station grounds. The positions of the seismometers

were based on the proximity to the power plant's injection well, accessibility, and isolation from noise. The seismic network set up in the Krafla geothermal power plant area was done for the purpose of examining the injection wells influence on the micro-earthquakes in the area, and the reaction of the highly faulted and cracked surface to the fluid pressure induced by the geothermal power plant.

The data from the Geospace GS-1 seismometers were used to determine the location of the epicenters through analysis of the P-wave and S-wave arrival times. The traces, corresponding to the two transverse directions of the S-wave and the longitudinal P-wave, are recorded on the tri-axis system. Data from the twenty seismometers, gathered over the 14-day span, were inspected, and the signatures of likely events were handpicked. Events observed at more than four stations were evaluated and the epicenters determined. Approximately four micro-earthquakes were observed per day, with somewhat fewer occurring when the injection well was not operational.

1.4.2 Data Overview

The locations were determined through the single-difference location program. Several deductions can be made from this analysis. The clustering of the microseisms suggests a fault line or series of cracks lie along a northeast direction, approximately 38° counter-clockwise from due north. Their locations in the near vicinity of the injection well, along with the temporal correlation of the microseisms with the injection of water, are evidence supporting the causal relation between water injection and seismic activity. The depth of these epicenters at approximately 2500 meters is consistent with the MT

data, which shows the border of high resistivity at this depth along the line. Not only is the depth correlated with the MT data, but the general curved shape (concave downward) is replicated in the MT data. This is indicative of the dome of hotter material at this depth.

1.4.3 Cross-correlation analysis

In order to proceed with the double-difference analysis on the Krafla data set, it is beneficial to identify those events which are similar. The double-difference algorithm assumes that the paths taken by the acoustic signals are sufficiently similar that differences arising from inaccuracies in the velocity structure will cancel. By performing cross-correlation analysis, the similarity of the waveforms can be determined. To accomplish this, the cross-correlation and coherence of the signals received at all stations were calculated. Figure 4 shows two sample waveforms and the resulting cross-correlation and coherence. The waveforms shifted by the lag time are displayed in Figure 5. The maximum value of the cross-correlation between events (over all stations) was used to determine the similarity of events. Those events which had a maximum cross-correlation of 0.7 or greater were considered similar and analyzed as a cluster in the double-difference analysis. From the original 67 events only 57 were found to be similar. This correlation is displayed in a matrix representation, where the rows and columns represent the events and the value of the element can be either the average correlation or the maximum correlation. Figure 6 shows a 3-D view of the matrix elements. Note, to avoid duplication only half the elements are displayed, the rest would be a mirror image

of those shown. This representation suggests an even distribution of correlations. That is, there is no evident pattern indicating that events occurring at similar times have a greater correlation than those occurring at greatly differing times.

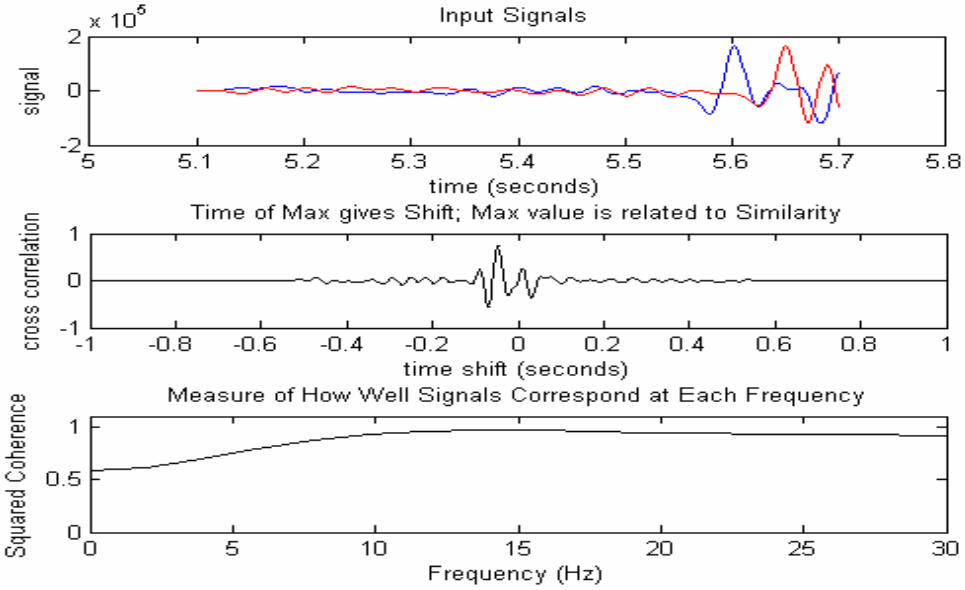

Figure 4: Cross-correlation and coherence in Krafla
(a) Sample input signals from Krafla data set. (b) Cross-correlation showing lag time for maximum at –0.46 seconds. (c) Squared coherence for the two signals.

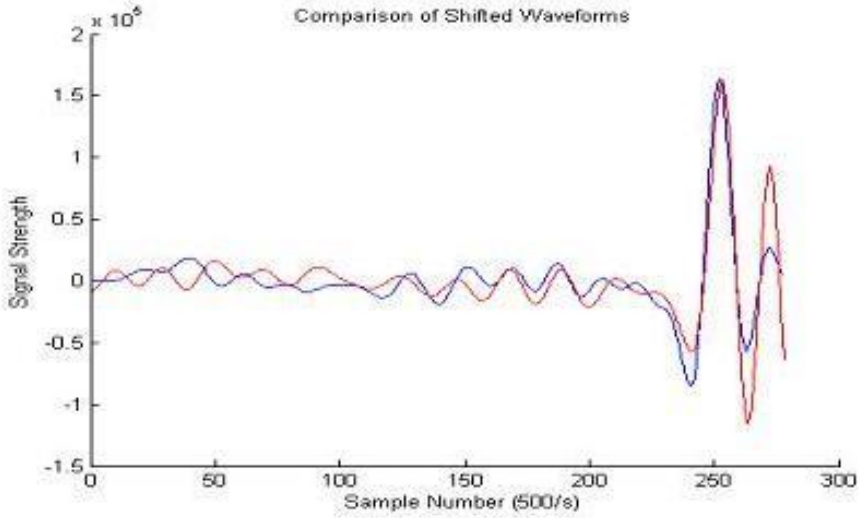

Figure 5: Signals after shift has been applied

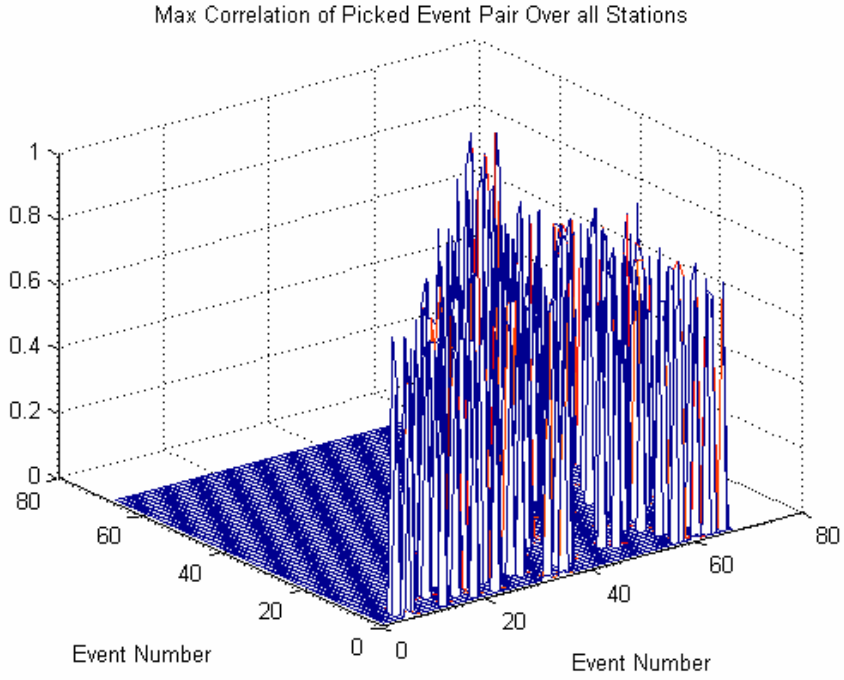

Figure 6: Maximum cross-correlation between events
The maximum is found by comparing the signals received at all stations receiving the two events.

A connectivity analysis was also performed to visualize which of the events were most highly connected. In this analysis, the number of stations which have a cross-correlation above a given threshold are counted. While the pattern of connections in Figure 7 does not appear to reveal any information about the fracture orientation, it does indicate that the correlations are not limited by distance. There are strong connections (large number of stations showing cross-correlations greater than 0.7) between events that are at opposite ends of the reservoir.

It will be seen below that the correlation between two events is related to the causes of the events. Two events originating on the same fracture have a higher correlation.

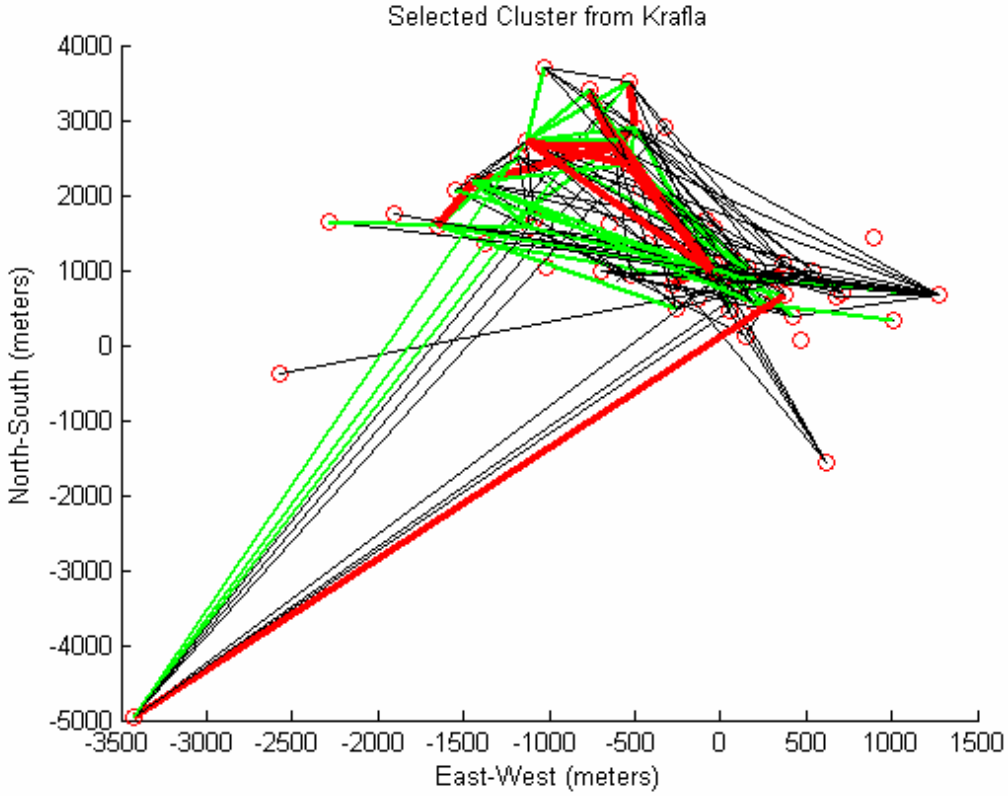

Figure 7: Location of Krafla events with connectivity lines.
The thicker lines (red) correspond to correlations greater than .85. The thinner lines (green) correspond to correlations between 0.8 and 0.85. The thinnest lines represent correlations between 0.7 and 0.8.

1.4.4 Double-difference analysis of data

The double difference algorithm was then applied to the events which were linked by a cross-correlation greater than 0.7. The initial estimate of the event locations was taken from the single-difference location program. This usage has several advantages. The number of iterations required to determine the double-difference locations is decreased compared to a calculation where a single starting point is used for all events. The absolute position appears better when the initial location was taken from the single-

difference locator when compared to MT data. Finally, events in which there is an error in the "pick times" can be spotted and eliminated from the calculation. For example, there were events which had a strong cross-correlation with other events but could not be located because of inconsistencies in timing. These events were eliminated from the double-difference calculation.

The connected events were grouped in several ways. In straight-forward calculation, all 57 events were treated simultaneously as one cluster. This has the advantage of locating the relative positions of all sites with respect to each other. The disadvantage is that as the number of events increases memory requirements increase with the cube of the number of events. The number of columns is a linear function of the number of events and the number of rows which depends on the number of event pairs is quadratic in the number of events. For larger clusters, this could become prohibitive. In anticipation of larger clusters, the calculation was broken up into smaller groupings. In this calculation, the groupings were set to 8, 16, or 32. The double-difference relative locations were calculated for each group; however, each group contained an event from another group, and the results were shifted so that common events occurred at the same location. The effect of group size did not have a significant impact on the relative positions (less than 20 meters), suggesting that for larger clusters memory constraints can be managed by choosing an appropriate group size.

The results of the double difference are displayed in Figure 8. Compared to the standard location routine (Figure 9), there is a marked collapse onto two fracture directions. This can be seen in the map plot where the two fractures are seen as east-west

and at an angle of 38 degrees along the NE. The stem plots (Figures 10 and 11) show the two fractures in terms of the average cross-correlation of an event with all other events. Again the intersection of the two fracture lines is evident. Events located away from these fracture lines have a much lower cross-correlation. This reinforces the previous suggestion that the cross-correlation is not related so much to absolute separation of events or the timing of the events, but is determined by the nature of the origin of the event.

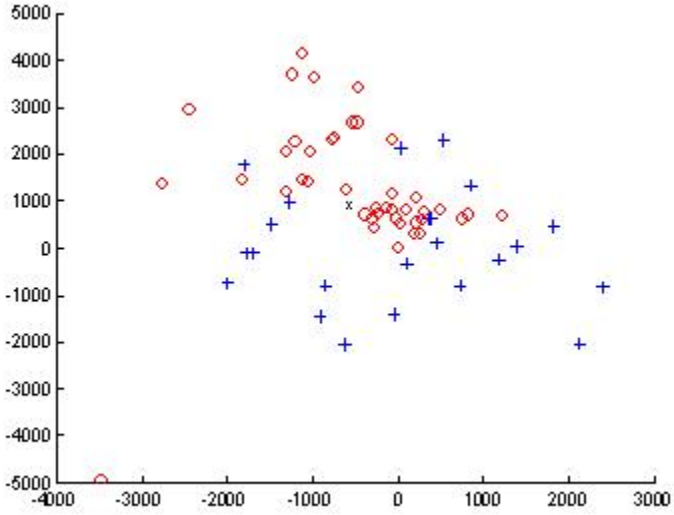

Figure 8: Double-difference locations for Krafla events
The double-difference locations are shown in red with station locations represented by +'s.

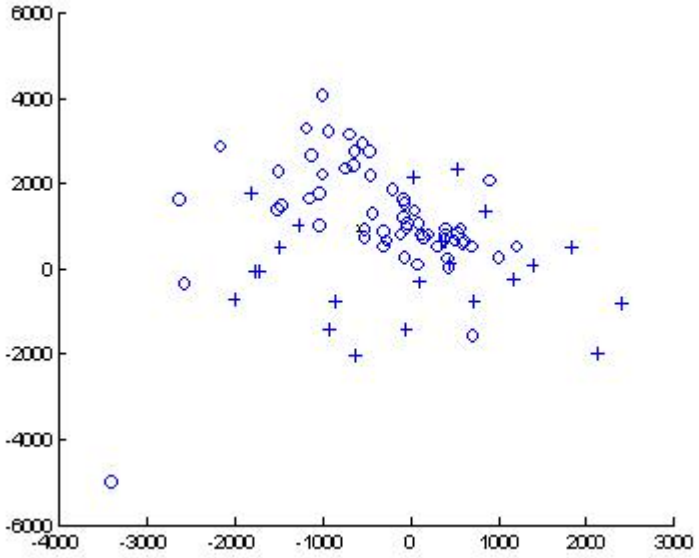

Figure 9: Single-difference locations for Krafla
The single-difference locations are shown in blue with station locations represented by +'s.

These results are consistent with MT data, which not only indicated a boundary between high and low resistivity regions, but also indicated two main fractures. Previously, we found that the depth profile of the event locations was consistent with the high/low resistance boundary. With the double-difference locations, when the cross-section is aligned along the fractures, the resistive boundary and the event locations line up more closely. This suggests that the fractures are real features and not artifacts of the calculation.

The correlation associated with the event sites is displayed in Figures 10 and 11. In Figure 10, the correlation of each event is found with all other events and all other stations. The maximum is plotted. In Figure 11, the average value of all the correlations is displayed.

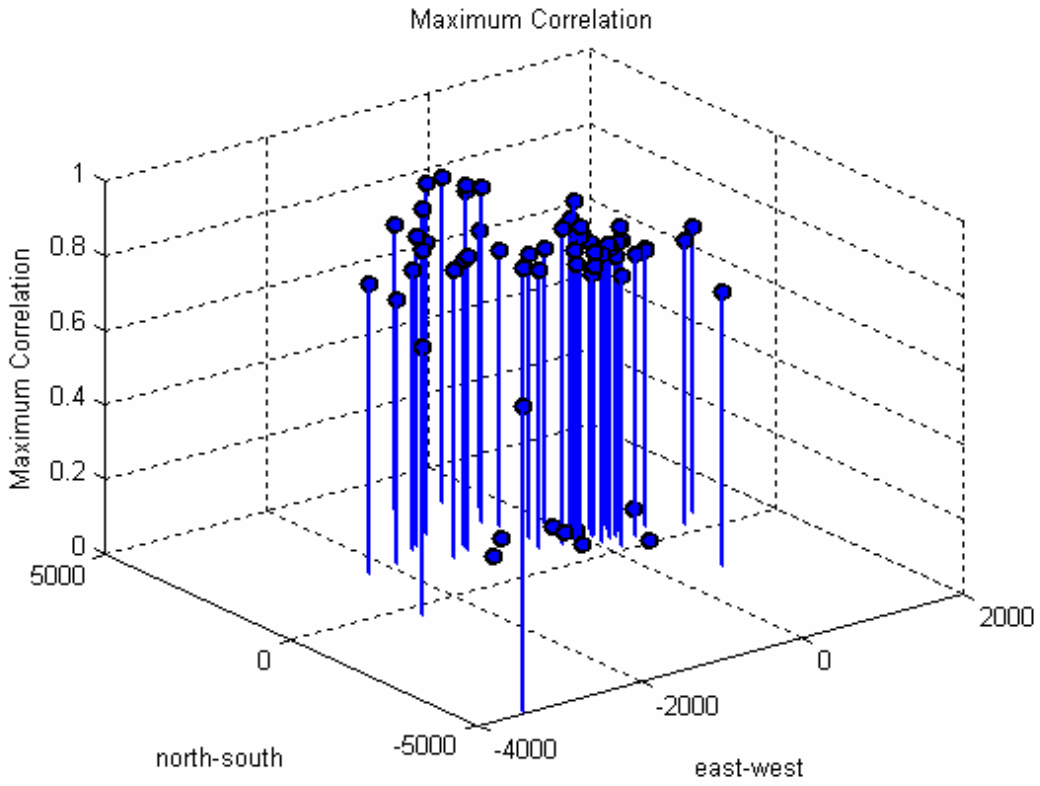

Figure 10: Maximum correlations for Krafla events
Maximum correlations for Krafla events showing two distinct fracture lines. Maximum values are determined by comparing all events at all stations.

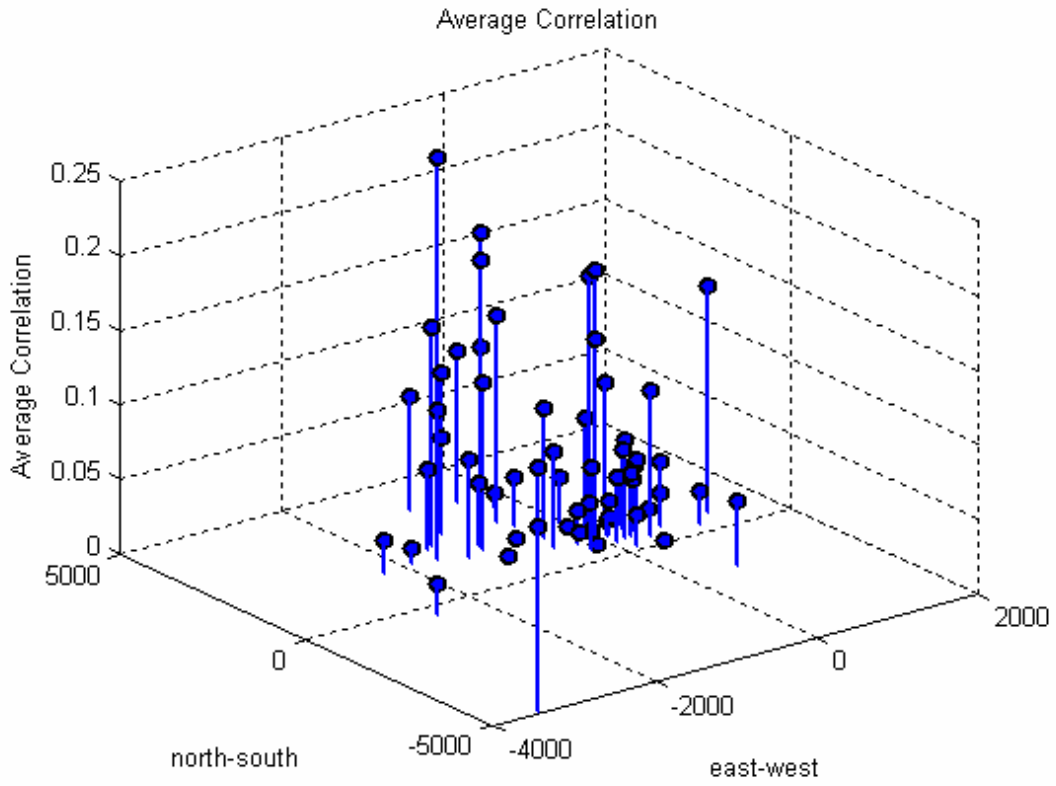

Figure 11: Average correlations for Krafla events
Average correlations for Krafla events showing two distinct fracture lines. Average values are determined by comparing all events at all stations.

1.4.5 Dynamics – time evolution

The time evolution of the events is displayed in Figure12. In this figure the time sequence goes from red to green to blue. While there is no dramatic shift as a function of time, it does appear that the later days are shifted toward the northwest. The initial values in red tend to be clustered to the east of the injection well. These represent the first 3 days of events. The middle 3 days of events in green appear to be centered around the injection well. The final events are predominantly located to the Northwest of the

injection well. The east-west cross-section shows a similar trend, but no discernible change of depth with time.

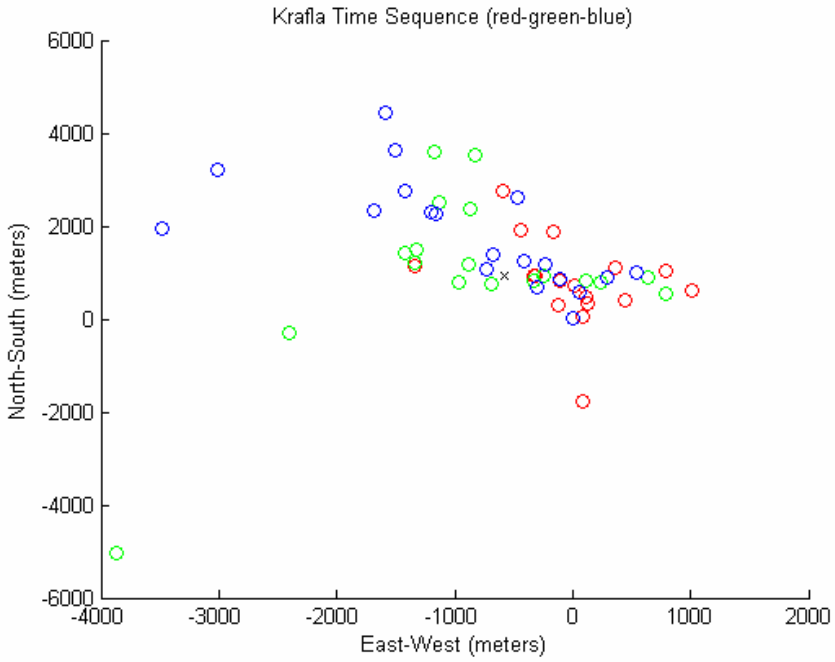

(a)

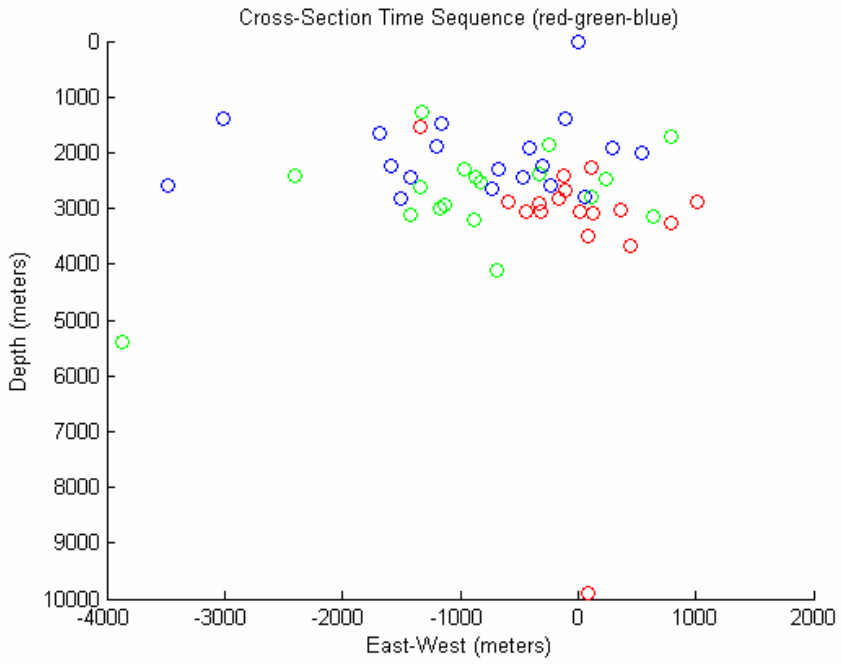

(b)

Figure 12: Time sequence of Krafla events
In sequence, red, green, blue each represent a time period of about 3 days. (a) The map view is shown. (b) A cross-section is shown.

1.5 Puna data

The "Puna" data arises from the eastern rift zone of Kilauea. The Puna Ridge extends into the ocean for over 75 kilometers. This was considered a good test of the double-difference algorithm because only four stations were used, a situation which may arise in the analysis of the Basel data. Furthermore, as can be seen, the stations were arranged in a rather linear pattern, not ideal for identifying event locations. Data was collected over 70 days during which time 390 events were recognized by the trigger program. The purpose of this study was to determine if the small number of stations and their non-optimal locations would prevent location by the double-difference algorithm.

In the first stage of analysis, we located the events using the standard locator program. The cross-correlation and double-difference routines were then applied to the data. Of the initially triggered 390 events, only 351 had a sufficiently large correlation coefficient to be considered similar and be considered part of the cluster. The event locations for this part of the analysis are displayed in Figure 13. Some structure is seen but no clear fractures can be identified. From the standard deviation, it is estimated that the uncertainty of the locations is on the order of 30-50 meters. It is seen in Figure 14 that the events with high correlation are clustered near a central site with correlation falling off with distance from the site.

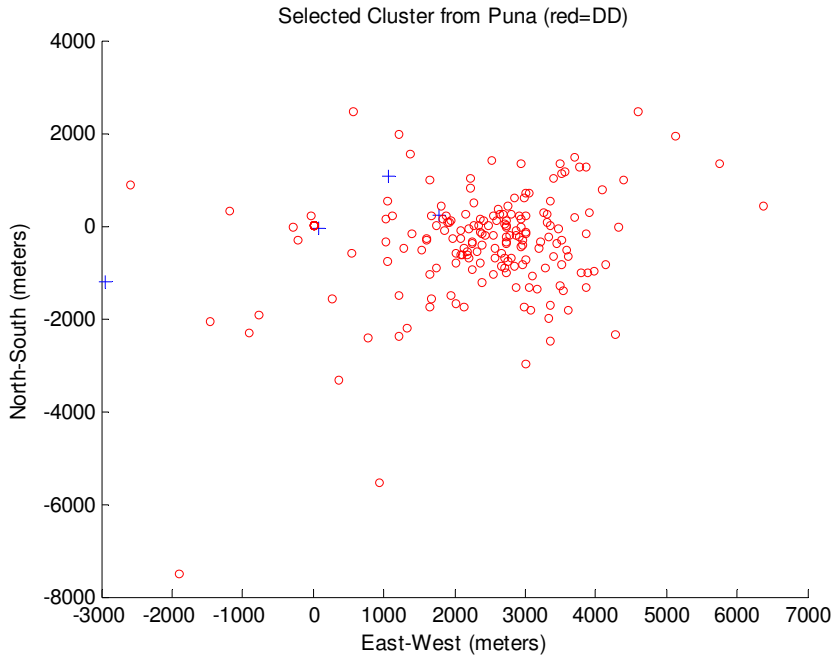

Figure 13: Double-difference locations from Puna data
The +'s represent the station locations. No shift has been made to correct for absolute position.

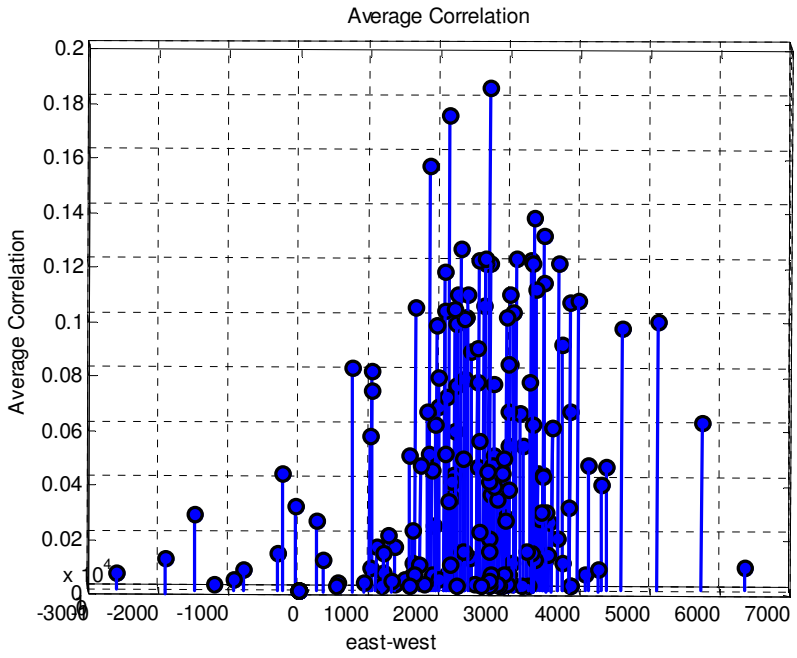

Figure 14: Average correlation of Puna events.
The average is calculated over all stations receiving the event signal

1.6 Basel Data- Cementation results

Following the drilling of the injection well, a process know as cementation, during which the walls of the injection borehole are lined with concrete cementing the casing in place, was performed. During this process, event signals were seen at the six borehole seismometers. From the approximately twenty signals that triggered the automatic picking routine only nine were seen at more than two stations. One of the stations, OT2, received all of the signals, probably because it is located at a depth of 2740 meters, closest to the events. The other station that received most of the signals, Riehen-2, is the new sensitive, double walled sonde recently deployed at a depth of 1213 m. The

locations and depth of the stations are displayed in Table 1. A map view of the stations is shown in Figure 15.

Table 1: Basel Station Properties

	Station Otterbach 2	Station Otterbach 1	Station Haltingen	Station St. Johann	Station Schützen-matte	Station Riehen 2
DSL-Link	SDSL 1 Mbps	SDSL 1 Mbps	SDSL 768/768 kbps	Super ADSL 600/600 kbps	Super ADSL 600/600 kbps	ADSL 600/600 kbps
surface station coord. (x/y in m)	612430.00 / 269685.00	612424.00 / 269684.00	611644.65 / 272923.85	609842.20 / 269342.15	609848.60 / 266748.90	616437.44 / 271468.18
downhole station coord. (x/y in m)	612486.00 / 269837.97	612452.00 / 269637.60	611629.60 / 272922.15	609832.90 / 269339.60	609847.70 / 266750.00	616505.94 / 271461.18
sensor depth b.g.s. (m)	2740	500	542	316.9	553.3	1213
altitude at ground surf. a.s.l. in m	252.61	253	247.4	261	278.9	285.31
sensor depth a.s.l. in m	-2487.39	-247	-294.6	-55.9	-274.4	-927.69

I modified the double-difference code from previous algorithms to accept the velocity structure supplied by Geothermal Explorers. Rather than use a gradient model, a two-layer structure was used, with the second layer beginning at 2516m. It was understood that this was a crude model, but it was anticipated that the double-difference routine's insensitivity to model error would overcome this problem.

The initial automatic picks were not of sufficient precision to locate the events. The residual deviations for locations calculated in the double-difference routine were approximately 0.5 seconds. The events were scattered over a region extending more than 5 km from the well-head. The locations were sensitive to the initial location and to

damping. The number of iterations required, while dependent on the damping, was always greater than 40, and in one extended run went to over 2000.

Manual refinement of the picks resulted in stable locations clustered within a few hundred meters of the well-head. We initially used only the p-wave arrival times for which we had the most confidence. Our initial starting location was beneath the well-head at a depth of 4000m. Within four iterations the tolerance was reached and the residual was reduced to 0.0021 seconds, comparable to previously described calculations. The overall configuration was stable, with relative shifts of less than 10m, when the horizontal position of the initial site was moved by 500 meters. Shifts in the depth of the initial site caused commensurate shifts in the depth of the final locations. The horizontal positions remained stable.

The location of the events indicate two main fracture lines. These are shown in Figure 16. The fracture lines are evident in the map view as well as in the cross sections. While nine events are too few to definitively map out fractures, these results are evidence in support of fractures being the site of events. When the locations are identified by absolute time, it is seen that the earlier event are closer to the well-head and the later events further away. This is in keeping with our understanding of the spread of the fractures. The increased pressure should initially cause events near the well-head. As the pressure builds, the events should move away from the well-head. It was also seen that the two fracture lines were initiated at different times. Later events appeared along a separate line from the initial events, suggesting that a second fracture opened at a later time.

Figures 16c and 16d show the borehole trajectory in relation to the events. The events seem to occur along cracks that run nearly parallel to the borehole. This is reasonable as the stimulation is coming from the cement being poured into the borehole surrounding the casing. These locations gave us confidence in the reliability of the double-difference algorithm.

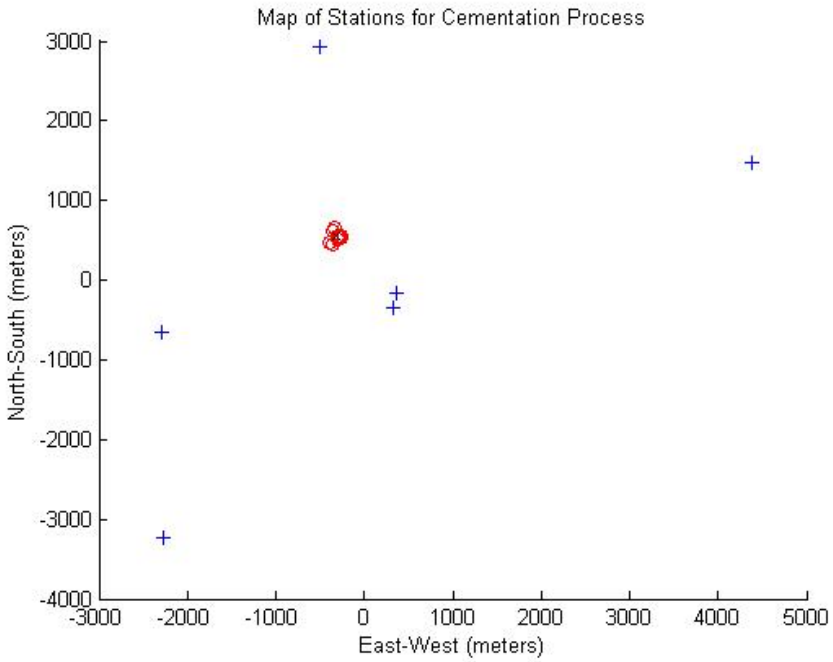

Figure 15: Map of Basel Stations
Map of Basel stations (+) with event cluster shown by (O). The (x), near the center of the events, marks the injection well position at the surface.

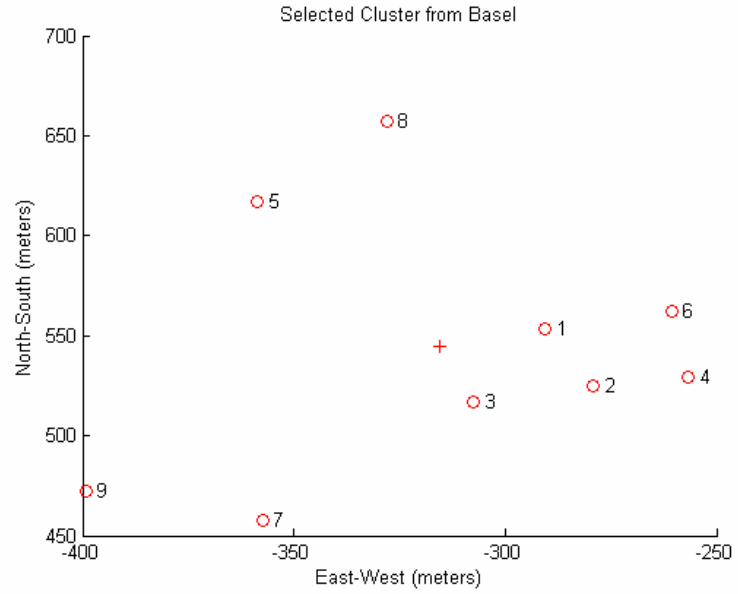
Selected Cluster from Basel
North-South (meters)
East-West (meters)
700
650
600
550
500
450
-400
-350
-300
-250
8
5
6
1
4
2
3
9
7

(a)

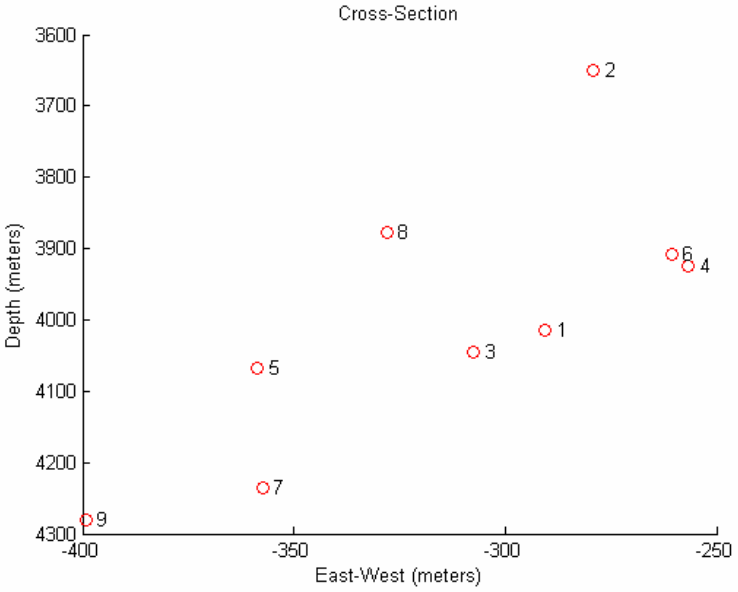
Cross-Section
Depth (meters)
East-West (meters)
3600
3700
3800
3900
4000
4100
4200
4300
-400
-350
-300
-250
2
8
6
4
1
3
5
7
9

(b)

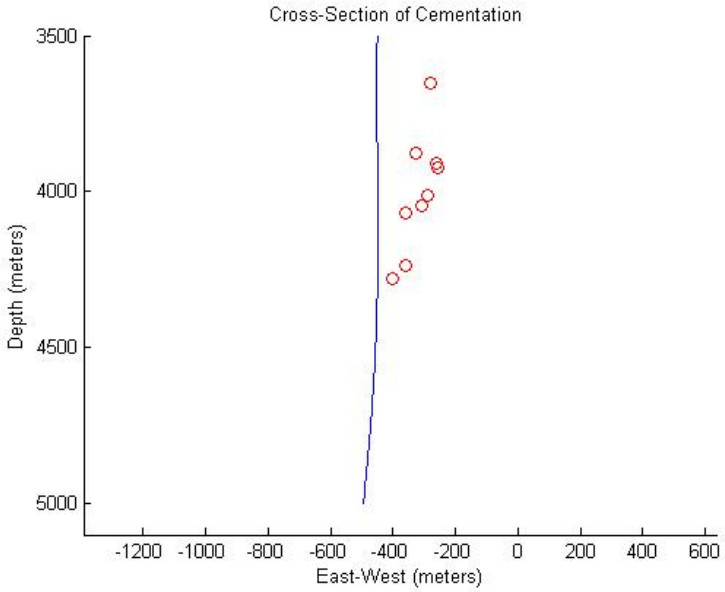

(c)

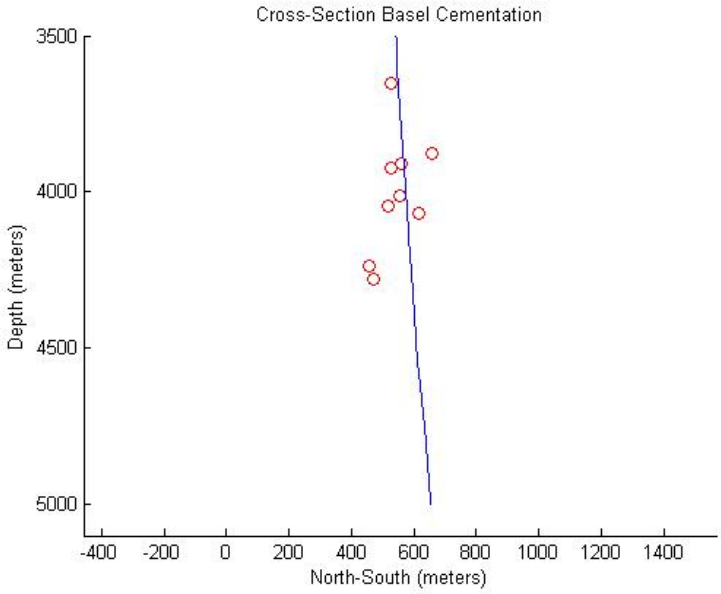

(d)

Figure 16: Double-difference locations for cementation process
Location of events found from double-difference routine for cementation process. Numbers represent time sequence of events (a) Map view with borehole denoted by (+); (b) Cross-section ; (c) North-South cross-section as in (b) with borehole trajectory shown (note change in scale); (d) East-West cross-section with borehole trajectory.

The s-wave data was less robust and of questionable quality. Only one of the nine events had arrival times from more than two stations (OT-2 and Riehen-2). The refinement of the s-wave arrival times from the auto-picked values was more difficult than the p-wave arrival times. Furthermore, all three detectors at each station "recorded" identical arrival times. This means that there is no evidence, at this level of resolution, of s-wave splitting. The addition of the s-wave arrival times led to a slight increase in the residual to 0.0026 seconds. Relative positions were shifted, and distinct fracture lines were not as clearly delineated. A sample of the application of the cross-correlation routine to the Basel data is given in Figure 17.

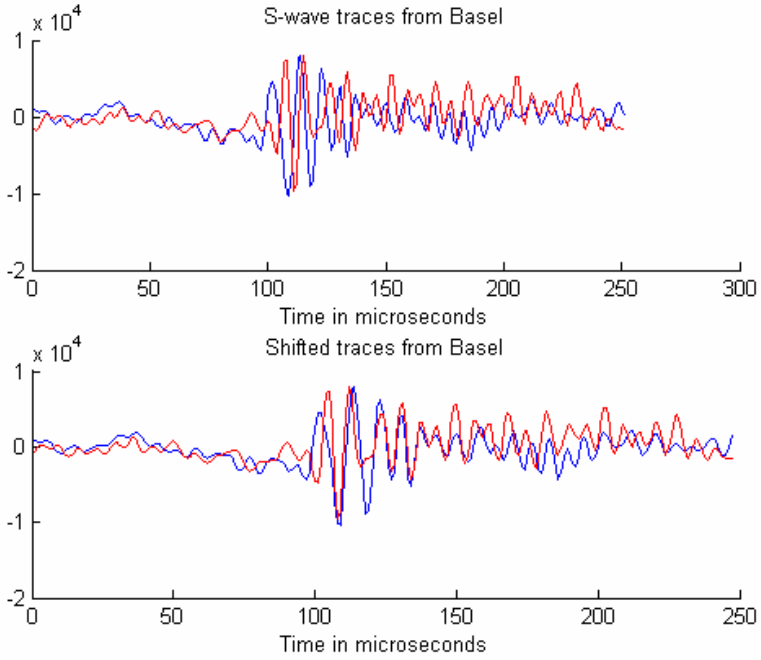

Figure 17: Sample signal from Basel cementation
Cross-correlation was found to be 0.52 with a lag time of –0.003 seconds. (a) Signals before time shift. (b) Signals after time shift by -0.003 seconds.

It should be noted that our single-difference locator program was also able to identify the cluster locations when both p- and s-waves were used. For s- or p-waves

alone, most events had too few signals for a location to be determined. With the exception of two events all of the residuals were less than 0.0025 seconds. For the two less precise locations the residual was ~0.0050 seconds. These residuals differ from the ones calculated from the double-difference calculation, but have the same interpretation. In the double-difference calculation, the residual is determined as an average over all of the events, while in the standard locator calculation each event is distinct and the residual is calculated as an average over all of the stations seeing the event. Because the single-difference locator program used a gradient model velocity (fitted to the layer structure), rather than the layer structure, the locations were shifted away from the well-head.

1.7 Conclusion

In this chapter, I have reviewed the double-difference formalism with the accompanying cross-correlation algorithm. These techniques have the potential to determine the relative locations of seismic events with greater precision than from absolute locator algorithms that do not take the difference of arrival times. The cross-correlation calculation allows the possibility of determining arrival time differences with a greater accuracy, while the double-difference code can cancel errors in model velocity structure.

I tested the codes on synthetic data in the form of lines and grids, and on real data from the Mammoth data set. When the data is noise free the double-difference algorithm is able to determine absolute locations with an accuracy of ~10 meters. In the case of the

Mammoth data, relative locations were satisfactory considering the limitations of my knowledge of the parameters, but there was a needed shift in the absolute locations.

These algorithms have been applied to several data sets revealing structure that had not been previously seen through seismic analysis. In the Krafla data set, two distinct fractures were located using the cross-correlation and double-difference algorithm. These are consistent with MT data and further refine the previous locations found from my standard single-difference locator. The Puna data was further refined showing a cluster of sites with high correlation which fell off with distance from the center of the cluster. Most revealing was the Basel analysis arising from the excitation of seismic events from the cementation process. Attempts by several other groups had failed to locate the events within 5 km of the wellhead. This was generally attributed to the inaccuracies in the velocity model. The double difference code not only placed the events within 100m of the wellhead's coordinates, but also suggested two distinct fractures. The sensitivity of the results to the initial location was tested.

Future work will involve applying these codes to the Basel Deep Heat Mining Project. The cross-correlation code will be refined to enable the calculation of lag times so that arrival time "picking" can be automated. This will be critical for the s-waves so that shear-wave splitting can be determined. The goal of the seismic analysis of the Basel project is the mapping of the growth of the hydro-fractured reservoir and the understanding of the crack propagation involved.

1.8 Double-Difference Code:

ddmain.m is the main program which initializes the data. It loads the station coordinates (bx,by,bz) and the arrival times. It also writes the results. It is essentially the input/output program. To get the hypocenter coordinates (m), **ddmam** calls **getddm.m.**

getddm.m is the program which arranges the elements of the double difference matrix (excluding rows where events are absent) and solves for the hypocenter coordinates (m). To generate the elements of the matrix, **jac.m** is called. To calculate the double difference $\{(ti-tj)_{obs}-(ti-tj)_{calc}\}$ **dbldif.m** is called. The inverse is taken by the function **lsqr.m**, a least-squares inverse routine for sparse matrices (Page and Saunders,1982) which has been adapted to this procedure. This speeds up calculations by a factor of at least three over matlab's pinv routine.

jac.m calculates the derivatives of the arrival times numerically and labels the values G. To evaluate the arrival times **evaldd.m** is called.

evaldd.m calculates arrival times by using the traveltime formula appropriate to the model structure. To use the formula, the ray parameter (p) is needed which is found using the matlab fzero command on the expression in **findprdd.m**.

findprdd.m gives an expression for the depth (z) in terms of the ray parameter (p) so that the matlab fzero command can be used.

dbldif.com uses the arrival time data and **evaldd**.**m** (to calculate the arrival times) to calculate the double difference $\{(ti-tj)_{obs}-(ti-tj)_{calc}\}$ for each pair of quakes at each station.

Chapter 2

2. Basel Main Stimulation: Characterizing the Hydro-Fractured Reservoir

2.1 Introduction

Geothermal energy has been shown to be an effective source of power in regions which are volcanically active. The question is whether geothermal energy can be mined in regions which show no overt activity. One of the regions which shows promise is the Rhine Graben, a rift system extending from northwest to southeast through central Europe. This part of Europe is characterized by strike-slip faulting dominated by compressive forces of the alpine collision (Reinecker et al., 2003). This rifting has created a thinned crust. A buckling of the Moho to a minimum depth of 24 km in the Southern Rhine Graben (Bonjer, 1993) brings high temperature regions (>200C) to within 5 km of the surface. To exploit this energy source, trial power plants have been built along the rift zone, most notably at Soultz-sous-Forets. These trials have shown the feasibility of mining energy in seismically quite regions.

One of the key components of the power station is the reservoir. The initial phase, the stimulation phase, hydro-fractures the rock creating a reservoir through which fluid can flow. In this chapter, the growth of the reservoir in the Basel Deep Heat Mining Project during the stimulation phase will be studied. One means of determining the characteristics of the reservoir is to record the seismic activity stimulated by the hydro-fracturing of the rock.

> Mapping of acoustic events is one of the most important tools we have for understanding the reservoir. In hydrothermal systems, we know from well tests and tracer tests that water is circulating and in contact with large areas of rock. We can assess stimulated fractures in the same way, once we have two or more wells in hydraulic connection to allow for circulation tests. We can map the location of acoustic emissions generated during stimulation and during circulation extremely accurately, i.e., ± 10-30 m. While we are not completely sure what the presence or absence of acoustic emissions means in terms of fluid flow paths or reservoir connectivity, knowledge of the location and intensity of these events is certainly important. This information helps define targets for future wells. (MIT report on EGS, 2007).

The microseisms generating the acoustic activity are located at the fracture sites, so that by mapping these events it is possible to map the development of the reservoir. Furthermore, it may be possible to determine fault planes and the focal mechanisms associated with the events.

There are several goals for this study: a) to map out the microseisms and from them determine the size and structure of the reservoir; b) to determine the time evolution of the reservoir during the hydro-fracture phase of stimulation resulting from fluid-crack interactions; c) to analyze the results in order to determine the orientation of the fracture planes. The chapter is organized as follows: in Section 2 an overview of the Basel Project is given. Section 3 describes the stimulation which occurred December 2-8, 2006. In Sections 4 & 5, the data acquisition and analysis is presented. This is followed by the results in Section 6, which are discussed and analyzed in Section 7. The focal mechanism calculations are presented in Section 8, and the Chapter's conclusion is in Section 9.

2.2 Overview of Basel

Switzerland is powered by hydroelectric and nuclear power. Additional power is needed and could be supplied by geothermal sources. The Basel region is situated at the southeast end of the Rhine Graben and belongs to a Cenozoic rift system, which is limited to the south by the fold-and-thrust belt of the Jura Mountains (Meghraoui *et al*, 2001). Because of these features, Basel is subject to mild seismic activity. In fact, Basel has experienced several major quakes, the worst in 1356 destroyed the city and has been analyzed to have been of magnitude 6.5 to 7.0 (Weidmann, 2002), the largest quake ever recorded in central Europe. The NNE-SSW-trending Basel-Reinach escarpment, which is 8 km long and 30 to 50 m high, has been identified as the surface expression of an active fault (Meghraoui *et al*, 2001). Most quakes are rather shallow, some occurring within 5 km of the surface. The heat flow in the region is between 100 and 130mW/m^2 (Medici and Rybach, 1995) compared to a globally averaged value of about 50mW/m^2. This suggests that the region near Basel would have a strong potential to be a source of geothermal energy that could be efficiently mined.

The goal of the Basel Deep Heat Mining Project was to develop a co-generation power plant that could generate both electric and thermal energy. The pilot plant was projected to generate 30MW of power from a circulation of 30 liters/s. The waste incineration of the municipal water purification plant provides an additional heat source. In combination with this heat source and an additional gas turbine, a combined co-generation plant can produce annually up to 108 GWh electric power and 39 GWh of thermal power to the district heating grid. (Haring, 2004)

> The Deep Heat Mining Project commenced in 1996 with the presentation of the basic concept. Preliminary studies and site selection took place in 1997-98. After several failed attempts beginning in 1999, the Otterbach exploration well was drilled in 2001. The well is located on the downthrown side, about two kilometres east of the main boundary fault. It was the first well in this area penetrating the entire sedimentary sequence down to basement. This sedimentary sequence consists of Tertiary clastics, Mesozoic carbonates, shales and evaporites and Permian sandstones, whereas the top granitic basement is located at 2649 m. The temperature gradient reaches 40 °C/ km and the heat flow and heat production measurements in the outcropping granites on the flanks indicate that the same gradient is likely to persist down to the target depth. Following in 2003-4, the first deep well was bored. Return wells were drilled in 2005-6.
>
> Borehole deformation logging with acoustic and electric borehole televiewer tools shows induced fractures pointing predominantly in a NNW direction and induced borehole breakouts in the perpendicular direction. This trend is completely in line with the regional stress field (Plenefisch and Bonjer, 1997). No pressure tests were performed. (Haring *et al*, 2007)

In February 2006, six sensors designed and built by Sondi Consultants (a corporation consisting of some members of the Duke University Seismology Program) were deployed, and background readings were taken to determine the baseline seismic activity. These sensors (see below) were deployed at depths from 317 meters to 2740 meters within several kilometers of the proposed injection site. No significant seismic activity was recorded. The station at Otterbach 2, failed as a result of over-pressure and was replaced in November, 2006.

2.3 Stimulation

In 2006, the injection well was bored to a depth of 5000 m, and the stimulation of the reservoir began shortly after. The stimulation was divided into two phases, a pre-stimulation phase, which took place between November 23-26, and a main-stimulation phase which took place between December 2-8.

The purpose of the pre-stimulation phase was to characterize the unperturbed reservoir. For this phase the flow rate was minimal, 10 liters/minute, with a well-head pressure of 7.38×10^6 Pa (=1070 psi). The hydraulic conductivity was between 10^{-9} and 10^{-10} m/s, which was considerably less than the conductivities seen in other studies in the Black Forest crystalline basement (Stober and Bucher, 2007). Further, clear indication of bi-linear flow, observed during the hydraulic tests, suggest that the flow regime is dominated by single fractures (Haring *et al*, 2007).

The purpose of the main-stimulation phase was to increase the hydraulic conductivity by hydro-fracturing the rock and to test the feasibility of establishing a flow rate of 3000 liters/min. During the first 16 hours of the main stimulation the pressure was gradually increased to 1.10×10^7 Pa yielding a flow rate of 100 liters/min. In the following days the pressure was continually increased until by the sixth day the pressure reached 2.96×10^7 Pa, yielding a flow rate of 3600 liters/min. However, because of the increased seismic activity, peaking at about 190 events/hour, and the occurrence of a M2.7 event, the decision was made to decrease the flow rate to 1800 liters/min. With continued seismic activity and another M2.7 event the well was bled-off. In the process of beginning the bleed-off process a M3.4 event occurred. Following the 4 day bleed-off some seismic activity continued with notable events occurring 29 days (M3.1), 39 days (M3.2), and 55days (M3.3) after the shut off (Harding *et al*, 2007).

During the main stimulation approximately 13,000 events were recorded (see figure 18), of which about 3,000 were locatable, since many of the events were seen by only one or two stations. The total water injected over the six days was 11,566 m^3 of

which 2,800 m^3 was returned to the surface, the rest of the water remained in the reservoir (Harding *et al*, 2007).

Because of the concern over risk to people and property, an independent risk evaluation is taking place to determine the appropriateness of continuing the project.

2.4 Data Acquisition

To monitor the stimulated events in Basel a set of six sensor locations were selected. As described in Table 2, the sensors were placed at depths ranging from 316.9 to 2740 meters below the ground surface within several kilometers of the location of the injection well. Each of the sondes contains 3-C Galperin mounted sensors, except for OT2, which has orthogonally (V, H1, H2) mounted sensors. In addition, several of the sondes contained 3C MEMS (accelerometers).

The design of the sonde for the deep station (OT2) was limited by several factors. The diameter of the borehole was 3.5 inches and the sonde had to be less than 3 inches in diameter in order that if the sonde buckled under pressure it could be removed without compromising the borehole. To prevent buckling at 5000 meters (~$5x10^7$ Pa ≈ 7,000 psi), the design was based on the von Mises formula for the critical pressure for buckling of cylinders to determine radius and thickness (Roark and Young, 1975). In the formula, the critical pressure is proportional to $(t/r)^{2.5}$, where t is the thickness of the cylinder and r is its inner radius. It was determined that r = 1.28 inches and t=0.125 inches would have a critical pressure of greater than 40,000 psi for a sonde of 30 inches in length, well above the tolerance required. Pressure tests at 10,000 psi confirmed the integrity of the

sonde. In addition, the sensors were gimbaled and had to be capable of rotating by 8 degrees without affecting the sensitivity by hitting the sonde. The design was such that the horizontal sensors went out of spec at 16 degrees, while the vertical went out at 20 degrees, well within tolerance.

The final design places the SM-6 and HS-1 sensors in completely separated pressure cases, with 2 different feedthroughs. The SM-6's were housed in a heavy frame whose pressure housing was mounted in a fully potted outer tube. The intention was to get a heavy unit with substantial inertia. It also means that if one case failed there was a second chance to maintain the integrity of the system.

The details of the OT2 sensor and its response can be found in Appendix 2.

2.5 Data Analysis

Data from the stations was digitized and sent over a link to a server at which the signals are recorded and categorized. Those events which are seen by at least 4 stations are analyzed by DIVINE, a routine developed by Ben Dyer of Semore Seismic, Ltd, Cornwall, UK. In this routine, the seismograms are processed and arrival times are estimated. From this process, preliminary event locations are estimated. At this point a manual review of the arrival times was performed and corrections were made where appropriate. Following, this a second correction was made to the arrival times for each station and phase. The purpose of this adjustment was to take into consideration velocity model errors. These errors can come about from mis-estimation of layer velocities, as well as from horizontal velocity variations. In Table 2, the velocity model is given and

the time corrections are shown in Table 3. It is important to note that the time corrections resulting from variations to the velocity model do not apply to the seismograms when doing analysis of wave forms, in the cross-correlation calculation for example.

2.5.1 Cross-correlation

As described in the previous chapter, there are two benefits to using cross-correlation in the preparation for double-difference calculations. The first benefit arises from the fact that the double-difference technique depends upon the events being compared being similar. The near cancellation of path effects in double-difference assumes that the waves are of similar origin. In this study, we select those events that are similar by a cross-correlation calculation. All events which are linked by a cross-correlation coefficient greater than 0.85 are included. This value of threshold is based on the work of Schaff *et al* (2003); however, deviations of 0.05 from this value had only minor effects on the eventual cluster. This linkage can be indirect in the sense that two events may have a cross-correlation less than the threshold but are each linked to another event by a cross-correlation greater than the threshold. To determine this linkage, the cross-correlation coefficient of each event with all of the other events which took place at a later time (to eliminate double counting) is calculated and a matrix of values for the pairs of events is created. This matrix was then analyzed to determine linkages between all events. In practice, this procedure proved too time-consuming for large data sets since the calculation of each of the approximately 4.5×10^6 cross-correlation coefficients took about 10 seconds. To streamline the process, an event would be compared with all others

until the correlation exceeded the threshold. The event identifications of the pair of correlated events would then be stored, and the next event would be compared to all of the others. A second routine would take this data and construct the fully linked cluster from these pairs. Most of the events not included in the linked cluster had no matches with any other event and would have been eliminated under any scheme. Other events were in small (2-10 events) clusters. While it is possible in pathological situations that a small cluster might be linked to the larger one, a survey of the larger of these small clusters showed they were not linked. The cluster of events which were linked was used in the double difference calculation.

A second more restrictive determination of similarity was used to analyze the events similar to the M3.4 event. In this case, the cross-correlation coefficient of the M3.4 event with all of the other events was calculated. Only those events with a coefficient above a given threshold were said to be similar to the M3.4 event and placed in the M3.4 cluster. The waveforms of the events in the M3.4 cluster, as recorded in the vertical sensor of OT2, are displayed in figure 20. The number of events for the direct linkage was very much dependent on the cross-correlation threshold, varying by nearly a factor of 2 for every change of 0.05 in the cross-correlation coefficient.

A key feature in the cross-correlation calculations is the window in which the seismograph is sampled. If the window is too large then other phases will be included, and the correlation will be lower. If the window is too small then the correlation can be artificially high because only a portion of the signal will be included. I did a variety of tests to determine the optimal window for the data and used a window of 250 ms centered

on the P-wave arrival time. To increase the signal-to-noise ratio, only the vertical sensor of OT2 was used. In figure 19, a representative comparison of the waveform of an event is displayed as recorded by the vertical sensors on OT2 and OT1. The higher resolution and signal-to-noise ratio obtained by OT2 is evident. To further eliminate noise, a 9^{th} order Butterworth low-pass filter was used with a cutoff frequency of 50Hz. This would allow roughly 6 periods of the highest frequency to be included in the window. The correlation coefficients were not very sensitive to the cutoff frequency; however, too small a cutoff tended to increase the coefficients and too small a frequency tended to decrease the correlation coefficient.

The second benefit of using the cross-correlation is the ability to refine the arrival times. This is done by calculating the lag time, which is the shift in time required to maximize the cross-correlation coefficient for one event seen at two stations. For this determination, I chose to compare the seismogram from each of the stations receiving the signal from an event with the signal seen for the event on OT2 sensor, since that station recorded all of the events. The window for the cross-correlation to determine the P-lag time was 100 ms and began 50 ms before the P-wave arrival time. The window for the S-lag time was also 100 ms, but to avoid contamination with the P-wave signal, it began 25 ms before the S-wave arrival time. Larger widow sizes gave different lag times because the lag time would then refer to the time to align a larger portion of the signal rather than just the onset. The results were not very sensitive to smaller windows, but the peak of the signal might be missed with too small a signal, yielding spurious results. Through this process any non-zero lag times became corrections to the arrival times. In general, the

corrections were on the order of a few milliseconds. These results were compared to the original arrival times to determine the importance of the correction. The new arrival times were then used in the double-difference calculation.

2.5.2 Single- to Double- Difference

The double-difference algorithm as adapted in this study was first presented by Waldhauser and Ellsworth in 2000. To increase portability, I wrote a MATLAB code based on their theory using a multi-step process to determine the locations of the recorded events. The first step in the location of the events is to use a single-difference algorithm to arrive at a preliminary location for the events. The algorithm has as its input the station locations, the S- and P-arrival times, an initial guess of location, and the velocity model. In addition, the tolerance and the maximum number of iterations of the non-linear-least-squares routine needs to be specified. The algorithm takes the arrival times at each of the stations and makes a best-fit estimate, in the least squares sense, of the location and origin time. With each iteration the four unknowns are updated and the standard deviation of the actual arrival time from the calculated arrival time, determined from the estimated location and origin time, is determined. This process is carried out until the maximum number of iterations (40) is reached, or until the difference between the standard deviations of two consecutive iterations is below the tolerance (1μs). For the Basel events, the initial guess was not critical as long as it was within a 2 kilometer cube, centered near the injection site. The initial guess for the origin time was one second

earlier than the first arrival time. Again, the results were not sensitive to the origin time estimate.

There are several advantages to using the single difference location in the initial step. First, events which have erroneous or inconsistent arrival times are isolated without having any impact on the locations of other events. This is important because of the linkage that occurs in the double-difference calculation. "Suspect" events can contaminate the cluster. It is expected that most of the suspect events are found in the cross-correlation, but some of these events were found in the single-difference calculation. Secondly, the closer the initial estimate of the locations is to the final result, the shorter the computing time in the double-difference routine. This is significant because the computing time for the single-difference is about an order of magnitude faster than that for the double-difference. This also helps with the accuracy of the final locations because the 4-dimensional space in which the locations and time-origins reside has many minima in the least squares calculation. There is always the possibility that the global minimum that is sought is not the local minimum which is closest. This is a very difficult problem and is best illustrated by making a poor initial guess for the locations. A minimum is always found, however, the standard deviations of the results could be substantially larger, representing a local rather than a global minimum. A reasonable initial estimate of the locations allows for a larger damping factor (smaller steps) in the least-squares fit to be used, and the skipping from one minimum to another to be avoided. Finally, the double-difference routine is only a relative locator. That is it yields the relative locations of the events with better accuracy than their absolute locations. Shifts

in the initial estimates of locations can give shifted final locations, while keeping intact the relative positioning. Since the single-difference algorithm is an absolute locator, it is expected that by using the locations from the single-difference routine as input to the double-difference routine, the locations will be more accurate in the absolute sense.

The double-difference routine was described in the previous chapter. It has as its input the single-difference locations, the station locations, the velocity model, the arrival times, and the cluster events as determined from the cross-correlation coefficients. As in the case of the single difference calculation the maximum number of iterations for the non-linear-least-squares fit must be specified as well as a tolerance for the standard deviation. In addition, the lsqr (Page and Sanders, 1982) algorithm, a least-squares algorithm for sparse matrices, requires a damping coefficient as well as a separate tolerance and an iteration maximum. The outputs are the event locations and the origin times. Only those events which are similar and have a single-difference result which converged with a standard deviation less than 0.1 seconds are used in the double-difference calculation.

Because of the size of the data set and the limitations of memory, the full cluster of approximately 3000 events could not be handled in one group. The number of columns is equal to four times the number of events and the number of rows is the number of pairs of events, summed for each station, for the P and S phases. In our case the matrix that would have to be "inverted" would be roughly (2 phases x (3000x2999/2) pairs *6 stations) ~5×10^7 by 12,000, well beyond the capability of the standard desktop. Since part of the goal of writing the routines in MATLAB was portability, a change to the

standard means of calculation had to be employed. The routine takes a group of events that belong to the cluster and finds their double-difference location. It then takes another group with a common element from the previous group calculates the double-difference location and shifts the locations of the second group so the common event has the same location. This linkage keeps the individual groups aligned. Group sizes varying from 8 to 45 showed final location differences of less than 20 meters. The differences of standard deviations for different sized groups were not significant.

2.6 Results

2.6.1 Location of events

The procedure described above was used to determine the locations of the 3000 events which took place during the main stimulation and in the days immediately following, from December 2, to December 8, 2006. The four plots shown in figure 21 show a map view including the station locations, an enlarged map view, and two cross-section views. The figures show the microseism cloud with a depth varying from approximately 3000 meters to about 5000 and a horizontal extent of approximately 1000 meters. The axis of the microseism cloud appears aligned with the trajectory of the injection borehole with the maximum depth near the bottom of the borehole. The M3.4 event is situated in a cluster of events with a range of about 100 meters. While there appear to be some filamentary structures which could be interpreted as cracks, the uncertainty of the relative locations of ± 25 meters makes that interpretation unreliable.

The standard deviation of the double-difference gives an indication of the uncertainty of the results. Standard deviations for groups within the cluster are on the order of 5 milliseconds. The mean speed of about 5000 m/s suggests a range of positions of approximately 25 meters. While this is a crude estimate it serves to indicate the reliability of the results. Other tests of accuracy, as discussed in the previous chapter, included putting noise in the arrival times and varying the model velocity. Those tests were consistent with the present estimate. In addition, a change in the group size had minimal (~10 meter) effect on locations.

2.6.2 M3.4 cluster

The M3.4 cluster, consisting of those events which have a cross-correlation coefficient greater than 0.8 with the M3.4 event, is shown in figure 22. In this figure, the small cluster of events in the vicinity of the M3.4 event has a range of approximately 100 meters. It is possible that these events have the same origin as the main event and that their orientation could map out the fault plane. It is also noteworthy that source scaling results indicate that the source radius of the main event is on the order of 100 meters (see following chapter).

2.6.3 Time evolution of events

The development of the reservoir is a major concern of this study. Several reasonable models could describe the growth of a reservoir. The reservoir could expand in a particular direction, perhaps along fault lines due to the injection. As an alternative, the reservoir could grow “uniformly” from a central area expanding outward like a

balloon. Or, perhaps, the growth could be more erratic, following the path of least resistance as cracks propagate in many directions. The development of the reservoir is of interest for several reasons. First, it is important to understand how the stimulation parameters, fluid injection and pressure, affect the growth of the reservoir. It would be beneficial to know how adjusting the flow rate and pressure can control the reservoir growth. Knowledge of the growth of the reservoir might also lead to improved production well locations. Secondly, knowing the underlying structure, perhaps the evolution of the well can be predicted. If we can document the expansion of the reservoir, it may be possible to compare it with known fracture structure to get information about the dynamics and crack propagation. Finally, it is of intrinsic value to study the evolution of a hydro-fractured reservoir with the intent of comparing the information obtained with that from other sites. I have attempted to address these issues by using the time-dependence of the event locations as representing the evolution of the reservoir. While these questions are not resolved in this study, the results form a framework for further investigation.

The first step in this process was to visualize the reservoir by making a time series "movie" of the events. In each frame of the movie, 15 events in sequence were added to the microseism cloud until all events were displayed. Each new group was displayed in a color different from the events in the existing cloud. An image of the evolution is displayed in figure 23, where color-coding shows the time sequence. Each of the four colors depicts the locations of 800 events. The time evolution of the microseism cloud shows that the initial events begin near the borehole trajectory about 200 meters from the

bottom. The events gradually expand from that location, although no discernible track is seen. From this representation, it appeared that the events were not focused at locations that moved through the region. It was also evident that the events in each new group were not located at the margins of existing cloud but were scattered throughout the reservoir. This can be seen by examining the last events, shown in black, in figure 23. Therefore, two of our suggested models were contradicted. The reservoir did not grow in a particular direction nor did the events occur at the outer boundaries of the reservoir. To quantify the growth of the reservoir, it was necessary to analyze each group.

My approach to this was to calculate the standard deviation of the distance of the members of each group from their mean position. It was expected that this calculation would give some information about the growth of the reservoir. I performed the calculation for a variety of group sizes from 10 to 50 events and the nature of the results presented is independent of the size of the group. For the purpose of this section, I will present the results for groups of size 15.

Figure 24 displays the standard deviation of the groups, as described above, in sequential order. Most apparent is the nearly linear increase of the standard deviation as a function of group number. While there are the expected fluctuations in the values, the overall trend as shown by the straight line is evident. The interpretation of this trend is that, while the events are scattered throughout the reservoir, the locations are gradually and fairly uniformly spreading out as a function of time. All of the activity is not at the margin of the reservoir; cracks are being opened even in interior regions. Nevertheless,

the outside boundaries are expanding. I will refer to this standard deviation as a measure of the size of the reservoir, recognizing that not all events are at the boundaries.

To convey a sense of the development of the reservoir, figure 25 shows the mean location of each group. There is no discernible trend, and the mean wanders fairly randomly with group number. Plotted in this figure to illustrate the relative length scale is the mean position of the group containing the M3.4 event and the actual position of the M3.4 event. Even for this event, the members of the group were not clustered in the near vicinity.

2.7 Discussion and Analysis

2.7.1 Reservoir size and shape

Figure 21 shows that the microseism cloud is oriented along a line approximately 30° west of North, with a linear extent of approximately 1000 meters and a "width" of approximately 200 meters. The west-east cross-section of reveals a narrow profile of the cloud aligned very closely with the borehole trajectory, shown in figure 21c. The south-north cross-section displays the broader part of the cloud, still aligned with the borehole trajectory, shown in figure 21d. Of particular note is the location of the M3.4 event in figure 21d. It appears to be located in a region occupied by a group of events that is somewhat separated from the rest of the events in the cluster.

2.7.2 Time evolution of events

In order to understand the dynamics of the well, reference to the stimulation parameters is needed. It has long been known that fluid injection is associated with event activity, and the reservoir is expected to grow as a result of the volume of fluid injected. The usefulness of using the group standard deviation is seen when the plot is superimposed with the flow rate (figure 26) or the pressure at the X-tree (figure 27). The increase in size of the reservoir, as estimated by the standard deviations of the groups, is in close agreement with the flow rate from the injection well for that portion of the time when there is flow. Not coincidentally, there is also strong correlation of the pressure at the X-tree and the reservoir size. The similarity between these parameters and the reservoir size seems stronger than the similarity between the cumulative flow and the reservoir size (see figure 28). This can be interpreted in the following way: to expand the reservoir additional fluid and pressure are needed, and they are the parameters that drive the growth. The reservoir size is most closely associated with those values. The cumulative volume is a relatively smooth function of time, it is its derivative with respect to time, the flow rate, has the structure needed to account for the features seen in the reservoir size.

Evident in figure 24 are two major fluctuations. These fluctuations are statistically significant. In figure 29 I subtracted the trend line and calculated the means and standard deviations of the main section (the first 113 groups) and of the fluctuations. The means of the fluctuations are more than two standard deviations from the means of the main section. This is in the 95% confidence range that the samples are independent.

A t-test comparing the main section and the fluctuations indicate that there is less than 10^{-8} chance that the means of fluctuations are the same as the mean of the main section. It is interesting to note that comparing the two fluctuations with a t-test reveals a 50% chance that the means are the same. So, given that these fluctuations are significant, can their cause be determined?

In figures 24 and 29 are sets of asterisks indicating the groups containing the largest seven events, those events with seismic moment greater than $1*10^{11}$Nm. Their timing, just before the onset of the fluctuations, may be coincidental but can be interpreted as follows. The reservoir is increasing in size at a rather steady rate when several large events occur. The effect of these events is to "shake up" the region and perhaps create new cracks. This allows the pressurized fluid to fracture rocks at the boundaries of the reservoir. Once these cracks are opened, the trend returns to the original growth line suggesting that those pathways are still active. It is interesting that following a large event the "after shocks" are not confined to the immediate location of that event. The after shocks do not define the fault plane of the large event, but rather energize the whole reservoir.

Since these largest events occur shortly after sharp changes in flow rate (see figure 26), they may have been triggered by those changes. The actual cause of the strong fluctuations, might also be a result of the sudden change in the flow rate. The second fluctuation, occurring just after the stoppage of flow may have been a consequence of the M3.4 event, which, in turn, may have been triggered by a decrease in fluid injection, resulting in a collapse of the fracture.

Since the return flow does not begin until 2 hours after the M.3.4 event, there is no evidence that the location of the return wells influences the growth of the reservoir.

In summary, the microseisms appear to occur at random locations with the region of activity gradually expanding at a rate closely following the injection rate and pressure. From these similarities, during the injection phase, it is reasonable to infer a causal relationship between flow and pressure, and the reservoir size. While this is not surprising, it does pose the question, Why does the reservoir continue to grow (by this measure) in the shut-down phase? It may be that the decrease in flow triggers a collapse of fractures, and the M3.4 event is the result of such a collapse. The collapse could force fluid into other regions of the reservoir opening other fractures. If in fact major events trigger other events throughout the reservoir, as suggested by the analysis, then the reservoir is well-connected acoustically and has a high permeability. Further analysis is needed to determine if there are trends which might indicate the propagation of cracks.

2.7 3 Fault Size

The cluster shown in figure 22 displays the events closely correlated with the M3.4 event. Most of the events are within 150 meters of the M3.4 event and appear to be separated into two fracture lines. What is interesting about the configuration is that the main event seems to be at the vertex of the two lines. Examination of the clusters, by rotating a 3-D expanded image, indicates that the “clusters” associated with the M3.4 event are oriented at approximately 65° west of North, with many of the events aligned in a vertical orientation (see figure 30).

The alignment of the group of events is consistent with the focal mechanism for the M3.4 event determined by the Swiss Seismological Survey, whose moment tensor solution yielded a strike of -60°, a dip of 99°, and a rake of 162° (see figure 31). The dip of 99° is close to the vertical alignment of the events in the cluster, and the rake is consistent with the overall values that were found for events in the cloud (see the histogram in figure 33). This agreement suggests that members of this cluster shared the fault plane of the M3.4 event. Assuming that this is true, an estimate of the area of the fault plane of 21,000 m^2 was made by examining the locations of the events. This estimate is independent of the form of the seismogram which was used to calculate the seismic moment. This corresponds to a fault radius of ~80 m, extremely close to the source radius (82.4 m from the P-wave and 38 m from the S-wave) calculated from fitting the velocity spectrum (see next chapter). From the seismic moment of 6.28e12 Nm and a shear modulus of 30GPa the slip along the fault for the M3.4 event is estimated to be ~1cm.

The agreement between the fault plane determined from the event locations and the calculated focal mechanism is additional evidence in support of the accuracy of the double-difference algorithm. This technique is a powerful tool for the examination of hydro-fractured reservoirs.

2.8 Focal Mechanisms

2.8.1 Procedure

Focal mechanisms of earthquakes can provide important information regarding the structure of faults and the accompanying stress fields. For earthquakes greater than M4.5, the focal mechanisms can be found by inverting the seismic waveforms. Unfortunately, for smaller quakes this procedure is not reliable. In order to determine the focal mechanisms, we followed the prescription of Hardebeck and Shearer (2002, 2003), HASH, which relies upon a combination of P-wave first-motion and S/P amplitude ratios.

The determination of the focal mechanism consists of finding the strike, dip, and rake of the earthquake. This information is usually displayed in a seismic "beach ball." The beach ball shows a reference sphere divided into four quadrants, two in which the first motion is away from the quake, and two in which it is toward the quake. This is the classic double-couple approximation, which assumes only shear motion on the fault plane. When the P-wave first-motion is determined at each station, the focal mechanism can be calculated for a given model velocity and event location. This procedure can have uncertainties arising from several factors: a) An incorrect assignment of first-motion direction, b) The earthquake velocity model is wrong, and so the event location is in error. These cause the take-off angle and azimuth to be in error. These uncertainties result in an incorrect focal mechanism.

The standard procedure developed by Reasenberg and Oppenheimer (1985) uses a grid search over possible strike, dip and rake values to determine the best focal

mechanism. Their program, FPFIT, finds the minimum-misfit solution, that is the solution where the number of polarity observations which disagree with the quadrant in which they appear is minimized. The strike, dip, and rake are varied while keeping the number of misfits below a level. This serves to determine the quality of the fault-plane solution. The FPFIT procedure accounts for errors in the P-wave polarities, but does not account for possible errors in the takeoff angle (Hardebeck and Shearer, 2002). The HASH routine includes the possibility of possible errors in the velocity model and the resultant error in the source location. This is accomplished by testing multiple combinations of reasonable locations and velocity structures, and a list of solutions which fit at least a given fraction of polarity observations is obtained (Hardebeck and Shearer, 2002).

The procedure used in the HASH routine for the first-motion analysis consists of (Hardebeck and Shearer, 2002):

a) Use a grid search to find al acceptable solutions: those with misfit polarities below a fixed value.

b) Perturb source location.

c) Compute new ray azimuths and takeoff angles.

d) Find all acceptable solutions

e) Perturb source location and repeat.

In addition, the HASH routine uses information about the S/P amplitude ratios to constrain the focal mechanisms. The usability of the S/P amplitude ratios has been discussed in several papers (see for example, Kisslinger, 1980; Julian and Foulger, 1996;

Rau *et al*, 1996). The S/P amplitude ratios can be used to determine the focal mechanism, because the P-wave and S-wave amplitudes are largest at different points in the reference sphere. P-wave amplitudes are largest near the P- and T-axes while the S-wave amplitude is largest near the nodal planes. Uncertainties arise from attenuation and site effects when the S- and P-waves are affected differently. There also exists the possibility that the calculation of the amplitudes is affected by the noise in the signal.

The quality of the solutions is rated (Hardebeck and Shearer, 2002). Quality A requires an RMS difference of $\leq 25^{o}$, $\geq 90\%$ of the mechanisms within 30^{o} of the preferred mechanism, a misfit of $\leq 15\%$ of the polarities and an STDR (station distribution ratio, which quantifies how the observations are spaced on on the focal plane) ≥ 0.5. Quality B requires an RMS difference of $\leq 35^{o}$, $\geq 60\%$ of the mechanisms within 30^{o} of the preferred mechanism, a misfit of $\leq 20\%$ of the polarities and an STDR ≥ 0.4. Quality C requires an RMS difference of $\leq 45^{o}$, $\geq 50\%$ of the mechanisms within 30^{o} of the preferred mechanism, a misfit of $\leq 30\%$ of the polarities and an STDR ≥ 0.3. All others are quality D.

The HASH routine was modified to run using MATLAB by Eylon Shalev. Several calculations were required before the program could be used with the Basel data. The first step was to change the event locations from a modified UTM to latitude/longitude. To arrive at the P-wave first-motion values, a window of 50 ms was created beginning 10ms before the P-wave arrival time. The waveform that is used was the vertical sensor of the OT2 station, which, as described above, has a significantly better signal-to-noise than the other stations. This waveform, after being processed by a

Butterworth low-pass filter with a cutoff of 50Hz, was integrated over the window with a positive result corresponding to a positive P-wave polarity and a negative result with a negative P-wave polarity. The S/P amplitude ratio was determined by scanning the waveform in the vicinity of the S and P arrival times and finding the maximum value. The noise of the wave is determined by scanning the waveform prior to the arrival times and finding the magnitude. Only solutions where the signal-to-noise ratio is greater than 3 are used.

2.8.2 Results

Of the 3000 events, only 60 were categorized as quality C. There were no events of quality A or B. I attribute this to the small number of receiving stations and the weakness of the events. With so few stations, it is difficult to narrow the range of nodal planes to qualify for a higher grade. Note that not all events are seen by all stations. This result is similar to the result found for the Puna, Hawaii data set, where the first-motion polarities were determined by a different routine. In the Puna case, only 20 out of 1800 events had reliably determined focal mechanisms. Again, the suspicion is that the few number of stations (6) is responsible for the lack of determined mechanisms.

The events for which focal mechanisms were reliably determined are displayed in figure 32 using Mirone software (Luis, 2007) and the locations with the strike, dip and rake are given in Table 4.

To assist in the interpretation of the results, figure 33 displays histograms showing the distribution of angles for the strike, dip, and rake. While the strike and dip

have fairly uniform distributions, the rake is closer to ± 180 degrees indicating that the predominant mechanism is a strike slip with a right lateral motion.

2.8.3 Discussion

While very few of the focal mechanisms could be determined reliably, the predominance of the strike-slip mechanism for those that were determined is consistent with results from other studies of the southern Rhine Graben and northern alpine region (Meghraoui *et al*, 2001). This suggests that the underlying fault structure of the region is being tapped in the hydro-fracturing of the reservoir.

2.9 Conclusion

In this study, the locations of the microseisms have been determined and used to describe the dynamics of the reservoir. The reservoir grew at a fairly steady rate, which was determined by the flow rate and input pressure. During the development of the reservoir, the opening of fissures occurred throughout the reservoir, not just at the outer boundary, and events which were close chronologically were not necessarily spatially related. The steady growth was punctuated by fluctuations that closely followed sudden changes in flow rate/pressure, which also appeared to trigger larger events. These jumps in reservoir size could be the result of the larger events opening cracks throughout the reservoir. The dominant mechanism for events triggered by the stimulation is strike-slip with right-lateral motion. The cluster of events highly correlated with the M3.4 event indicate that the fault plane associated with the M3.4 event appears to have a radius of ~80m and is vertically aligned along a direction 65° west of North. The focal mechanism

determined by the Swiss Seismological Survey is consistent with the orientation of the fault plane associated with the M3.4 event.

Table 2: Velocity Model

	Depth (m)	V_p(m/s)	V_s(m/s)
Layer 1	0-2265	3980	2080
Layer 2	>2265	5940	3450

Table 3: Arrival Time Correction

Station	S-wave (s)	P-wave (s)
Otterbach 2	0	0
Otterbach 1	0	0
Haltingen	0.023	0.007
St. Johann	0.018	-0.006
Schutzenmatte	0.021	-0.005
Riehen 2	0.097	0.073

Table 4: Focal Mechanisms

Longitude	Latitude	Depth(km)	Strike	Dip	Rake
7.593400	47.586080	4.580	358	22	-104
7.593860	47.585650	4.570	321	37	-136
7.594400	47.585370	4.580	318	70	-150
7.592690	47.585950	4.820	305	82	140
7.594370	47.585310	4.620	224	13	-146
7.594320	47.585930	4.250	84	57	124
7.593590	47.585660	4.530	220	80	-120
7.594270	47.585440	4.530	221	28	-95
7.592770	47.586460	4.640	293	45	142
7.594530	47.584860	4.560	136	83	-133
7.593920	47.585480	4.600	320	12	174
7.591900	47.586150	4.620	138	88	-143
7.594460	47.584620	4.730	136	90	-114
7.595880	47.585190	4.250	4	32	-27
7.594360	47.585590	4.310	197	72	161
7.592090	47.586660	4.650	207	44	-100
7.595550	47.583380	4.810	234	25	99
7.596000	47.583130	4.920	6	72	172
7.594540	47.585410	4.230	166	78	-130
7.593000	47.587520	4.700	303	87	-166
7.592510	47.587750	4.690	77	53	-94
7.595000	47.584010	5.100	7	9	120
7.592450	47.585890	4.620	232	20	-59
7.595760	47.586060	4.410	66	87	-140
7.592020	47.587740	4.680	256	15	67
7.594430	47.584890	4.280	14	14	-98
7.595390	47.584560	4.470	254	89	92
7.595700	47.585500	4.570	197	47	-172
7.594530	47.585140	4.410	328	79	98
7.593280	47.587480	4.450	153	49	-107
7.595920	47.584120	4.310	142	89	-110
7.592910	47.587050	4.820	191	45	-107
7.594760	47.583540	4.890	267	12	-146
7.594770	47.583500	4.880	200	34	-136
7.594200	47.584020	4.980	41	43	115
7.591840	47.586890	4.690	257	24	-91
7.594400	47.585170	4.430	173	81	-123
7.595700	47.582630	4.830	119	88	-84
7.594570	47.583730	4.900	327	77	151
7.594870	47.583410	4.540	200	51	161
7.594690	47.583110	4.680	10	20	-86
7.593710	47.584110	4.900	260	16	34
7.596390	47.582910	4.370	195	79	-177
7.593830	47.585030	5.050	228	73	-101
7.593740	47.584140	5.030	276	41	85

Table 3 Focal Mechanisms (Continued)

Longitude	Latitude	Depth(km)	Strike	Dip	Rake
7.595880	47.585440	4.470	260	88	139
7.593570	47.586150	4.990	39	12	1
7.591160	47.588550	4.630	163	37	75
7.593380	47.585230	4.990	200	31	170
7.596140	47.583020	5.000	193	44	-137
7.594100	47.584150	4.340	71	81	114
7.596560	47.584840	4.300	103	81	-124
7.591500	47.586120	5.060	259	37	-161
7.591910	47.588440	4.520	197	83	137
7.592490	47.588380	4.520	182	42	-163
7.596890	47.585780	4.270	135	56	165
7.595490	47.584720	4.480	285	13	-82
7.595360	47.584760	4.490	319	46	-97
7.597240	47.585460	4.280	273	80	97
7.596500	47.584150	4.310	80	13	36
7.592760	47.588390	4.420	48	10	-16

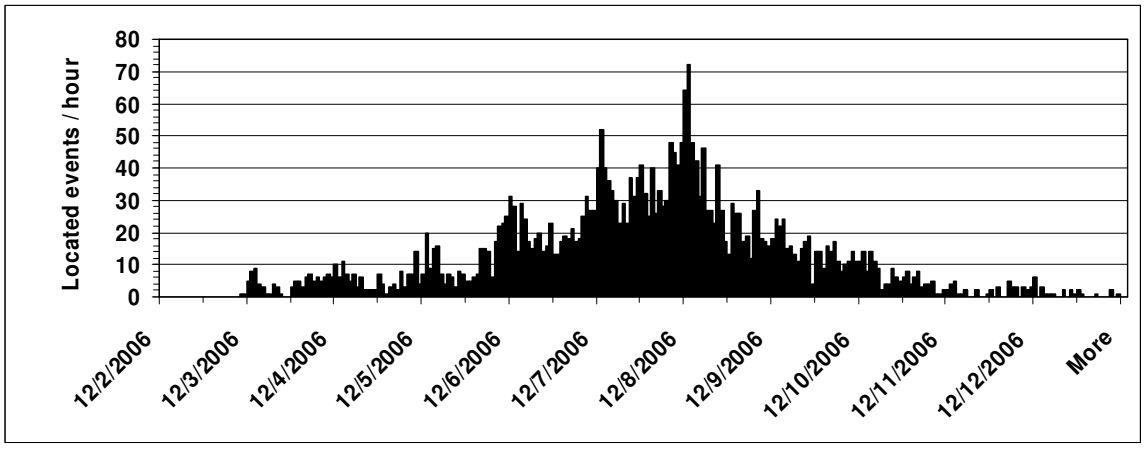

(a)

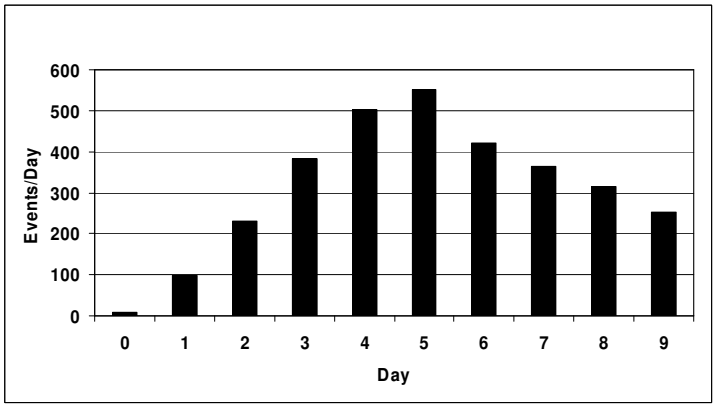

(b)

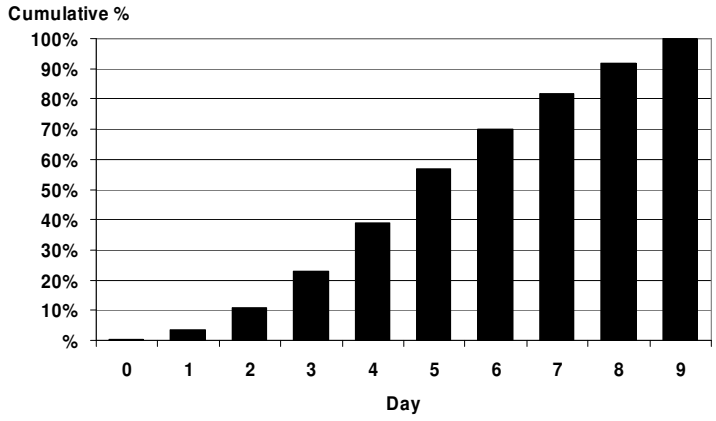

Figure 18: Locatable events

(a) The number of locatable events per hour during the main stimulation and in the days following. The frequency of events was low for the first day and peaked December 8, 2006, the date of the Magnitude 3.4 event. c. (b) The number of events per day during the main stimulation and in the days following. Day zero corresponds to December 2, 2006. (c) The cumulative number of events as a percentage of the total for 9 days. Day zero corresponds to December 2, 2006.

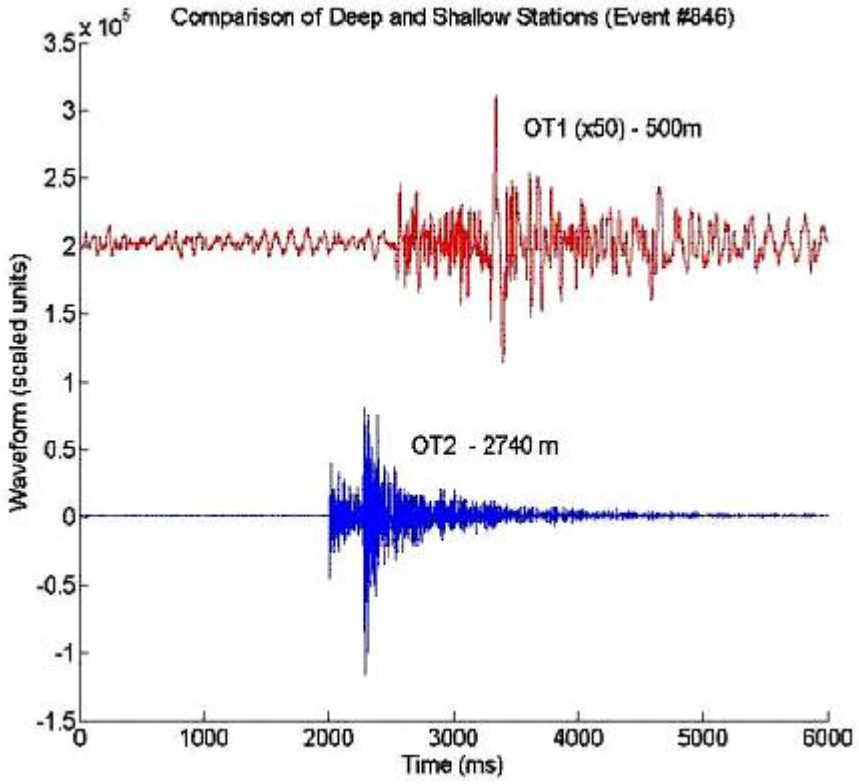

Figure 19: Seismographs from OT1 and OT2.
Seismographs from Otterbach 1 and Otterbach 2 showing higher resolution for deeper station. Depths are given. Note OT1 waveform is multiplied by 50.

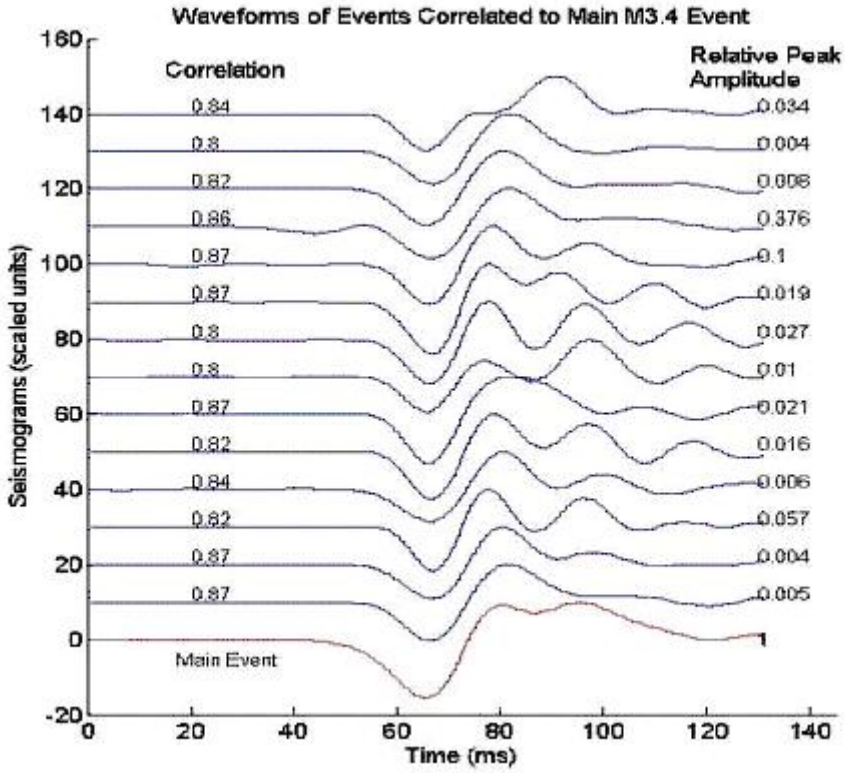

Figure 20:Seismographs of events in the M3.4 cluster.
The M3.4 eventis at the bottom. The relative amplitude of the peak is given at the right. All waveforms are from OT2

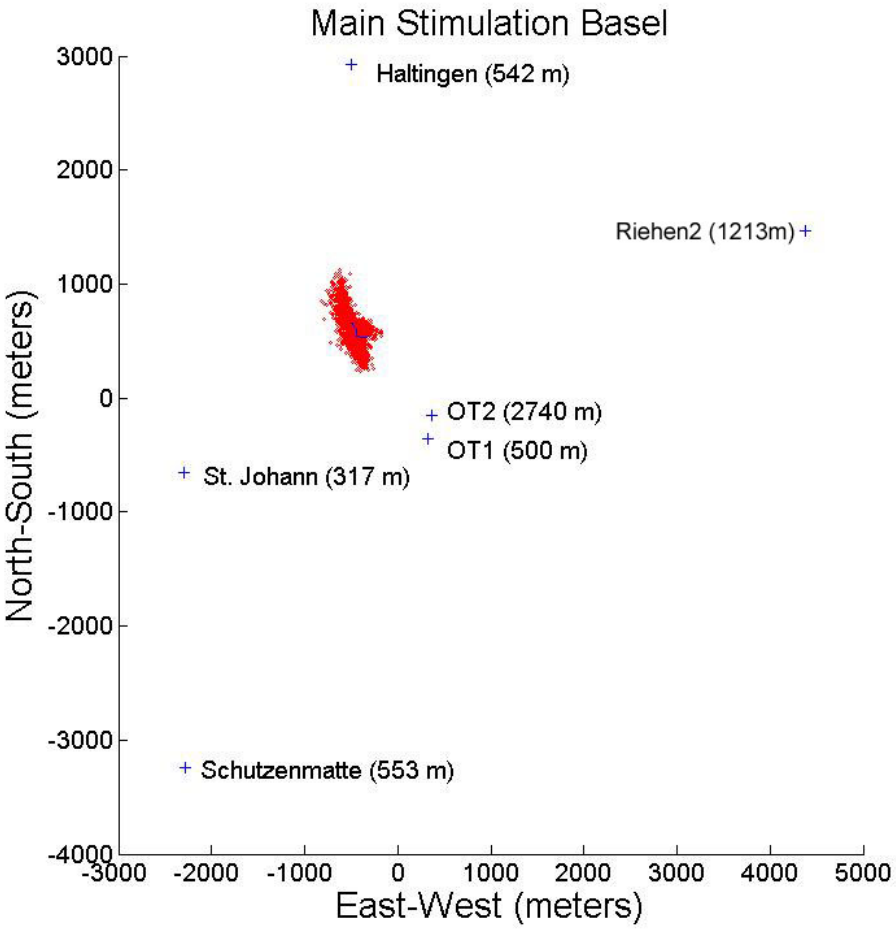
Main Stimulation Basel
Haltingen (542 m)
Riehen2 (1213m)
OT2 (2740 m)
OT1 (500 m)
St. Johann (317 m)
Schutzenmatte (553 m)
North-South (meters)
East-West (meters)
3000
2000
1000
0
-1000
-2000
-3000
-4000
-3000
-2000
-1000
0
1000
2000
3000
4000
5000

(a)

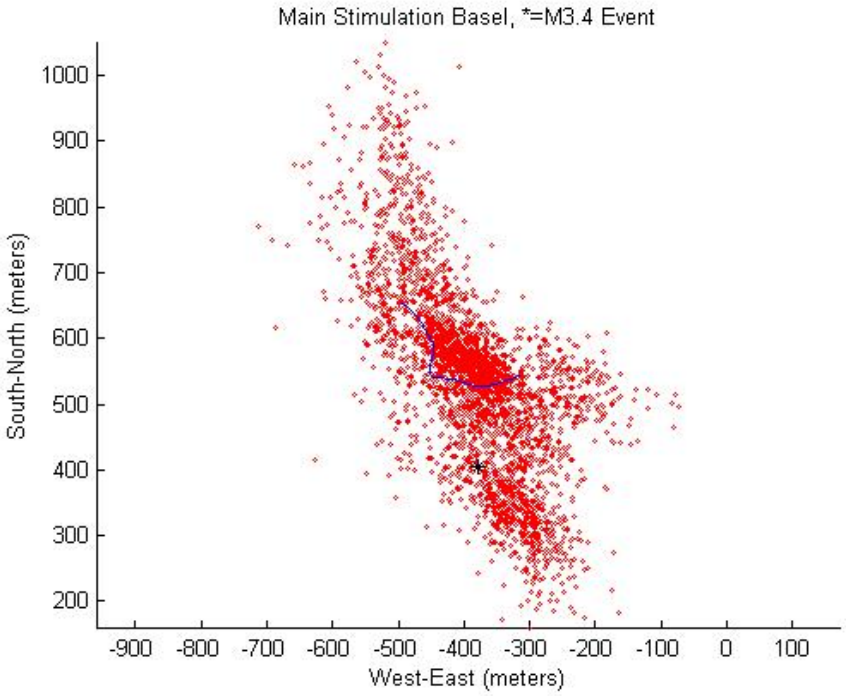
Main Stimulation Basel, *=M3.4 Event
South-North (meters)
West-East (meters)
1000
900
800
700
600
500
400
300
200
-900
-800
-700
-600
-500
-400
-300
-200
-100
0
100

(b)

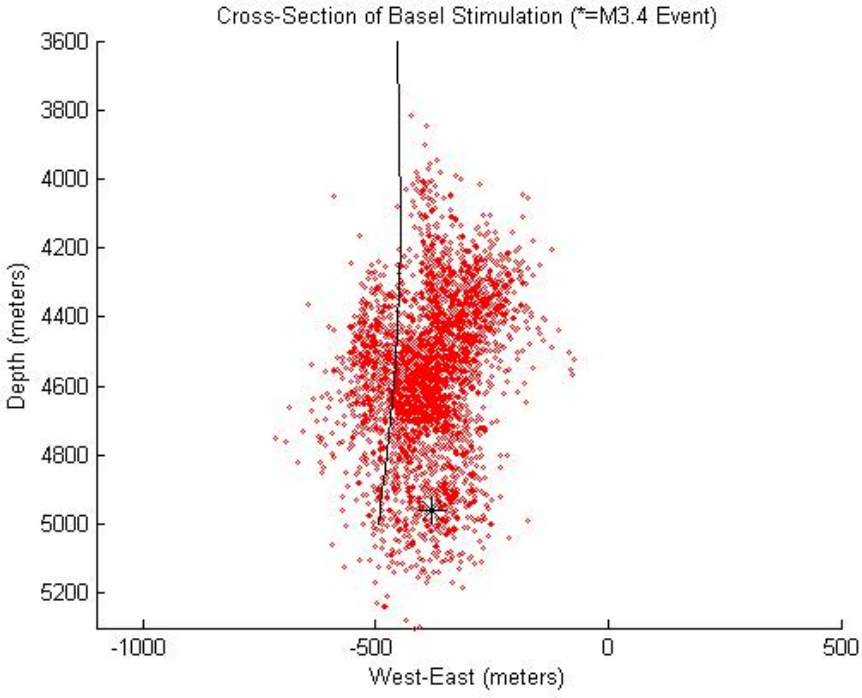
Cross-Section of Basel Stimulation (*=M3.4 Event)
Depth (meters)
West-East (meters)
3600
3800
4000
4200
4400
4600
4800
5000
5200
-1000
-500
0
500

(c)

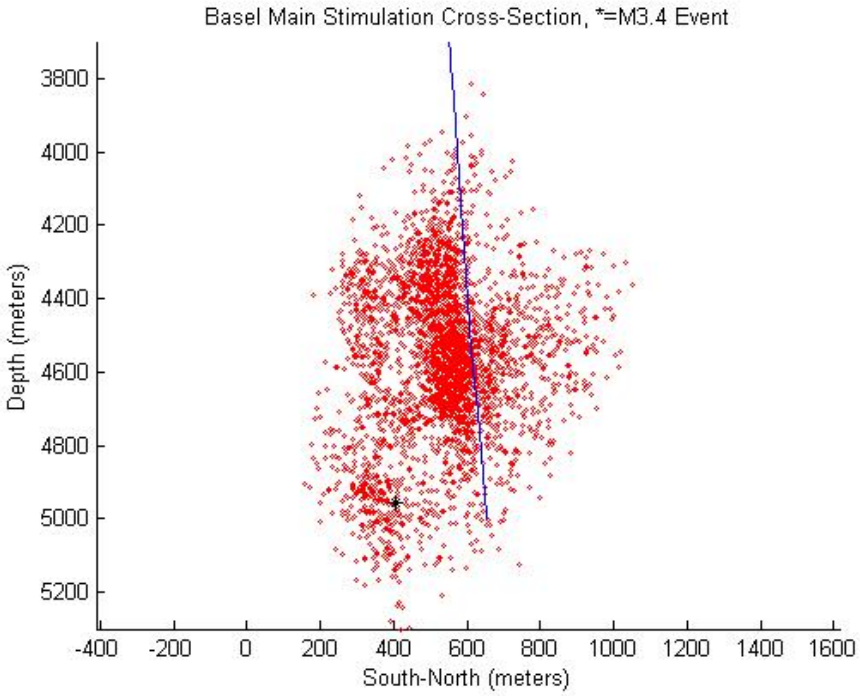

Figure 21: Microseism Cloud
(a) Map view of microseism cloud and sensor deployment. Depths of stations are shown in parentheses. Blue line is the borehole trajectory. (b) Map view of microseism cloud. Blue line is borehole trajectory. * indicates the location of the M3.4 event. (c) West-East cross-section of microseism cloud. Blue line is borehole trajectory. * indicates the location of the M3.4 event. (d) South-North cross-section of microseism cloud. Blue line is borehole trajectory.

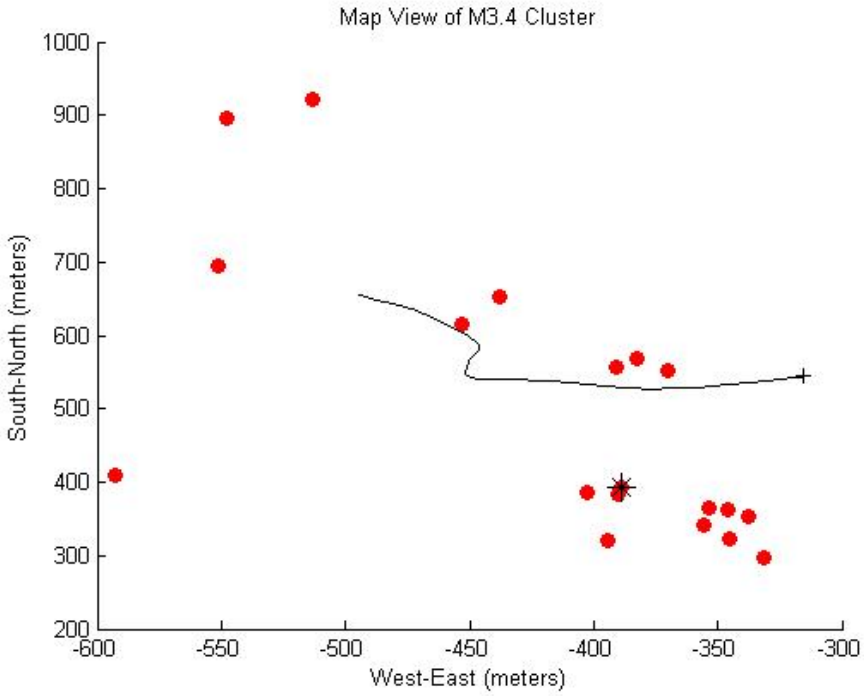
Map View of M3.4 Cluster
South-North (meters)
West-East (meters)
1000
900
800
700
600
500
400
300
200
-600
-550
-500
-450
-400
-350
-300

(a)

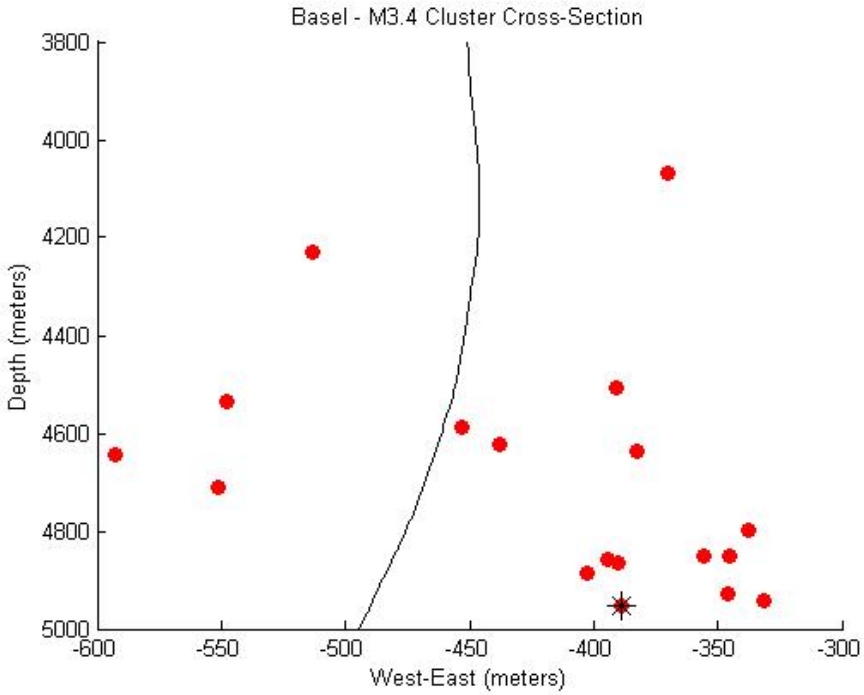
Basel - M3.4 Cluster Cross-Section
Depth (meters)
West-East (meters)
3800
4000
4200
4400
4600
4800
5000
-600
-550
-500
-450
-400
-350
-300

(b)

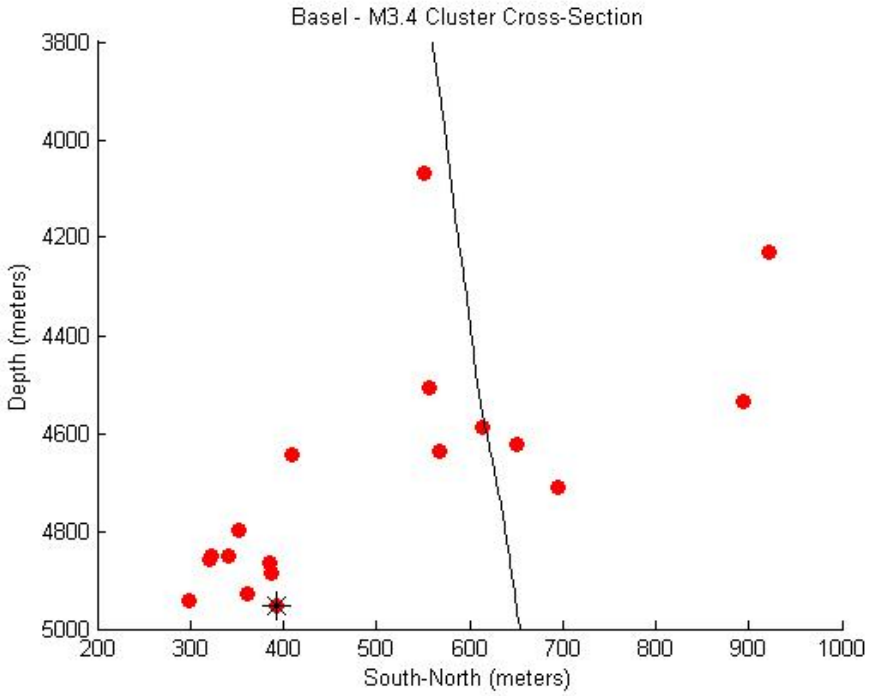

Figure 22: M3.4 Cluster
(a) Map view of M3.4 cluster. Black line is borehole trajectory; surface is at +. * indicates location of the M3.4 event. (b) . West-East cross-section of M3.4 cluster. Black line is borehole trajectory. * indicates location M3.4 event. (c) South-North cross-section of M3.4 cluster. Blue line is borehole trajectory. * indicates location M3.4 event

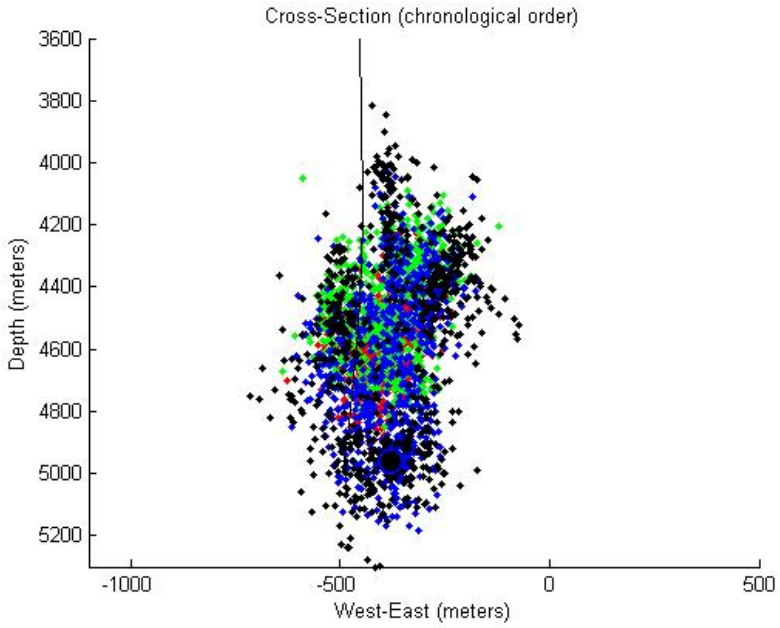

(a)

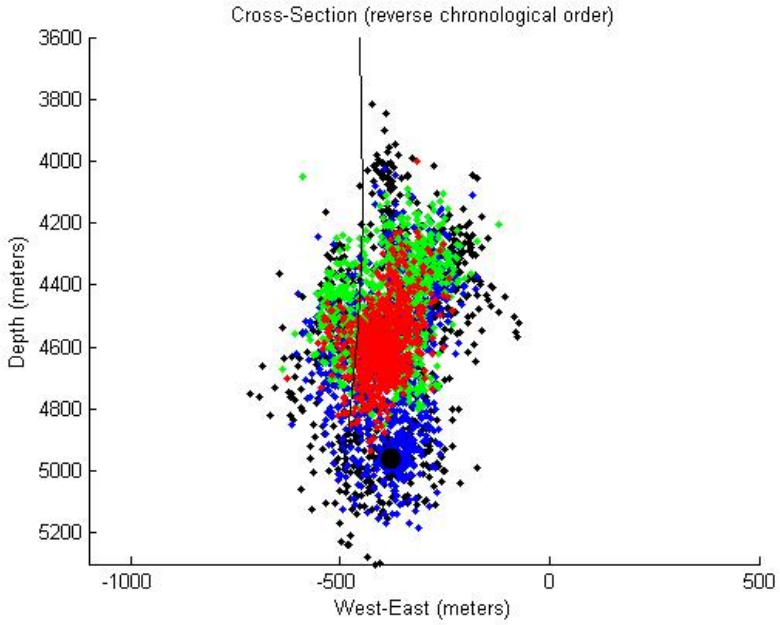

Figure 23: Time evolution of microseism cloud.
The time evolution of the microseism cloud. From earliest to latest red, green, blue, black. Each color depicts the location of 800 events. (a) The cloud is plotted with the earliest events first so that they are covered by the later events. (b) same as (a), but with the later points plotted first. The black line is the borehole trajectory and the large black circle is the M3.4 event.

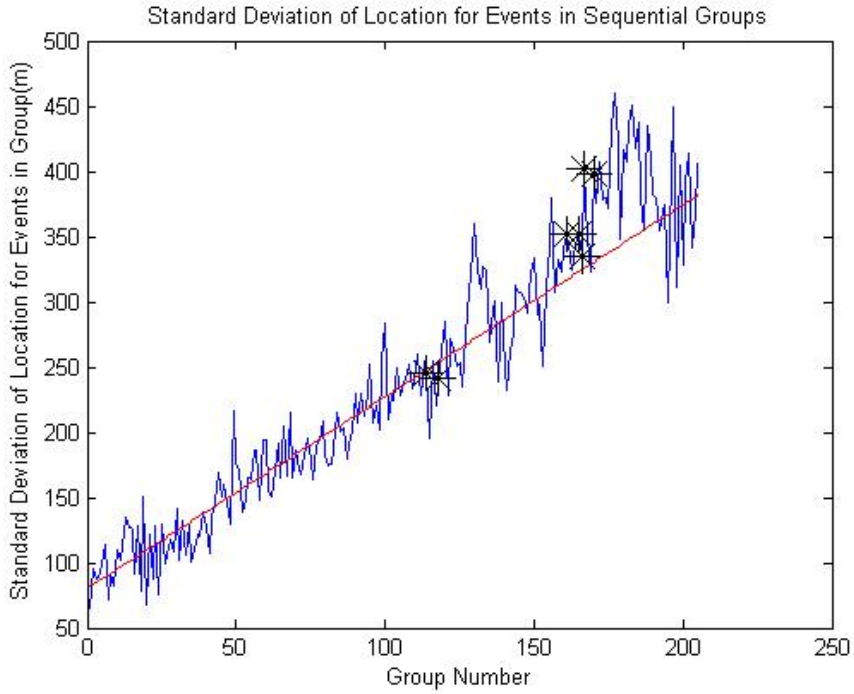

Figure 24: Growth of reservoir.
Standard deviation of event locations from mean position for groups consisting of 15 events. The straight line is the least-squares curve fit and the asterisks indicate the groups containing the 7 largest events that were located.

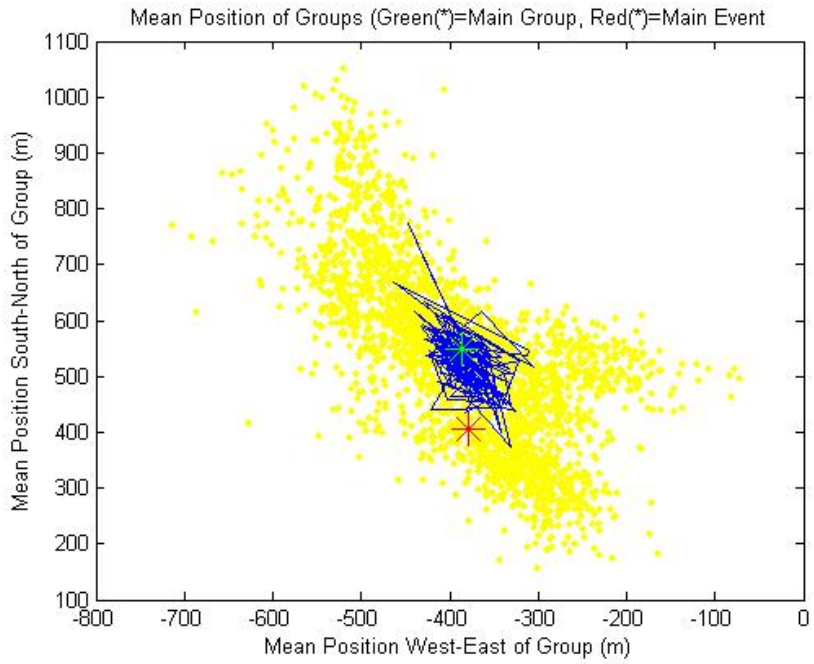

Figure 25: Trajectory of the means of the groups.
The yellow region indicates the microseism cloud. The green asterisk is the mean of the group containing the M3.4 event, whose location is given by the re asterisk.

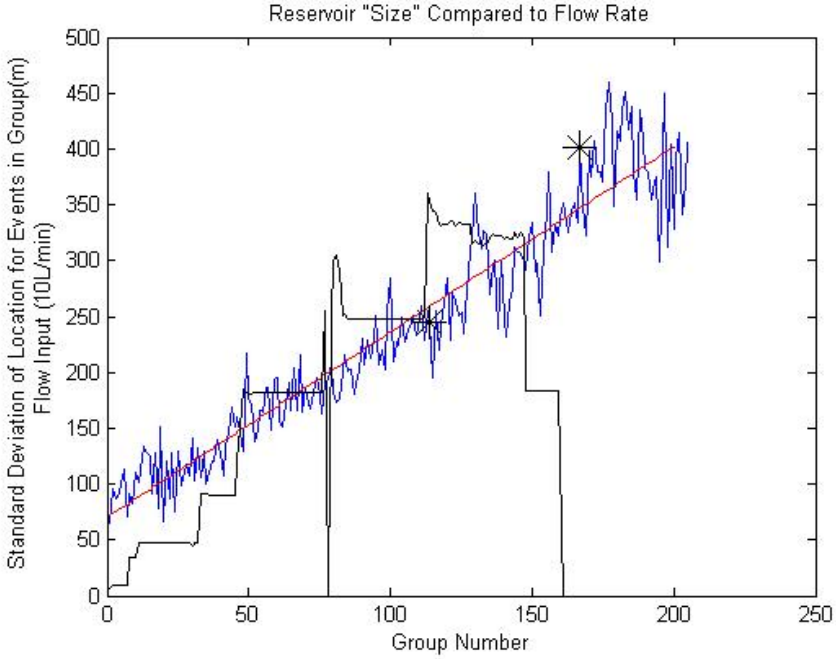

Figure 26: Comparison of the injection flow rate to the reservoir "size"
The straight line is the least-squares fit to the reservoir size. The asterisks denote the two largest events.

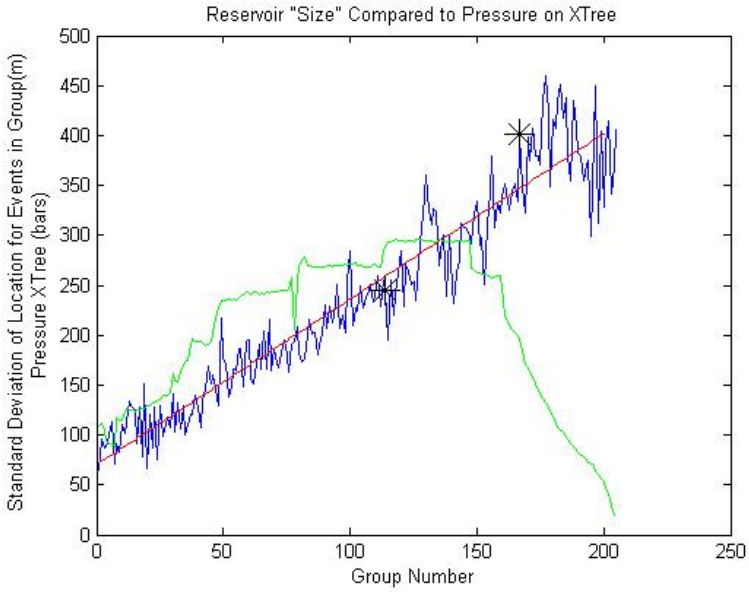

Figure 27: Comparison of the pressure at the X-tree to the reservoir size. The straight line is the least-squares fit to the reservoir size. The asterisks denote the two largest events.

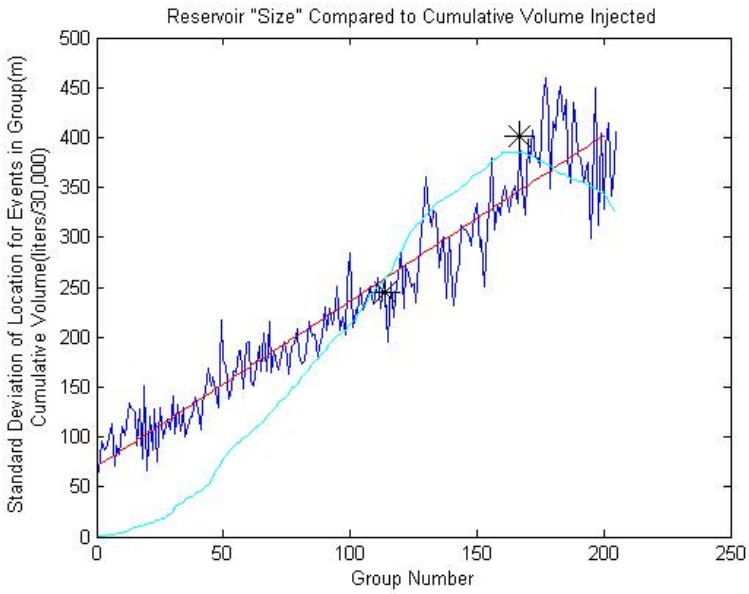

Figure 28: Comparison of the cumulative injected fluid to the reservoir size. The decrease occurs when fluid is being returned. The straight line is the least-squares fit to the reservoir size. The asterisks denote the two largest events.

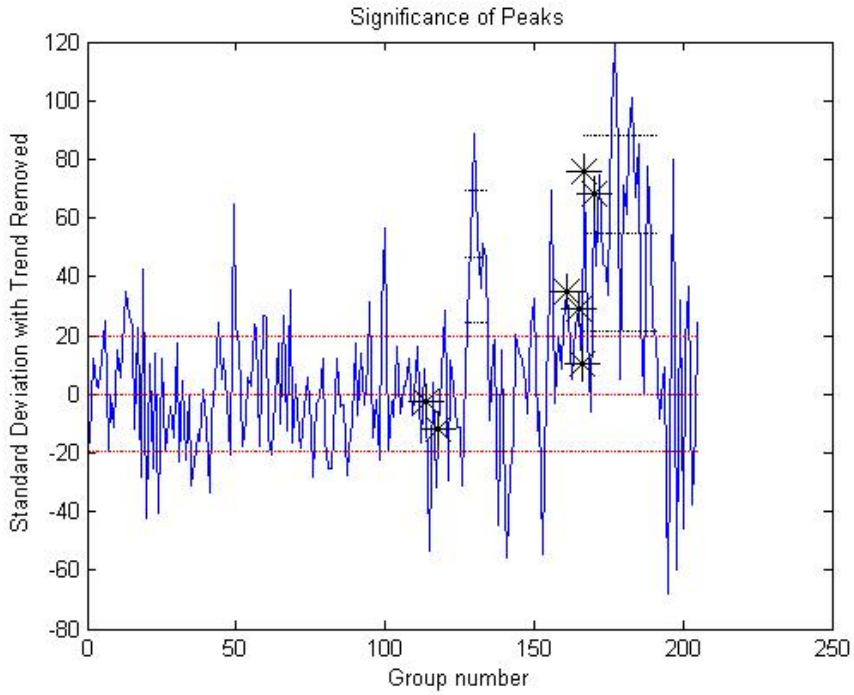

Figure 29: Data from figure 28 with trend line subtracted
Red horizontal lines show mean and standard deviation of the main section, while the black horizontal lines show means and standard deviations of the two fluctuations. The asterisks denote the largest events.

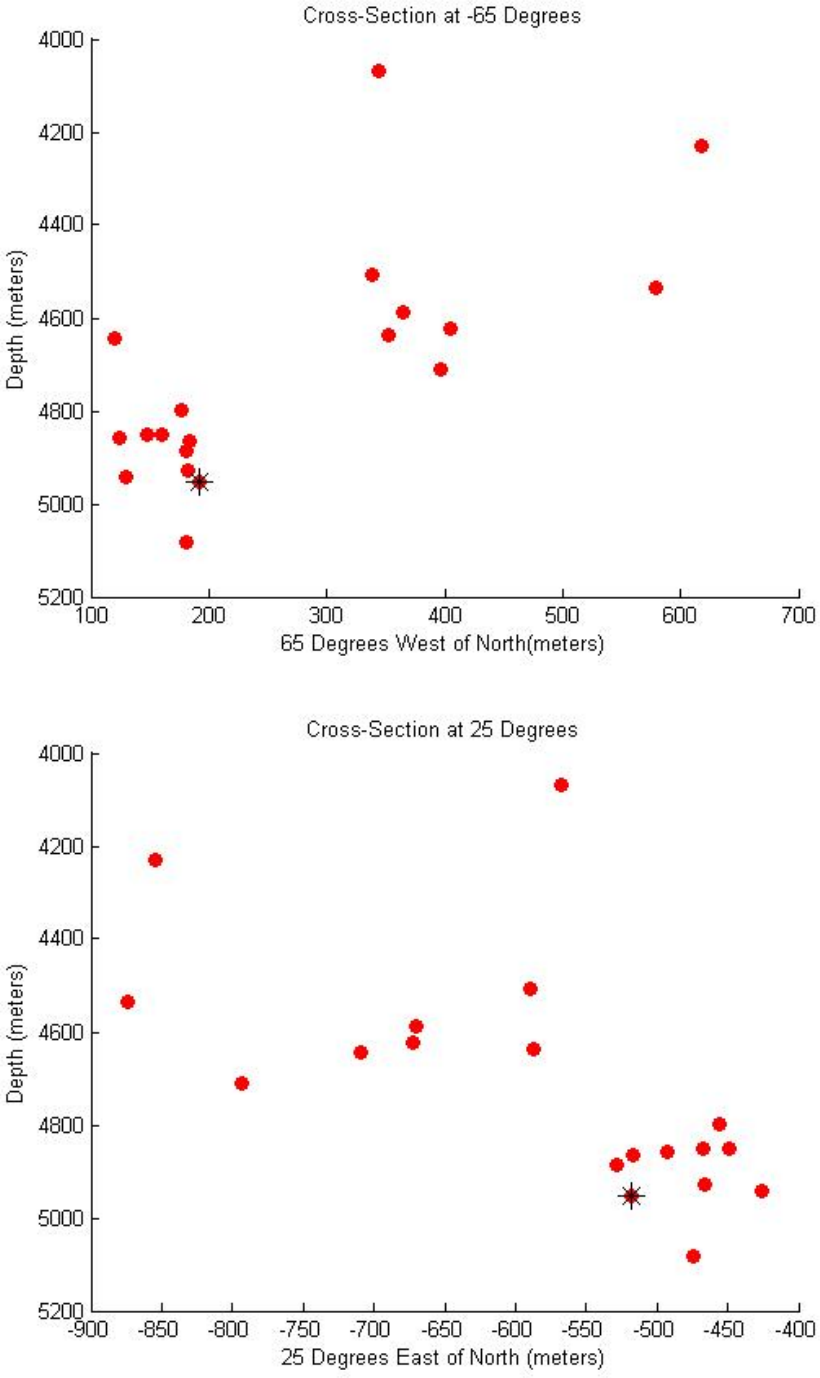

Figure 30: Rotated cross-section plots of M3.4 cluster.
(a) Rotated cross-section plots of M3.4 cluster (65° west of North). Group of events with vertical alignment are seen in the lower left of the figure. (b) Perpendicular view (25° east of North) showing cross-section of fracture plane, lower right.

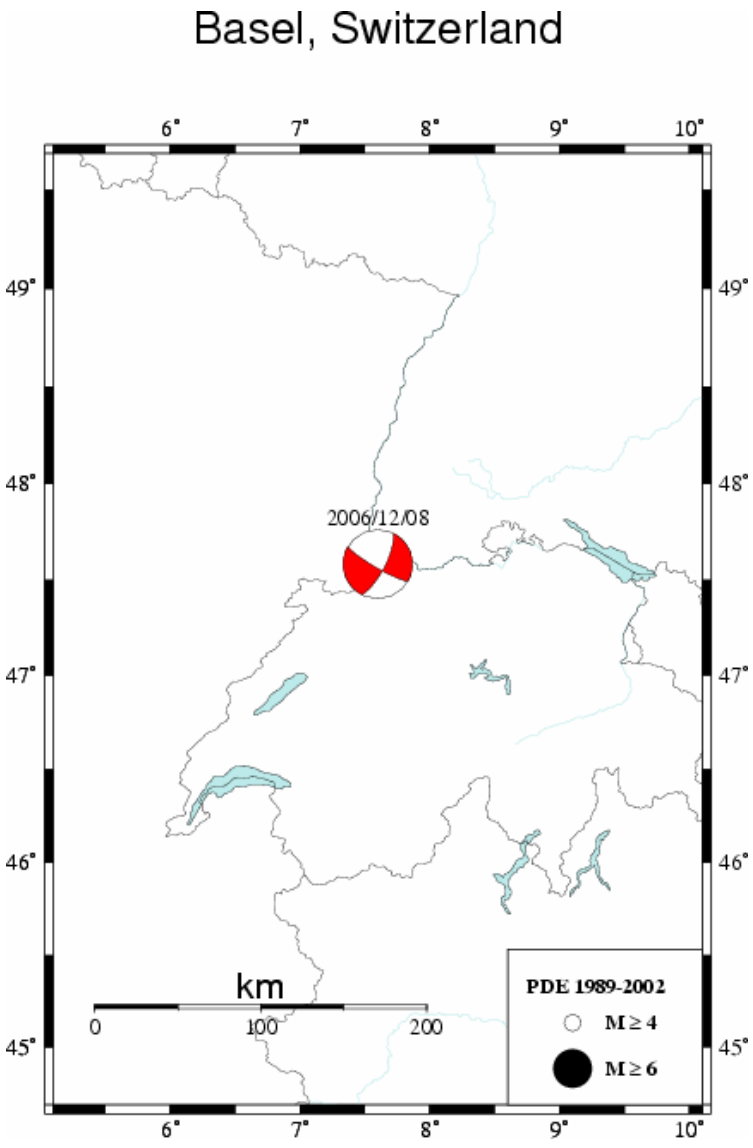

Figure 31: Focal mechanism of the M3.4 event. Determination by the Swiss Seismological Survey.

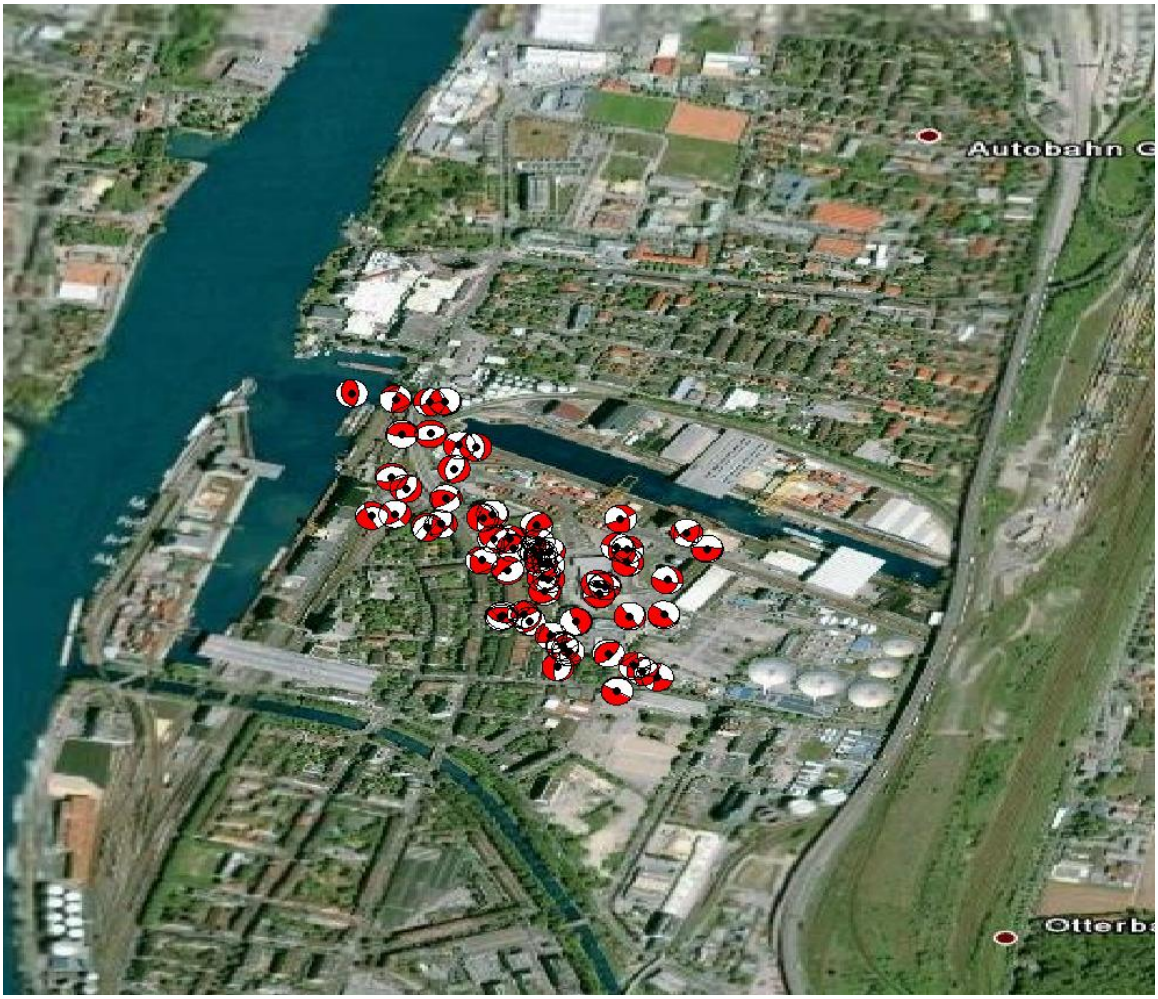

Figure 32: Beach ball focal mechanisms for selected events.

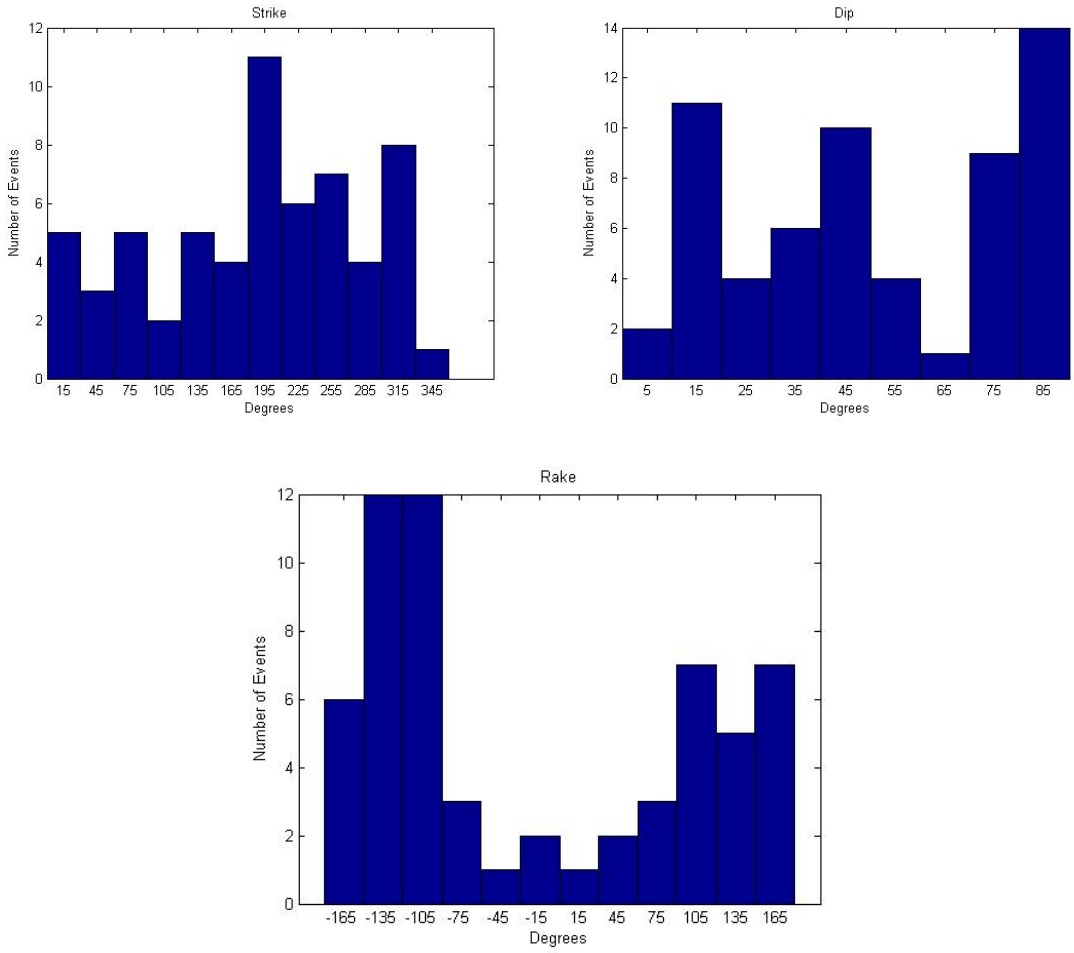

Figure 33: Histograms of focal mechanism parameters.
Histograms showing distribution of the a) strike , b) dip , and c) rake for the identified mechanisms.

Chapter 3

3. Source Scaling Relations

3.1 Introduction

An important topic in seismology is the question of scaling relations of earthquakes. Are small quakes (magnitude < 2) simply large quakes scaled down? Numerous studies (see for example: Kanamori *et al* (1993), Singh and Ordaz (1994), Abercrombie (1995), Mayeda and Walter (1996), Izutani and Kanamori (2001), Prejean and Ellsworth (2001), Richardson and Jordan (2002), Kanamori and Anderson (1975), Choy and Boatwright (1995), McGarr (1999), Ide and Beroza (2001), Ide et al. (2003)) have examined this question with mixed results. The last five references found a constant ratio of radiated energy to seismic moment, in keeping with the scaling hypothesis. The first seven found an increase in the ratio with increasing moment, suggesting that small and large quakes are fundamentally different. While these results appear to be in conflict, there are several explanations that might account for the disagreement:

1) Large uncertainties in the seismic energy.
2) Large energy variability for different earthquakes with the same moments within the same study.
3) Lack of common events between studies, making comparisons of the different scalings difficult.

4) Limited studies using a single consistent technique covering a wide range of sizes (e.g., magnitude 2 to 8).

(Ryerson *et al,* 2003)

Other than radiated energy, another of the source parameters that is examined is the stress drop, the change in stress before and after the quake. The stress drop, which is the ratio of the seismic moment to source dimension cubed is hypothesized to be constant over many magnitudes (0 to 7). The argument is that the seismic moment, M = rigidity*fault area*slip, is proportional to the length-scale cubed, so when it is divided by the source dimension cubed (the radius, for example), a constant will result. However, because of the difficulty in separating the effects of source, path, and site, it was difficult to verify the scaling relationships below magnitude 3. Below this magnitude the source dimension previously appeared to have a constant value of about 100m; therefore, the stress drop decreased with decreasing moment. While there were arguments that supported this length as the typical width of a fault zone, it was also suggested that the attenuation seen in surface stations was responsible for the breakdown. This attenuation was particularly important for high frequencies (>50 Hz), because the short wavelengths could serve to restrict the source size. As a result studies are now using relatively deep (~3 km) sites to eliminate near-surface attenuation and determine whether the scaling relations hold.

In this study, I will use the data acquired during the Basel hydro-fracture stimulation, which occurred during December 2006, to examine the source scaling parameters for the ~3000 events that were recorded during a one week period. These

events, which vary in magnitude from approximately -1 to 3.4, have been located with a double-difference algorithm and form a robust data set for this study. The data set has the further advantage that the events were highly localized and that a nearby sensor at 2740m in depth recorded the events.

3.2 Source Scaling Relations

In this section the basic expressions for the source parameters are presented. The velocity spectrum has been represented by Brune (1970) and Boatwright (1980), using the so-called omega-square relation:

$$\Omega(f) = \frac{f\Omega_o e^{-(\pi f t/Q)}}{\left[1+(f/f_c)^{\gamma n}\right]^{1/\gamma}} \qquad (1)$$

Here, Ω(f) is the velocity spectrum of either the S- or P-waves determined by the Fourier transform of the seismogram, Ω_o is the long period amplitude, f is the frequency, f_c is the corner frequency, t is the traveltime of the signal from the source to the receiver, Q is the quality factor (a measure of the damping), n is the high frequency fall off rate on a log-log plot, R is the hypocentral distance from the source to the receiver. When t=0, n=2, and γ=1, this is the formula proposed by Brune. The Boatwright used γ=2, which is the model that I will use in this study.

In most previous studies, the data (Fourier transform of the seismograms) were fitted to determine the parameters Ω_o, f_c, and Q. Various methods were used including, setting t=0, setting Q_P=Q_S =1000 and varying the parameter, n. The different models

yielded comparable fits of the data with no impact on the conclusions regarding the validity of the scaling hypothesis.

There are a couple of models for the source dimension. These models assume that the source dimension is reliably described by the source radius assuming a circular crack model. With this assumption, Madariaga (1976) derived a relation,

$$r = \frac{3k\beta}{(f_c(Z) + f_c(H1) + f_c(H2))} \tag{2}$$

where β= is the S-wave speed and k=0.32 for P waves and k=0.21 for S waves.
Sato and Hirasawa (1973) arrived at the expression,

$$r = \frac{CV}{2\pi f_c} \tag{3}$$

where, C is a coefficient dependent on the rupture velocity, and V is the relevant wave velocity (S or P). While the similarity of the two formulas is evident, in this study I will use the Madariaga model, because of the use of the corner frequencies from all three sensors.

The static stress drop is defined as the difference between the initial equilibrium stress and the final equilibrium stress in the source region. Mathematically it is written as (Aki, 1972),

$$\Delta\tau = C\mu\left(\frac{d}{r}\right) \tag{4}$$

with C being a constant, μ the shear modulus, and d the slip distance. For a circular rupture model, the static stress drop was found by Eshelby (1957) to be,

$$\Delta\tau = \left(\frac{7}{16}\right)\left(\frac{M_o}{r^3}\right) \tag{5}$$

with M_o being the seismic moment, which can be determined by (Keilis-Borok, 1960):

$$M_o = \frac{2\rho V^3 R\sqrt{\Omega_o(Z)^2 + \Omega_o(H1)^2 + \Omega_o(H2)^2}}{U_{\phi\theta}} \tag{6}$$

where, ρ is the density and $U_{\varphi\theta}$ is the mean radiation pattern (0.52 for P waves and 0.63 for S waves).

By fitting the seismic wave form to find the corner frequencies and the long period amplitudes, the moment can be estimated, from which the static stress drop, Δτ, can be calculated. If earthquakes scale, Δτ should be relatively constant over a wide range of magnitudes.

The radiated seismic energy is also an important characteristic of quakes for the determination of whether scaling is valid. Boatwright and Fletcher (1984) describe the radiated energy

$$E_{S/P} = \frac{4\pi\rho V R^2 < U_{\varphi\theta} >}{U_{\varphi\theta}}\left[I(Z) + I(H1) + I(H2)\right] \tag{7}$$

with <U>=U as an approximation and $I = \int_0^\infty \dot{u}(\omega)^2 d\omega$ an integral of the velocity spectrum. A similar expression was derived by Vassiliou and Kanamori (1982),

$$E_R = \left(\frac{1}{15\pi\rho V_p^5}\right)\int (2\pi f)^2 \left|M_o^P(f)\right|^2 df + \left(\frac{1}{10\pi\rho V_s^5}\right)\int (2\pi f)^2 \left|M_o^S(f)\right|^2 df \qquad (8)$$

Here $M_o(f)$ is the moment rate spectrum, calculated by stacking the ratios between the observed spectrum and attenuation function for each level of the array and component. I will use the expression of Boatwright and Fletcher.

The radiated energy, which describes the portion of the total strain energy released that is transformed to acoustic energy, is another source parameter of interest.

$$E_R = \eta \Delta W \qquad (9)$$

Here η is the efficiency and ΔW is the change in strain energy. Writing

$$\Delta W = Ad\sigma \qquad (10)$$

with A the area of the fault and σ the mean stress, and identifying $\eta\sigma=\tau_a$ as the apparent stress, the apparent stress can then be calculated by

$$\tau_a = \mu \frac{E_R}{M_o} \qquad (11)$$

(Wyss and Brune, 1968).

The apparent stress is also referred to as the scaled energy (Kanamori and Heaton, 2000), since dividing the radiated energy by the seismic moment, $M_o=\mu Ad$, is equivalent to dividing the energy by a volume. Since the energy of a quake is expected to be proportional to the volume, this ratio is expected to be constant.

3.3 Brief Review of Previous Techniques

In 1995, Abercrombie did the seminal study using data from a triaxial set of 10Hz high temperature geophones deployed at depth of 2.5km in the Cajon Pass scientific drill

hole about 4km from the San Andreas Fault. The sample rates were between 500 and 1000 samples/sec. It was important to use deep sensors because downhole seismograms contain higher frequency components and show a higher signal-to-noise ratio. One second windows were used for the smallest events (<M3), 2 second windows for M3 to M4. At the depth of the sensors, the seismic paths had not been refracted to vertical so all three components saw both S and P waves. Abercrombie found:

1) No breakdown in self similarity below magnitude 3 (source dimensions ~10 meters).
2) The ratio of radiated seismic energy to seismic moment (apparent stress) decreasing gradually with decreasing moment.
3) The ratio of S-radiated energy to P-radiated energy to be ~14 after correcting Q factors.
4) Intrinsic attenuation to be very low below 2.5 km. Q~1000.
5) That n=2 was good average value.

In a recent study by Imanishi and Ellsworth (2006), thirty-two 3-component geophones were spaced at 40 meter intervals from 856 to 2096m below surface. They chose quakes whose S-P time differences were <1 second. The cross-correlation coefficients of all combinations of quakes at all levels of the array were calculated and they demanded that cross-correlation coefficients be >0.8 between a pair of quakes at 10 or more levels so that only similar quakes would be included. A passband-filtered (10-15 Hz) seismogram in a time window extending 1.5 seconds beyond the direct P-arrival time was used so that the window contained both P and S waves. Demanding a common focal mechanism, the 34 events were divided into into 14 clusters. A moving overlapping

window (0.1 seconds in width for P-waves and 0.2 seconds in width for S-waves) shifted by 0.05 seconds was used, with total of 5 windows. The spectral ratios were obtained by stacking the ratios calculated in the multi-window taken along the record following the direct wave. The goal was to use stacking to suppress the noise resulting from different paths. Boatwright's (1978) omega-square relation was used to determine moments and corner frequencies. They found no breakdown in constancy of stress drops, even below M0.

3.4 Basel Reservoir

3.4.1 Data Acquisition

The data set used to examine source parameter scaling came from the Basel Deep Heat Mining Project hydro-fracture stimulation occurring between December 2 and December 8, 2006. This is a valuable data set because during the stimulation a M3.4 event was triggered and so it includes events with a range of magnitudes and similar origins. Analysis of the events also indicates that the events were localized with in a 2 kilometer region (see Chapter 2).

To record the events a set of six geophones were deployed ranging in depth from ~317 to ~2740 meters. The properties of the geophones are described in Chapter 2 (see Table 1).

3.4.2 Data Analysis

The data set used to determine the source scaling parameters consisted of over 3000 events. To analyze this data set, several steps with accompanying approximations and assumptions had to be taken. The first step in the analysis was the determination of the events which were sufficiently similar to be used in a double-difference location calculation (described in Chapter 1). To make this determination, the cross-correlation coefficients for the events were calculated and a threshold of 0.85 was used to select those events which would be used in the calculation. The resulting locations were the ones that were used for determination of the source parameters. All of the scaling analysis was derived from the seismograms from the Otterbach 2 sensor (OT2), which was the deepest and closest to the seismic cloud that was stimulated. This sensor had a signal to noise ratio which was more than a factor of 10 better than any of the other sensors due to its depth, proximity to the events, and design (see figure 20).

To determine the velocity spectrum, the data from the three components of OT2 were used. A window of 0.2 seconds beginning 10 ms before the trigger point of the P-wave was used in order to avoid contamination from the S-wave signal. For consistency, the same window size was used for the S-wave data. Trials with different window sizes did not significantly change the spectrum and had no effect on the overall conclusions. Although, window sizes that overlapped P- and S-waves yielded results that were noticeably different. It should be noted that the difficulty in determining the exact time of the arrival of the S-waves made the beginning of the window, and the resulting velocity spectrum, less reliable than that for the P-waves. Therefore, the results for the

source parameters and the implications of trends rely more confidently on the P-wave data. The Fourier transform used 128 frequencies up to a maximum of 500 Hz. Trials with lower cutoff frequencies, or those that employed low-pass filters, did not substantially change the results or affect the conclusions. The response of the seismometer, using parameters described in the previous chapter, was divided out from the spectrum. The effect of the response had a quantitative but not qualitative effect. In the current study, I used the Boatwright omega-square model to fit the velocity spectrum, with γ=n=2 (Eq.1). A sample fit, using the M3.4 event, is shown in figure 34. The travel times and the hypocentral distances were from the double-difference calculation. The exponential factor was of no real consequence since the best-fit values of Q were so large (~10,000). Nevertheless, the model was fitted with the full Boatwright expression. A standard inverse algorithm was used to fit the velocity spectrum with the parameters Ω_o, f_c, and Q as defined above.

Two data sets were analyzed in detail. The first was the full set of events which were linked by the cross-correlation coefficient. These ~3000 events were used to examine the question of scaling over a large range of parameters. The second set was more selective and was comprised of a subset of the large cluster, consisting of those events which were directly correlated to the M3.4 event. There were only 15 events in this cluster; a substantial difference from the original one. While the seismic moments for these events spanned over 4 orders of magnitude of the moment, they were constrained by their similarity. The large data set was more stable, since it was less susceptible to changes in the included events. No single events whether outliers, which

may have been included through the cross-correlation selection but were not really similar, or the M3.4 event, had any significant weight in the determination of the parameters. The study of the large data set was really an examination of the smaller magnitude events since the few large events carried very little weight. The M3.4 cluster, on the other hand, was more sensitive to individual events because of the smaller size of the data set. The M3.4 event played a more significant role, and for that reason, this data was better at describing the trends through a larger range of magnitudes. The results of the analysis of these data sets are given below.

3.4.3 Results

The events that were analyzed in the M3.4 cluster were the cluster of events which had a cross-correlation with the M3.4 of greater than 0.80. The first item to note is the range of the source dimension. Radii of less than 10 meters for small quakes were found, contrary to the previously held assumption that geometrical effects, such as the width of the fault zone would prevent source dimensions from being much less than 100 meters [Guo *et al*., 1992; Archuleta *et al.*, 1982]. These smaller source dimensions are consistent with numerous recent analyses and are crucial if scaling is to be valid. If the radii have a lower bound, then the stress drop will not be constant at lower seismic moments. The source radius for the M3.4 event was ~100m in good agreements with estimated fracture zone sizes of comparably-sized quakes. (see for example, Ambercrombie, 1995).

One of the main questions is whether the stress drop is constant, independent of the seismic moment. For the M3.4 cluster, for over 4 orders of magnitude of the seismic moment, the stress drop shows no trend (see figure 35). This independence is consistent with the moment's dependence on the source radius. Since the stress drop is proportional to the moment divided by the source-radius cubed (Eq.4), a constant stress drop would be given by a moment which had an r^3-dependence. When the moment, determined from the P-wave signal, is plotted versus the source radius on a log-log plot (see figure 36), the slope gives the power of the radius to be ~3.03±0.33, in close agreement with the expected value of 3. These results are supportive of source scaling for events of magnitude much less than 3. Since this works for a moment roughly 4 orders of magnitude less then the M3.4 event, the scaling appears to be valid at magnitudes less than M0. It should be noted that the slope is sensitive to the events which are included. The elimination of several events can change the fitted slope by ±0.5, so the goodness of the fit should not be taken too seriously.

A final and perhaps the most significant comparison is the radiated energy versus seismic moment. Since the apparent stress is proportional to the ratio of the radiated energy to the seismic moment, scaling would demand that the apparent stress be constant. Assuming a constant apparent stress, a best fit of the data (a linear least squares fit of the radiated energy to seismic moment) yields an apparent stress of 0.15 MPa. However, for the P-wave signal, a least squares fit using this model suggests that $E_R \sim M^{1.36}$, so that the apparent stress increases with increasing moment (figure 37). This result is contrary to the expected results if the source parameters scaled. While the overall fit is not consistent

with constant apparent stress, those events with larger moment seem to lie along a constant apparent stress.

The results for the analysis of the S-wave signal differ qualitatively from that of the P-wave signal. While some of the source dimensions fall below 10 meters, the radius of the M3.4 event is only ~40 meters, roughly half that found for the P-wave signal. This variation is not unreasonable compared with the values found in other studies. Abercrombie (1995) finds discrepancies of factors of two or greater in the source dimension between S- and P-wave analysis for individual quakes. I attribute this difference to the uncertainty in the S-wave arrival time, with the resulting uncertainty in the time window creating error in the velocity spectrum.

A plot of the stress drop versus seismic moment shows a definite trend of increasing stress drop with moment. For the S-waves, a least squares fitting of the stress drop versus seismic moment shows a slope which is more than a factor of 80 greater than was seen for the P-wave signal (figure 38). This trend is more readily seen in the fitting of the seismic moment to the source dimension. As determined by the S-wave signal, on a log-log plot of seismic moment versus source dimension, yields a slope of 3.37 (see figure 39). This is consistent with the result for the P-wave because the uncertainty with so few events is ±0.3. The magnitude of the slope, with the events that are included, suggests that scaling is valid in this model.

The analysis of the radiated energy versus seismic moment for the S-wave is similar to that of the P-wave, except the divergence from the scaling result is more pronounced (figure 40). For the S-wave, $E_R \sim M^{1.46}$. Again, this indicates that the

apparent stress increases with seismic moment. An assumption of a constant apparent stress gives a best fit value of 1.8 MPa, roughly an order of magnitude greater than the value found for the P-waves. In comparisons made by Abercrombie (1995), the ratio of E_S to E_P was found to be between 9.44 (without attenuation) and 14.31 (with attenuation). In the present case the ratio $E_S/E_P=7.41$.

While the M3.4 cluster seems to contradict scaling, it is not definitive because of the small sample size. The addition or removal of a few events can have significant impact on the statistics. But the results do suggest that small quakes have a strong similarity with larger quakes even if they are not exactly the same.

The main cluster emphasizes the smaller moment quakes because their increased percentage of the total number of events. Since the smaller quakes are the ones that are most controversial when it comes to scaling, this should be a more severe test of the scaling hypothesis.

When the stress drop is plotted against the seismic moment, there is a slight trend of increasing stress drop (figure 41). The slope is about eleven times larger than it was for the P-wave analysis in the M3.4 cluster. This dependence is still very small and by itself is not indicative of a breakdown in scaling. A different measure of the dependence of the stress drop on the seismic moment is the power dependence of the moment on the source dimension. This is displayed in figure 42. For the P-wave analysis, a substantial number of events have source radii less than 10 meters. Clearly, there is no geometrical limit to the source radius that is on the order of 100 meters. The fitted slope of 2.46±0.06

represents the weighting of the smaller quakes. The M3.4 event seems to align itself with a slight larger slope (figure 42).

This is not the case for the radiated energy in the P-wave analysis. The plot of radiated energy versus seismic moment differs significantly from the scaled model (figure 43). The nearly linear plot of data is significantly different from the expected values. The radiated energy, $E_R \sim M^{1.74}$, rather than being proportional to M. The apparent stress increases with increasing moment rather than being constant. It may be worth noting that the larger events do seem to track along the constant τ_A=0.2MPa, suggesting that perhaps scaling is valid for events of moment greater than approximately 1.

The S-wave analysis is very similar to the P-wave analysis for the full cluster. The stress drop for the S-wave has a greater dependence on the moment than for the P-wave. The fitted slope is 1.3×10^{-5} MPa/Nm, which is significant even for moments of 10^{10} Nm (figure 44). This breakdown in scaling is not as evident in the log plot of M vs r, where the fitted slope is 2.74±0.08 (figure 45) and the superposition of lines of constant stress drop seem to the eye consistent with the data. The difference between these plots comes from the dominance of the smaller moment events in figure 44, while the trend in figure 45 is dominated by the larger moment events. That is, if the larger moment events are eliminated from all of the graphs, only figure 45 will see a significant impact on the statistics.

The plot of radiated energy versus seismic moment for the S-wave data is similar to that of the P-wave (figure 46). In this case $E_R \sim M^{1.59}$, compared to a power of 1.74 for

the P-waves. The scaling result of $E_R \sim M$ is violated for both phases, so the apparent stress increases with increasing seismic moment rather than being constant. Again it should be pointed out that for large moment events constant apparent stress appears valid and is about an order of magnitude larger for the S-wave than the P-wave, 2.0MPa versus 0.2MPa. Similarly, the radiated energy from the S-wave portion is 10.0 times the radiated energy from the P-wave portion, which is consistent with previous studies.

3.4.4 Discussion

The question of whether source parameters scale with quake size is a continuing issue. The uncertainty of the calculations, coupled with the different data sets and analysis techniques used by investigators, keep the issue from being resolved. In this study I have compared two clusters, one a subset of the other, to determine the impact of quake magnitude and quake similarity on source parameter scaling. It appears from the results that scaling is more closely obeyed for a cluster of quakes with higher similarity which at the same time gives stronger weighting to larger quakes. Even for the M3.4 cluster scaling breaks down; the radiated energy is not proportional to the seismic moment over the range of events. Because of the ability to determine the P-wave arrival time with more accuracy than the S-wave arrival time, it is suspected that the resulting P-wave analysis should be more reliable. While the P-wave analysis shows closer agreement with scaling, it breaks down for smaller events. The strong correlation of radiated energy versus seismic moment for the smaller events, while not a direct proportionality, needs further examination.

The question posed by the preceding analysis is whether the apparent breakdown in scaling is the result of size effects, larger events being different than smaller events, or whether it is the result of comparing events which are dissimilar in terms of their cross-correlation. To address this question, I analyzed several different clusters. These clusters were formed by selecting a "seed" event and determining those events that were similar to the seed by having cross-correlation coefficients ≥0.85, 0.90, and 0.95. The source parameters for the events in these clusters were then determined and the scaling relations examined. The results were essentially the same for all clusters, regardless of whether the seed event had a large or small seismic moment. The radiated energy, $E_R \sim M_O^{\alpha}$, was consistent with $1.8 > \alpha > 1.6$. The noticeable trend was that as the cross-correlation coefficient increased, the value for α decreased to the lower end of the range. In all cases, the larger events in the clusters seemed to follow a different trend line, one which more closely followed scaling. It should be noted that as the cross-correlation increased the number of events in the cluster decreased and the uncertainty in the least-squares fit of the points increased. For no cluster were the results consistent with the scaling hypothesis. Furthermore, the M3.4 cluster had the smallest number of events. A typical cluster corresponding to the seed events that were examined contained >200 events for a coefficient of 0.85, while the M3.4 cluster had on the order of 10. These results indicate that the larger events were different from the smaller events, not merely scaled up. The source parameters did not scale as hypothesized. Furthermore, it is reasonable to suggest that the M3.4 event was significantly different from almost all of the other events and had a structurally different origin.

The trend of increasing energy with increasing moment is seen in several studies (for example: Abercrombie, 1995; Kanamori et al, 1993; Mayeda and Walter, 1996; Ide etal, 2003). A study by Wu (2001) compared the NEIC broadband radiated energy catalog and the Harvard CMT catalog and found that the ratio of E_R/M_o depended on the focal mechanism. For North America, where strike slip events predominate, E_R/M_o $\sim M_o^{0.36}$, while for Japan, where thrust mechanisms predominate, $E_R/M_o=M_o^{-0.10}$. Kanamori and Heaton (2000) also found increasing energy with seismic moment in North American small to moderate quakes. It has been suggested by Abercrombie [1995] and partially verified by Ide et al [2003] that the size effects could be attributed to the limited recording bandwidth or inappropriate correction for path effects in terms of attenuation.

That the decrease in the radiated energy for events with smaller seismic moments could be the result of the limited bandwidth (see, for example Ide *et al*, 2003), can be explained as follows. Because the sample rate for the sensors was 1000 per second, the Fourier transform is limited to 500 Hz. Smaller events generally have larger corner frequencies and therefore a higher proportion of their energy will be in the tail region above 500 Hz. If a sufficient amount of energy was disproportionally in the tail region for the smaller events, then this neglected energy could account for the resulting inconsistency with scaling, a non-constant apparent stress. To test to see if the limited bandwidth was responsible for the energy falloff, I used an analytic extrapolation of the Boatwright formula (Eq.1) to determine the fraction of energy beyond the 500 Hz cutoff. The radiated energy is proportional to the integral of the square of the velocity spectrum over frequency, $\int\Omega^2 df$. After fitting the waveform, as described above, I numerically

computed the integral using the Boatwright formula to 500Hz. I then used the asymptotic form of the Boatwright, $\Omega \sim f\Omega_o(f_c/f)^2$, to analytically calculate the energy in the tail, $E_R \sim \Omega_o f_c^4/500$. This factor was then used to correct for the fraction of the energy that was in the tail above 500Hz. As expected, the effect of the correction was to increase the radiated energy for the smaller events but the size of the effect was negligible. The largest correction factor was approximately 2, meaning that half of the radiated energy was in the excluded tail region. But since the smaller events were nearly a factor of 1000 lower in radiated energy than needed to be consistent with scaling, this is a minor effect. The slope of $\log(E_R)$ vs $\log(M_o)$ only decreased from 1.74 to 1.7 for the P-wave contribution; not enough to change the conclusion that the apparent stress is not constant. It is still possible that the higher frequency regime is responsible for the inconsistency, if for example the Boatwright model is not representative of high frequencies. The use of a higher sample rates could help to resolve the issue.

There is always the possibility that the source parameter data is being compromised by other effects. The sensors, site effects, and path effects could contaminate the data in systematic ways that might skew the results. Volumetric changes, which may be prevalent in hydro-fractured stimulated events, as opposed to pure shear events might have an effect on the measured energy. It is also possible that the circular-rupture model is inappropriate under certain conditions. The scaling hypothesis remains an interesting question for further inquiry.

Several other trends and results are consistent with previous studies. The radiated energy from the S-wave portion is about an order of magnitude greater than that from the

P-wave portion. The range of source dimension, the radius assuming a circular pattern, ranges from a few meters to ~100 meters, consistent with the results for similarly sized quakes in other studies. The stress drop, apparent stress, and seismic moment are also in reasonable agreement with the results of other studies. The corner frequencies for the P-wave section average approximately 1.2 times larger than those for the S-wave (full cluster analysis), comparing favorably with Abercrombie's (1995) value of 1.3. Even with this general agreement regarding values, there remain disagreements regarding conclusions.

3.5 Conclusions

1) Scaling is not valid for the Basel hydro-fracture stimulated events over the full range of moments.
2) Scaling is approximately obeyed for the larger events.
3) There is a breakdown in scaling for the smaller events. Seismic moment and radiated energy have a strong correlation for small events, which is different from that of larger events.
4) It is reasonable to suggest that the M3.4 event was significantly different from almost all of the other events and had a structurally different origin.

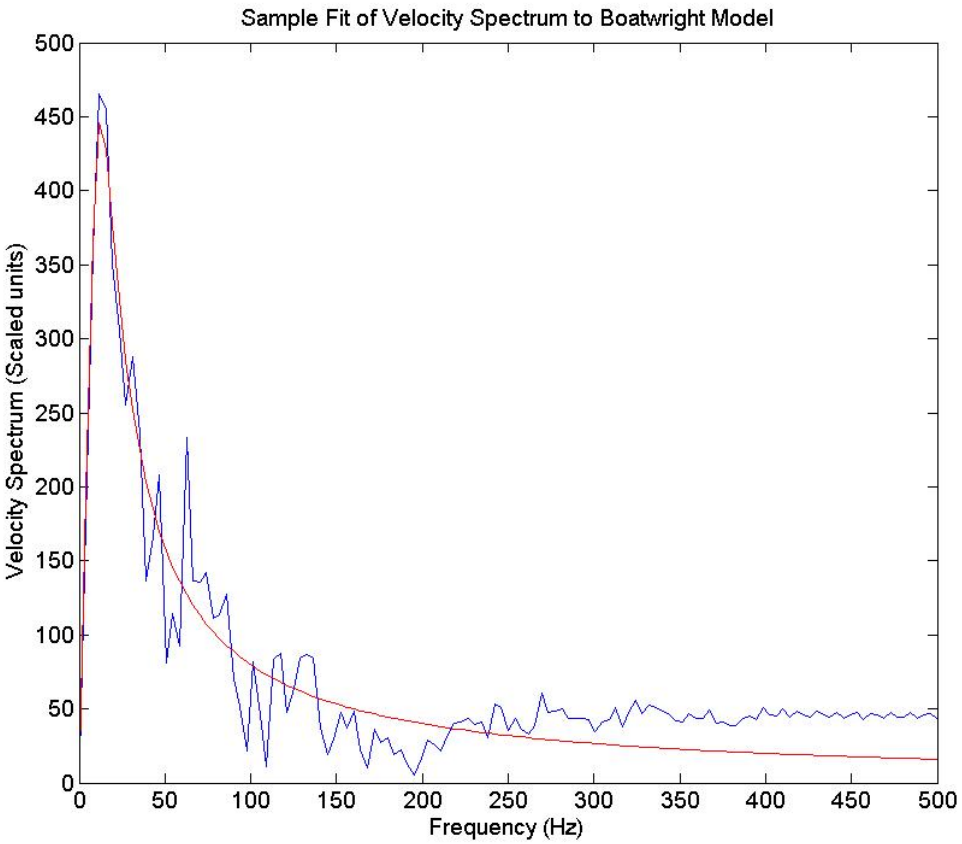

Figure 34: Sample fit of the velocity spectrum to the Boatwright model.
Fit of velocity spectrum from M3.4 event to the Boatwright omega-square model. Red curve is the fit.

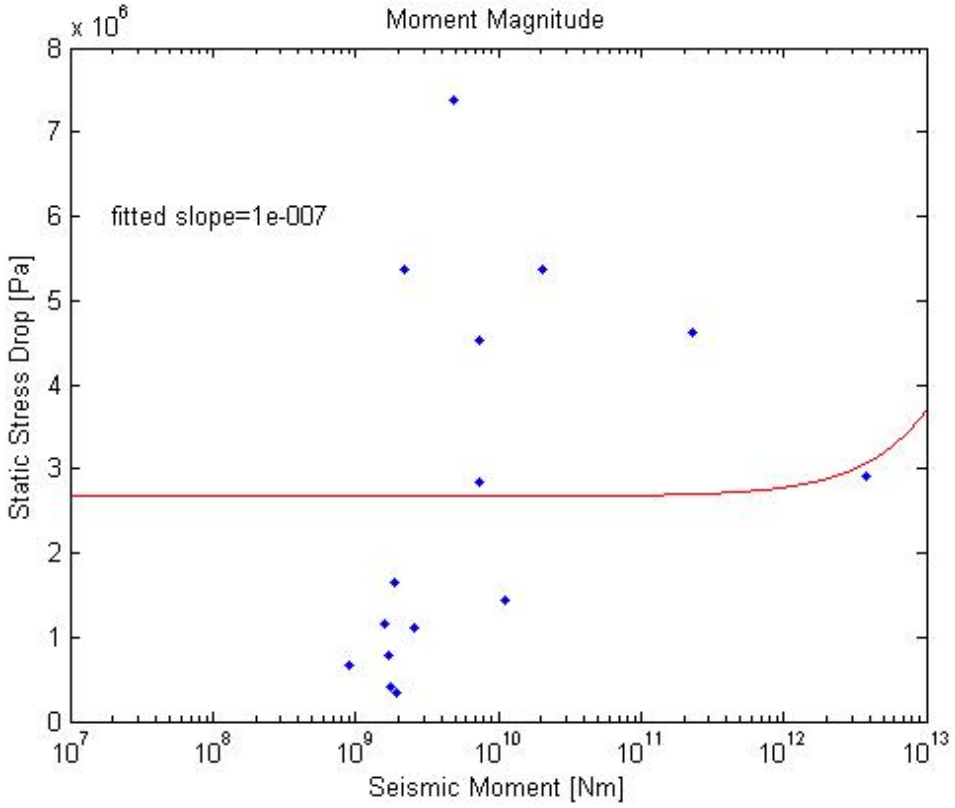

Figure 35: Static stress drop vs moment for th P-wave in the M3.4 cluster
The red curve is the least squares fit to a linear expression τ=a*M+b (the apparent curvature is a result of the semi-log plot). There is negligible dependence of stress drop on seismic moment.

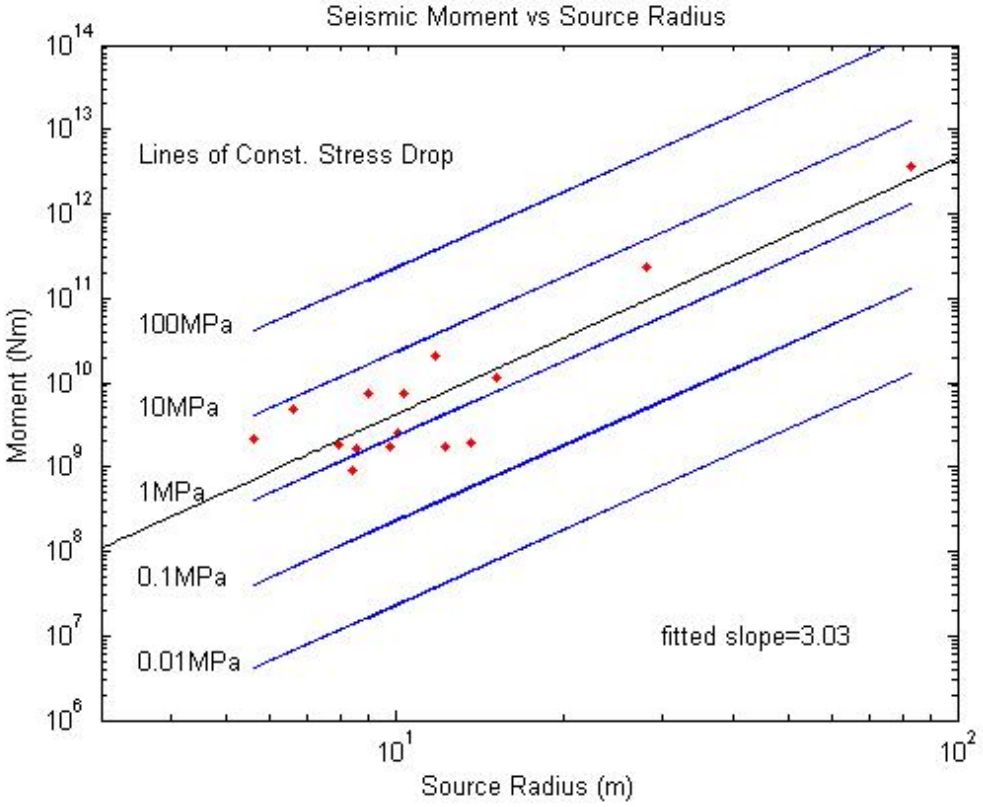

Figure 36: Seismic moment vs source radius for the P-wave in the M3.4 cluster. Lines of constant stress drop are shown. The fitted slope of 3.03 is consistent with $M \sim r^3$, implying a nearly constant stress drop.

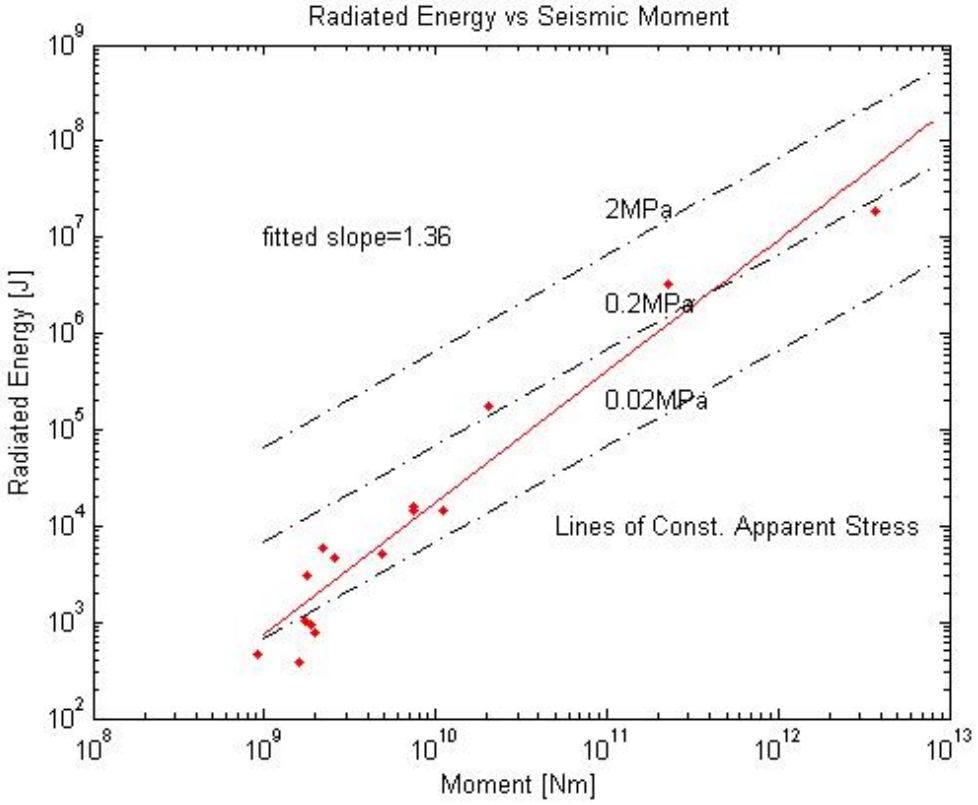

Figure 37: Radiated energy vs seismic moment for the P-wave in the M3.4 cluster. Lines of constant apparent stress are given by the -.-. curves. The red curve is the least squares fit of $\log(E_R)=a*\log(M)+b$. While the overall fit is not consistent with constant apparent stress, those events with larger moment seem to lie along a constant apparent stress.

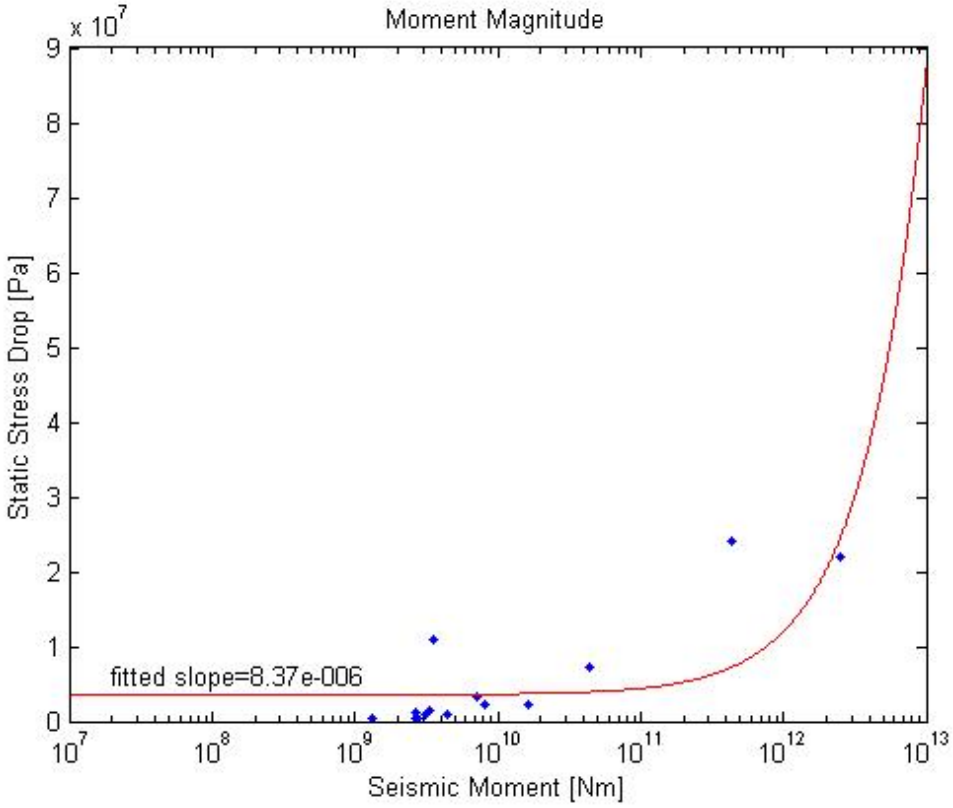

Figure 38: Static stress drop vs seismic moment for the S-wave in the M3.4 cluster. The red curve is the least squares fit to a linear expression τ=a*M+b (the apparent curvature is a result of the semi-log plot). The dependence of stress drop on seismic moment for the S-wave is more than 80 times greater than for the P-wave.

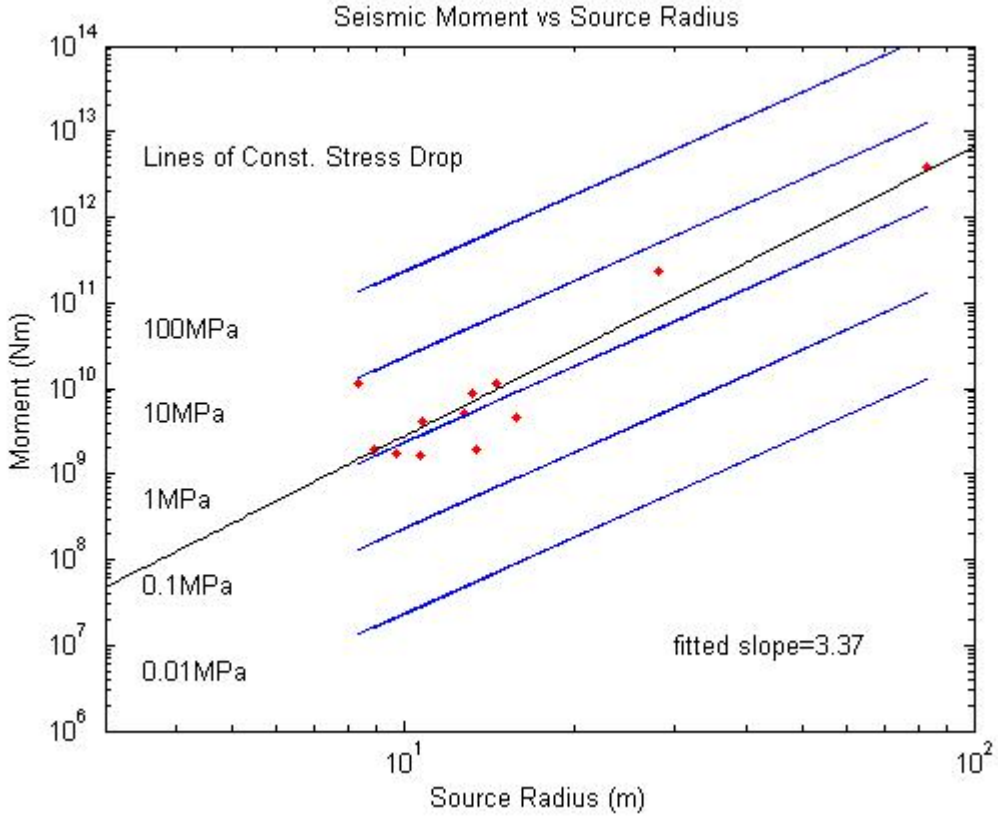

Figure 39: Seismic moment vs source radius for the S-wave in the M3.4 cluster Lines of constant stress drop are shown. The fitted slope of 3.37 indicates that $M \sim r^{3.37}$, implying a stress drop that increases with seismic moment.

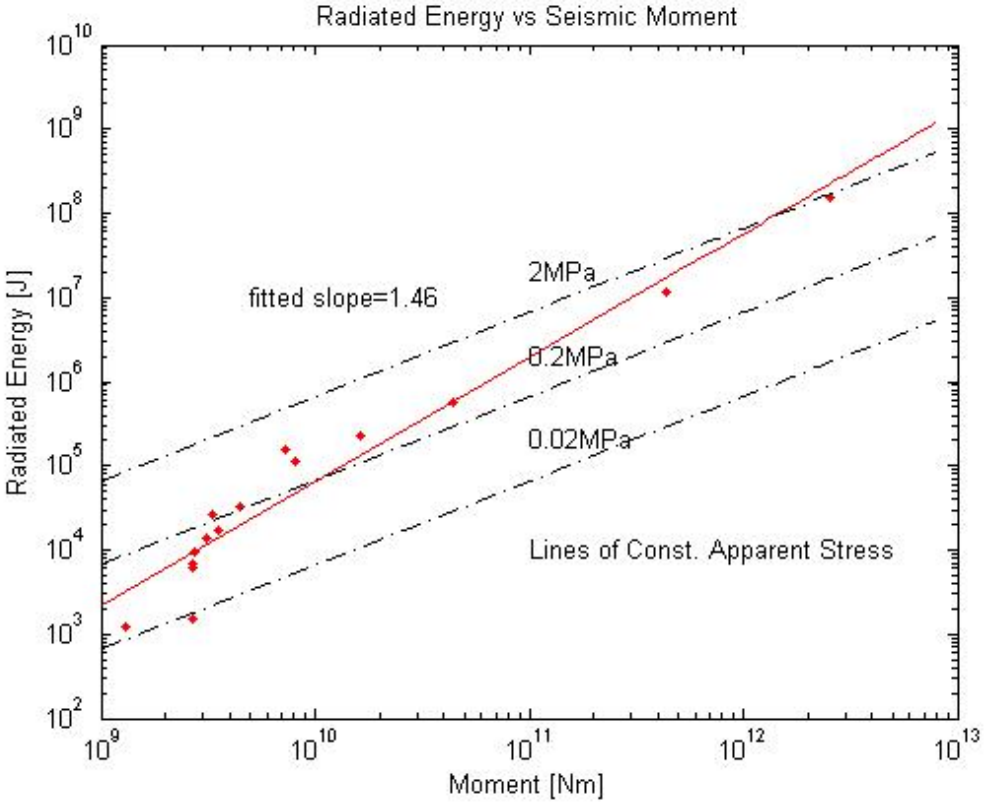

Figure 40: Radiated energy vs seismic moment for the S-wave in the M3.4 cluster
Lines of constant apparent stress are given by the -.-. curves. The red curve is the least squares fit of $\log(E_R)=a*\log(M)+b$. The overall fit is not consistent with constant apparent stress, even for those events with larger moment.

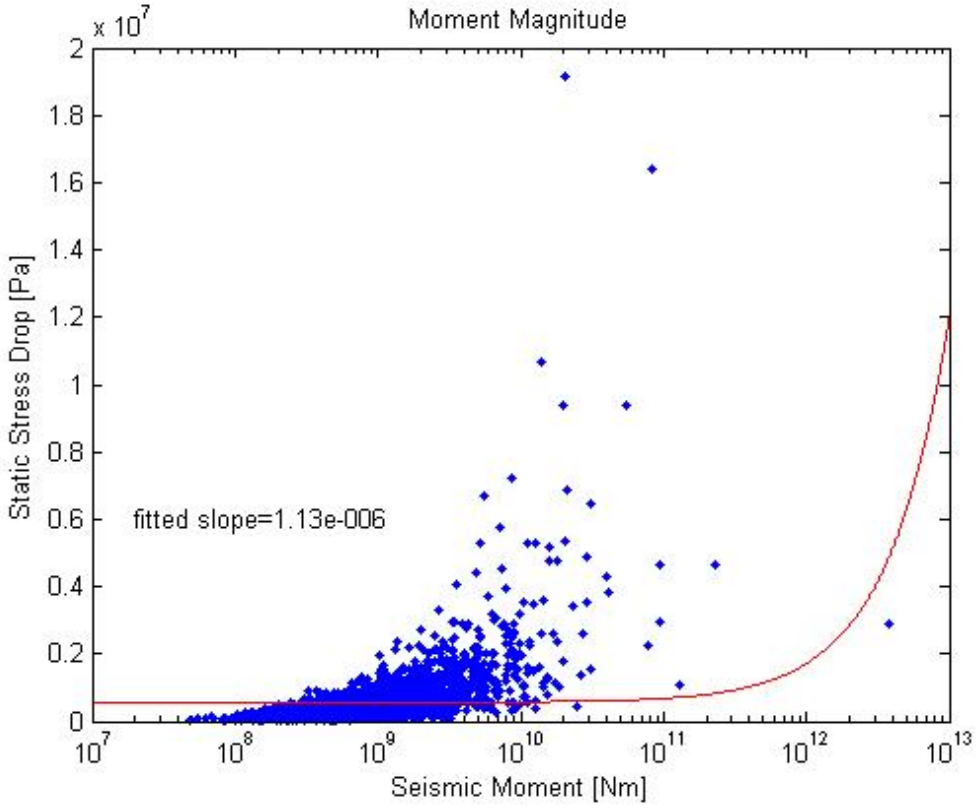

Figure 41: Static stress drop vs seismic moment for the P-wave in the full cluster. The red curve is the least squares fit to a linear expression τ=a*M+b (the apparent curvature is a result of the semi-log plot). There is minimal dependence of stress drop on seismic moment.

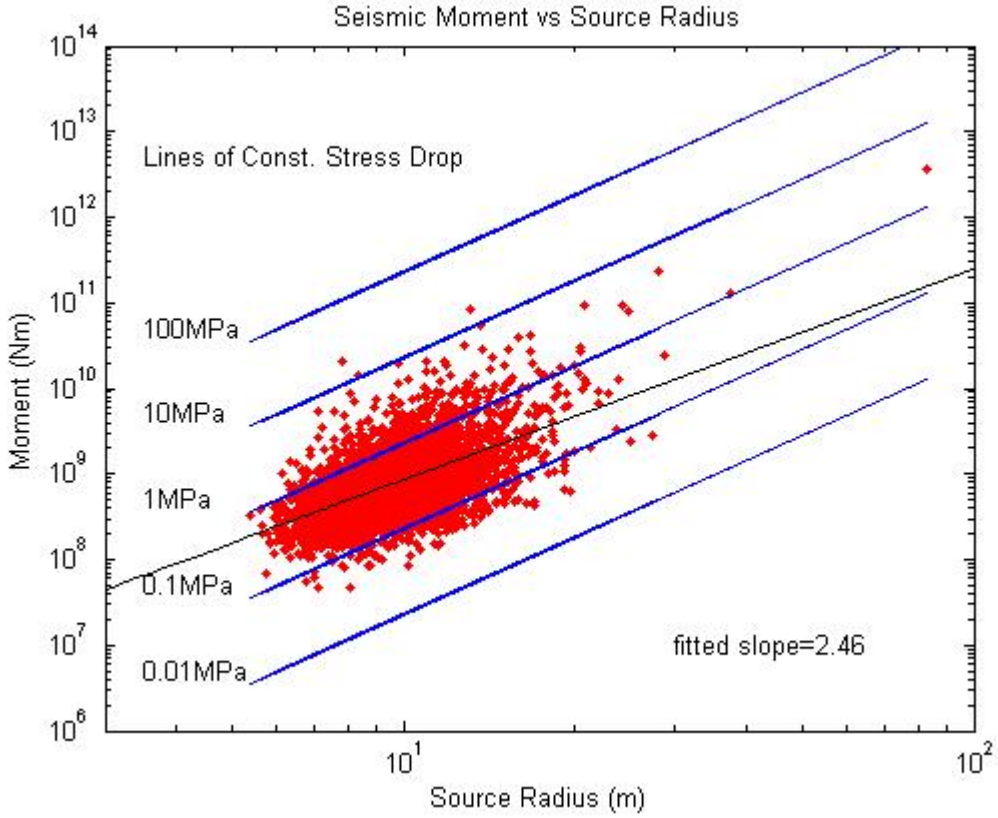

Figure 42: Seismic moment vs source radius for the P-wave in the full cluster. Lines of constant stress drop are shown. The fitted slope of 2.46±0.06 indicates is not consistent with $M \sim r^3$, implying a stress drop that decreases with increasing seismic moment.

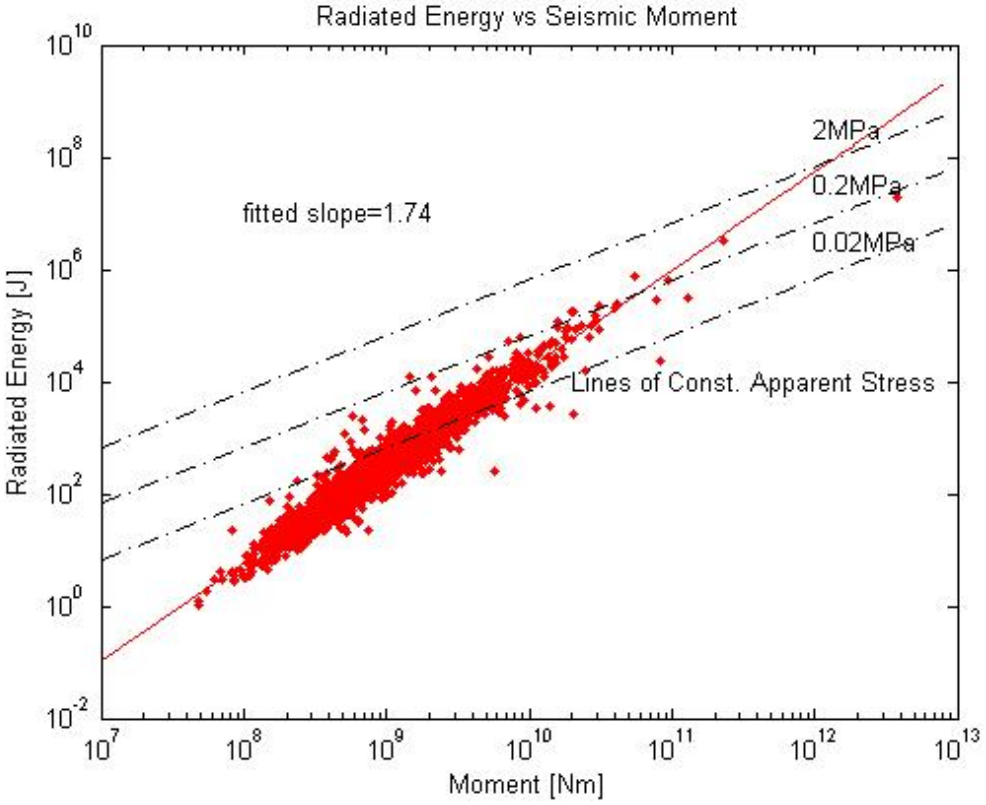

Figure 43: Radiated energy vs seismic moment for the P-wave in the full cluster. Lines of constant apparent stress are given by the -.-. curves. The red curve is the least squares fit of $\log(E_R)=a*\log(M)+b$, with a=1.74. While the overall fit is not consistent with constant apparent stress, those events with larger moment seem to lie along a constant apparent stress of τ_A=0.2 MPa.

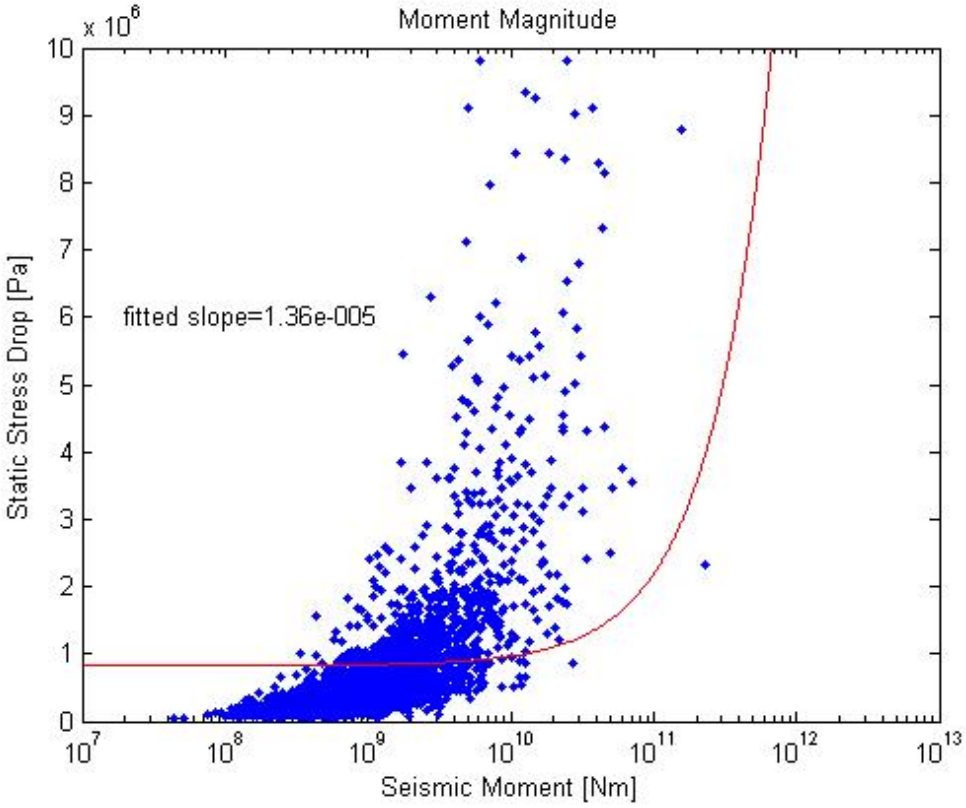

Figure 44: Static stress drop vs seismic moment for the S-wave in the full cluster. The red curve is the least squares fit to a linear expression τ=a*M+b (the apparent curvature is a result of the semi-log plot). There is significant dependence of stress drop on seismic moment.

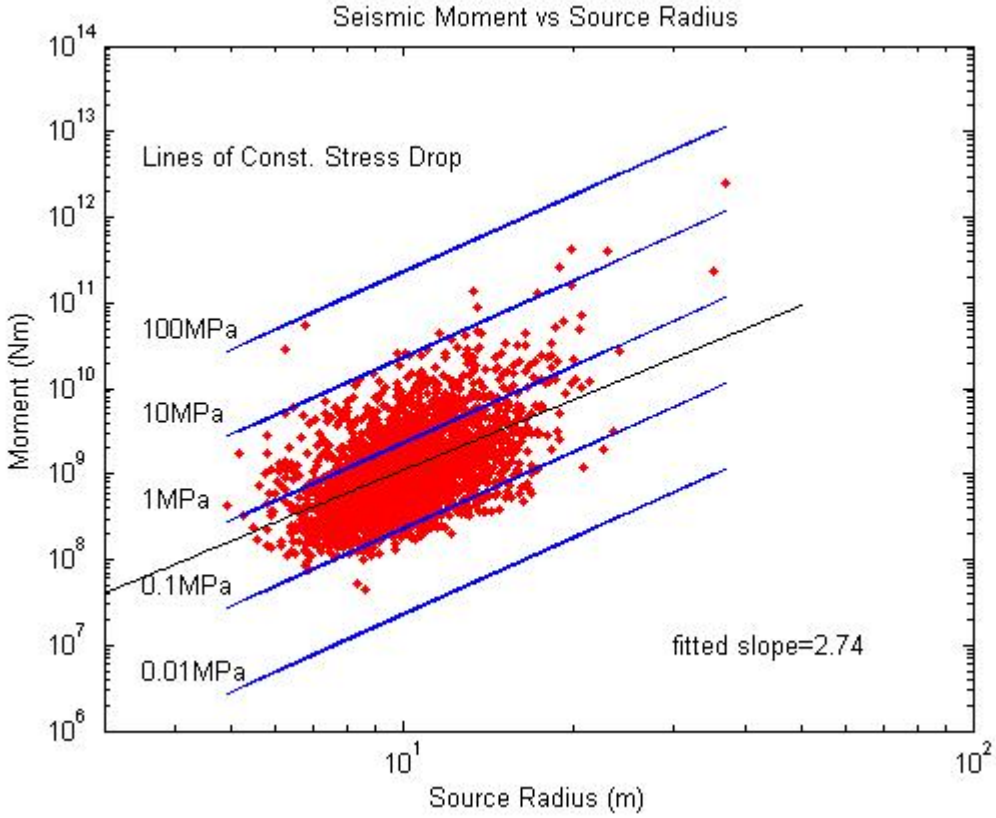

Figure 45: Seismic moment vs source radius for the S-wave in the full cluster Lines of constant stress drop are shown. The fitted slope of 2.74±0.08 indicates is not consistent with $M \sim r^3$, implying a stress drop that decreases with increasing seismic moment.

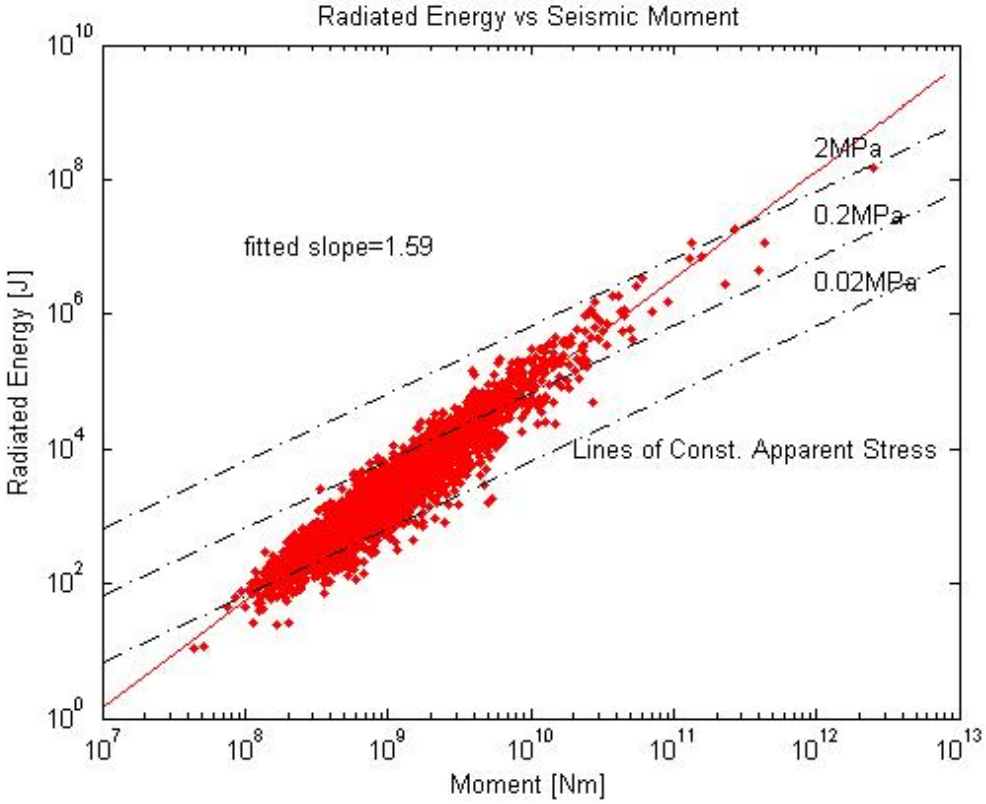

Figure 46: Radiated energy vs seismic moment for the S-wave in the full cluster. Lines of constant apparent stress are given by the -.-. curves. The red curve is the least squares fit of $\log(E_R)=a*\log(M)+b$, with a=1.59. While the overall fit is not consistent with constant apparent stress, those events with larger moment seem to lie along a constant apparent stress of $\tau_A \sim 2.0$ MPa.

Appendix 1: Seismic Study of the Krafla Geothermal Field

A1.1 Project Overview

Iceland is an island country which straddles the mid-Atlantic spreading ridge, so that part of the island is on the North American Plate and part of it is on the Eurasian plate. Iceland is literally being torn apart as the plates separate. The separation is especially evident around Krafla, the site of this study, where displacements caused by rifting totaled almost seven meters between 1975 and 1984. New fissures appear and existing cracks continually widen, while magma occasionally breaks through during volcanic activity. Microearthquakes are commonplace. Therefore, the geography of this region is constantly changing.

A hotspot is also associated with Iceland giving the country access to a large amount of potential geothermal energy from the large magma reservoir below. The heat below the surface is evident by the presence of naturally occurring steam vents. Geothermal power actually supports 87% of the Icelandic population's heating needs and 17% of its electricity needs. This power is generated from geothermal power stations, which pump relatively cool water into the hotter subterranean regions using injection wells. The water returns as steam, which drives the power stations' turbines and generates electrical power. The water injection controls the amount of steam produced due to the fact it is the dominant source of water flux into the magma source. This water injection however is thought to control another phenomenon, earthquakes.

There have been numerous studies that have tried to determine the connection between water injection (or other fluid injection, such as oil) and earthquake swarms (see for example Schulte-Theis Hartwig (1995), Brandsdóttir et al (1994), Genmo et al (1995), Healy et al (1968), and Ohtake (1974)). One such study was done in the Nojima fault zone in Japan by Tadokoro et al (2001). This fault zone had a very large earthquake in 1995, and they began injecting water into the zone in 1997 for the "healing process". Before injecting water they set up a network of seismometers throughout the area. Three unique aspects of the fault zone were observed by doing this: 1) The water-induced earthquakes were in the same zones as normal seismicity which means there is an inhomogeneity in the crust; 2) There was successive rupturing on the fault probably due to water migration in the weak fault area; 3) Low b-values of 0.6, much lower than normal earthquakes in the area, were recorded. This helps support the idea that water reduces the effective stress so that fault slip is easier, causing earthquakes.

Another prominent study took place much closer to Krafla, in the Svartsengi geothermal field in Iceland. The conclusion of Davis and Frolich (1993) was that the injection pressure into Svartsengi was insufficient to cause induced seismicity. There are now permanent seismic stations operating to monitor the local microseisms.

These studies, as well as many of the others, are based on the theories involving water injection and its ability to reduce the normal stress between plates. The initial hypothesis developed by Hubbert and Rubey (1959), suggested that increasing fluid pressure in pores decreases friction allowing plate movement. When the fluid pressure in a fault zone approaches lithostatic pressure the normal stress across the fault becomes

small (Healy et al, 1968). In other words, when the magnitude of the fluid pressure approaches the weight of the rock, the fluid can give an upward force that can support the weight of the rock, and act as a lubricant between both surfaces. This would create a situation where the fault would slip more easily.

As part of a joint project between the University of North Carolina, Duke University, and the Krafla Geothermal Power Station, an array of twenty Geospace GS-1 sensors along with an array of twenty PASSCAL L-28 4.5-Hz sensors were placed in a 25km^2 area within the Krafla power station grounds. The positions of the seismometers were based on the proximity to the power plant's injection well, accessibility, and isolation from noise. The seismic network set up in the Krafla geothermal power plant area was done for the purpose of examining the injection wells influence on the micro-earthquakes in the area, and the reaction of the highly faulted and cracked surface to the fluid pressure induced by the geothermal power plant.

A1.2 Krafla Geothermal Power Plant

The Krafla Power Station is located in the northern part of Iceland directly on the rifting zone associated with the Mid-Atlantic Ridge spreading center, and over the zone that is associated with the hotspot. Krafla is an area with a large amount of volcanism because it sits within a caldera. It has seen 18 violent eruptions during the recent past, the latest of which almost canceled the power station construction. The spreading center causes the land to be heavily faulted and fissured; the continually shifting faulting causes frequent microseisms. The Krafla Power Station is Landsvirkjun's main geothermal

power source. There are 34 wells, 15 of which are high-pressure wells, 5 are low-pressure wells, and 14 wells which are unutilized or unserviceable. On average, 15-17 wells are in use at any one time, one of which is the injection well.

Geothermal power is created from pumping cold water into the injection well, which extends into the hot magma source. This creates high-pressure steam which accelerates up through the other wells and enters the power station. This steam is used to spin the turbines producing the electrical power (the station operates with an installed capacity of 60 Megawatts (MW)). The used steam is then cooled in the cooling tower and recycled into the ground. The process produces completely clean power making it an environment-friendly energy.

A1.3 Field Instrumentation

The Geospace GS-1 is a 3-component, 24-bit, 4-channel, digital grade seismometer with standard up-right-forward movement detection, designed for seismic exploration in a variety of terrains (Figure 47). It is designed with a natural frequency of 1 Hertz (Hz), well suited for optimal response to microseisms where the driving frequency is expected to be low. The twenty Geospace GS-1 seismometers used for this study proved to be portable over rough terrain, durable, easy to maintain, and accurate.

The Geospace seismometers functioned well over a variety of conditions. The temperature ranged from –10C to 25C with no discernable effect on the seismometers. The seismometers were easy to maintain with lightweight alkaline batteries lasting between 44-48 hours. With lithium batteries the seismometers could continue to run for

over a two week period. Lithium batteries, however, are considered a safety concern on airplanes with the heightened security, and could not be shipped in time for this experiment. The alkaline batteries were charged by parallel connection, with 10 batteries charged by one machine in 12 hours. Since the batteries had a full day to charge there was never a problem with semi-charged batteries in the field. The PCMCIA flash storage card memories of 2 Gigabytes (GB) were changed every 2 days, at the same time the batteries were changed, even though the flashcards had the ability to last up to 4-5 days while running at a sampling rate of 500 samples per second (2ms). Evidence of the seismometers' accuracy is found in the close correlation with data from multiple devices and the interpretation of the epicenter locations in terms of MT measurements. The specifications for the device are found in Table 1.

Figure 47: The GeoWatch recorder

The GeoWatch recorder (top) fully assembled with a three-component SeisMonitor (1 Hz, HS-1) unit (bottom) and leveling legs. Both components are sealed for weatherproof operations. The system is configured as an anti-theft device for remote earthquake recording.

Table 5: Geospace GS-1 Seismometer Specifications

Description	Specifications @25C	Tolerance±
Natural frequency (Fn)	1.0 Hz	10%
Coil resistance (DCR)	4550 Ω	5%
Tilt angle, measured from Horizontal	0.5°	
Intrinsic Voltage Sensitivity	9.7 V/in/sec, 3.8V/cm/sec	10%
Normalized Transduction Constant	0.143 √(DCR) V/cm/sec	10%
Open Circuit Damping	0.54	20%
Damping Constant	16,579	
Sample Rates (ms)	¼,½,1,2,4,8,16	
Preamplifier Gain (dB)	0 to 36 in 6dB increments	
Instantaneous Dynamic Range (dB)	127	
Gain Accuracy	Better than 0.2%	
Maximum Parsed Record Length	16 seconds in continuous record mode	
Operating Temperature	-40 to 100° C	
Moving mass (m)	700 grams	5%
Coil excursion (peak-to-peak)	>0.635cm	
Number of Channels	up to 4 channels	
Digitization	24-bit delta-sigma AD	
Anti-Alias Filter types	Linear or Minimum phase	
Frequency response	DC to 3200Hz@ ¼ ms sample rate	
Dynamic range	123dB at sample rate of 500/s	
Absolute time accuracy	<1 microsecond of UTC (with GPS)	
Sampling accuracy	better than 0.5 ppm	
External connections	Analog Seis input (4 channels) Battery charger or external battery RS232 serial port	
Dimensions (Outside Diameter)	7.62cm	
Height	16.4 cm	
Weight	1.960 Kg	

The 4550 Ω resistance gives a damping constant of approximately 0.54 of the critical damping , which occurs when the damping constant of the seismometer, $h = D/(2m\omega_o) = 1$ (Scherbaum,1996). Here D is the friction coefficient, ω_o is the natural angular frequency which equals $2\pi f_o$, and m is the moving mass. The damping is controlled by the total resistance of the circuit, coil plus shunt. With these parameters, the damping factor, $\varepsilon = h\omega_o = 3.393$. The frequency response function (the ratio of the amplitude of the moving mass to the moving ground) is given by

$$T = \frac{\omega^2}{\sqrt{\left(\omega_o{}^2 - \omega^2\right)^2 + 4h^2\omega^2\omega_o{}^2}} e^{i \arctan\left(\frac{-2h\omega_o\omega}{\omega_o{}^2 - \omega^2}\right)} \qquad (1)$$

At resonance ($\omega=\omega_o$), the response function $T(\omega_o) = 0.9259$. An electrodynamic system records ground velocity and translates it into a voltage. The magnitude of the response function is given by

$$|T| = G\frac{\omega^2}{\sqrt{(\omega_o{}^2 - \omega^2)^2 + 4h^2\omega^2\omega_o{}^2}} \qquad (2)$$

The constant G, the intrinsic sensitivity (also called the generator constant of the seismometer coil), has units (voltage/ ground velocity) and allows the conversion of the recorded output to the ground motion. The output voltage per inch per second (ground velocity) as a function of frequency is shown in Figure 48. As can be seen the most sensitive response is near the resonance frequency, and above that frequency the seismometer generates a voltage proportional to the ground velocity (the response is flat). For $\omega>5\omega_o$, $|T(\omega)| = G$, the constant response. From the graph, the value for G~9.7

volts/(inch/sec), which is the listed intrinsic sensitivity. This enables voltage readings to be converted to ground velocity.

The frequency response function is the Fourier transform of the time-dependent impulse response function. A related function is the transfer function T_s, which is the Laplace transform of the impulse response function. The transfer function gives the ratio of the Laplace transform of the mass excursion to the ground excursion, and can be found by substituting s=iω into the frequency response function.

$$T_s = -G\frac{s^2}{s^2 + 2h\omega_o s + \omega_o{}^2} \tag{3}$$

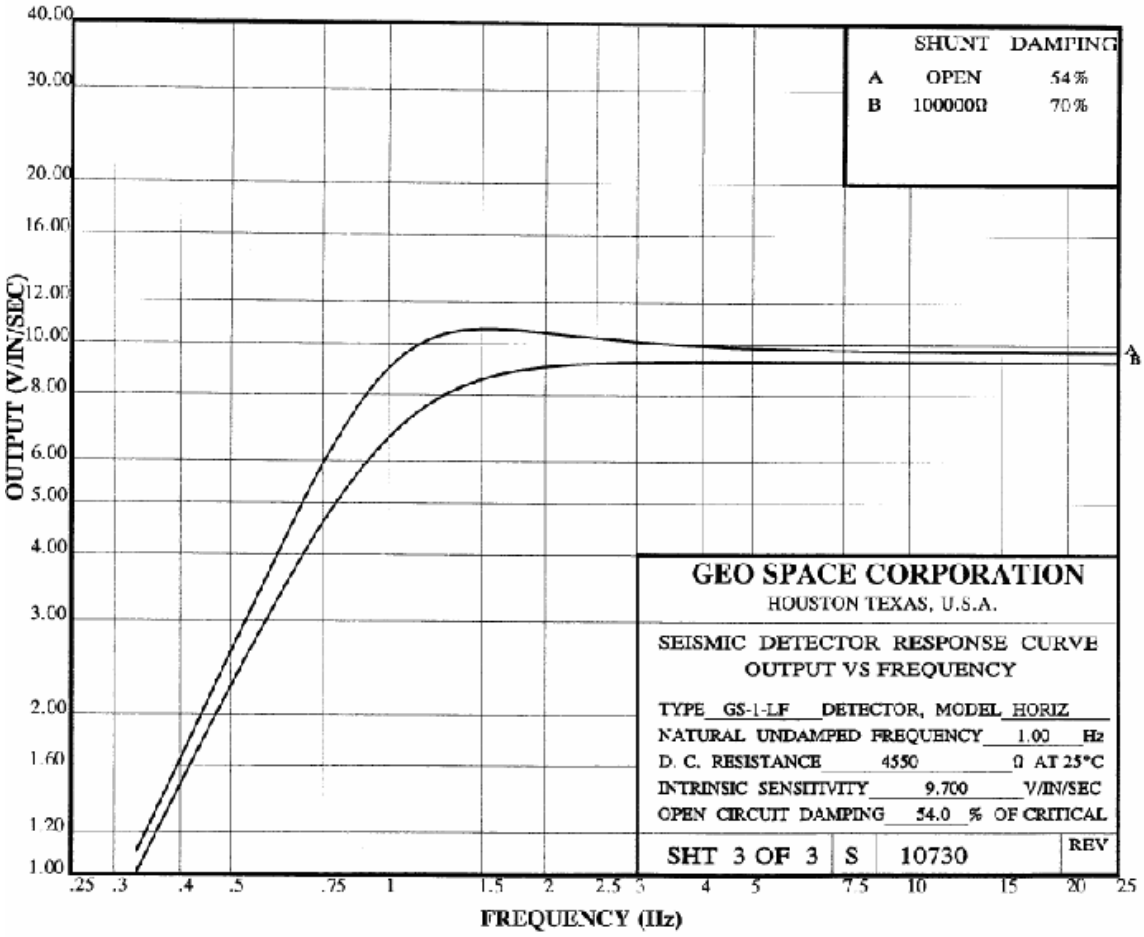

Figure 48: Seismic Detector Response Curve

The poles and zeros of the transfer function determine the response, and in the present case are given by,

$$s(\,pole\,) = -\left(h \pm i\sqrt{1-h^2}\right)\omega_o = -3.393 \pm 5.288\ i \qquad (4)$$

while there is a double zero at s=0.

A1.4 Instrumentation set-up and maintenance

The locations of the seismometers were determined with several features in mind. The first and most important requirement was that the network of stations be evenly distributed around the injection well, since it was anticipated that the majority of microseisms of interest would occur in the vicinity of this site. The rugged terrain demanded that the seismometers be lightweight and easy to set up. Transportation of the stations was convenient due to their compactness (only 2 major pieces). A group of four was capable of transporting eight stations by foot over several kilometers with backpacks. Setup in rough terrain wasn't too much of a factor either, although some problems were encountered as described below. The seismometers were easily placed at the top of hills and over stretches of lava fields. The Geospace seismometer's size and weight made them suitable for this project.

Additionally, it was necessary that the stations be well anchored to the ground for the best sensitivity (See Figures 49 and 50). Site selection was dependent on ground workability, because the seismometer had to be anchored by securing a 70cm auger. The auger is a metal screw which couples the seismometer acoustically to the ground and increases security. Some otherwise desirable locations with areas of lava flows or shallow zones of permafrost caused numerous problems when the auger could not be properly secured. There were other areas that had eroded dirt deposits that were deep enough for the auger, but the loose dirt impeded anchoring the seismometer. On average it took at least 2-3 setups of each seismometer, due to terrain variability, before a location was found where it could be solidly anchored.

Furthermore, protection from the elements was also a location influence. Since the seismometers stand 30cm above ground, wind and rain tend to vibrate the metal capsule, causing low-level noise to infiltrate the data. In order to combat this vibration, low lying areas or areas blocked by cliffs were ideal. This too caused some minor problems. In the lower lying areas the ground tended to be less workable because an impenetrable layer would come into play at a shallower depth. Moreover, the GPS would fail to connect if the seismometer was too close to a cliff face. Most of these weather problems result from the fact that the seismometer is above ground. There was also a high risk of temporary malfunctions if moisture entered the seismometers during battery or memory card exchanges at which time all the wires and equipment were directly exposed to the weather. On several occasions the seismometers had to be moved because of noise from vehicles, pumping stations, and foot traffic interfered with data collection. Table 2 lists the stations and their locations. More than 20 sites are shown because of the relocation of several stations during the project.

Figure 49: The anchoring assembly components

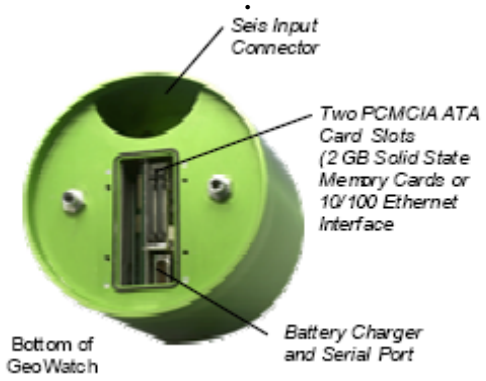

Figure 50: Electrical Connections

Table 6: Station Locations

	Latitude		Longitude	
Station id	degrees	minutes	degrees	minutes
G20	65	40.9961	16	42.7264
G21	65	41.6421	16	42.4167
G22	65	41.2836	16	45.5938
G23	65	40.9303	16	46.3333
G24	65	41.9273	16	44.0465
G25	65	41.6303	16	44.6075
G26	65	41.255	16	46.7408

G27	65	43.1852	16	45.6125
G28	65	43.2976	16	44.979
G29	65	42.7819	16	44.5219
G30	65	42.3988	16	45.1064
G31	65	41.875	16	45.4517
G32	65	41.608	16	46.6665
G33	65	42.3277	16	43.23
G34	65	42.1194	16	44.9905
G35	65	41.6179	16	48.1742
G36	65	42.9821	16	48.0155
G37	65	42.5637	16	47.2842
G38	65	42.2972	16	47.5448
G39	65	41.9749	16	47.8121
G40	65	41.973	16	47.9044
G41	65	42.1	16	43.7673
G42	65	42.3973	16	45.1524

When a potential spot was found, the auger was screwed in. This took a substantial effort since it had to be drilled quite deeply into the ground; the top of the auger had to be 15 cm below the surface because the J-bolt connecting it to the seismometer was about 15 cm long. The process of connecting the seismometer to the ground required two people. Once the auger was successfully anchored, a J-bolt was attached to the bottom of the seismometer and a wrench was connected to the top of the seismometer. The J-bolt was then attached to the auger. One person had the job of aligning the seismometer to the north (+15degrees) and trying to keep it level (using the level bubble), while keeping strain on the J-bolt so it would continue to be connected to the auger. The second person used the wrench to screw in the seismometer and pack dirt underneath, securing it to the ground. This process took the longest amount of time because it was the critical to obtaining calibrated data. If the seismometer was pointed in the wrong direction or was not level, the data would be altered in a random fashion.

Once secured to the ground the seismometer was locked down. This set-up gives a very good signal for an instrument that is above the ground. It also provides security for the instrument from being stolen or altered.

Once anchored, the battery is checked and connected, and a flash card is installed in the seismometer. The seismometer is closed and locked using the hex pin key. There is then a slight wait for the GPS to establish a connection. Depending on the location of the seismometer, the GPS varied in the time it took to connect. The lights on top of the seismometer were color-coded for the GPS connection (red =not acquiring or storing data, orange=no GPS ,clock not stable, green=acquiring and storing, yellow=warning low battery or memory). The following is a typical progression:

- Red & Orange Blink - No acquisition & No satellites
- Red & Orange - No acquisition & Satellites in view, No stable clock
- Red Blink & Green Blink - No storage yet & Acquisition started.
- Green - Acquiring data (wrote previous data)

Once the GPS connection was established, the setup was complete, and it was on to the next station.

A1.5 Data and Preliminary Results

The data from the Geospace GS-1 seismometers were used to determine the location of the epicenters through analysis of the P-wave and S-wave arrival times. A sample of the raw data is shown in Figure 51. The traces, corresponding to the two transverse directions of the S-wave and the longitudinal P-wave, are recorded on the tri-

axis system. Data from the twenty seismometers, gathered over the 14-day span, were inspected, and the signatures of likely events were handpicked. Events observed at more than four stations were evaluated and the epicenters determined. Approximately four micro-earthquakes were observed per day, with somewhat fewer occurring when the injection well was not operational. The results of this process are shown in Figures 52 and 53. In Figure 52 the locations of the epicenters and seismometer stations are displayed along with the injection well. Figure 53 shows a vertical cross-section along a line rotated 37.8 degrees counter-clockwise from due north. It is along this line that the earthquakes tend to occur (The x in the figure is the site of the injection well).

Several deductions can be made from this analysis. The clustering of the microseisms suggests a fault line or series of cracks lie along a northeast direction. Their location in the near vicinity of the injection well, along with the temporal correlation of the microseisms with the injection of water, are evidence supporting the causal relation between water injection and seismic activity. The depth of these epicenters at approximately 2500 meters is consistent with the MT data, which shows the border of high resistivity at this depth along the line. Not only is the depth correlated with the MT data, but the general curved shape (concave downward) is replicated in the MT data. This is indicative of the dome of hotter material at this depth.

To determine the density and polarization of cracks in the transmitting medium, a high frequency sampling rate of 500 samples /second was used to perform the frequency dependent SWS analysis. The differential time delay (the time difference between the fast and slow polarization modes) scaled by the distance traveled from an

epicenter to a station can be used to determine the density of cracks along the path. An equal-area projection showing the location of the epicenters and the differential time delay is shown in Figure 54 for station G28. The large circle is the shear-wave window of 36 degrees (= $\sin^{-1}$(Vp/Vs), the angle at which surface effects corrupt the waveform, Booth and Crampin,1985). The orientation of the fast polarization is an indicator of the orientation of the cracks. An equal-area projection of the polarization angle is shown in Figure 55 for station G28. To better visualize the polarization of the cracks, a set of rose diagrams (polar histograms) is shown in Figure 56 superimposed on a map of the seismometer sites.

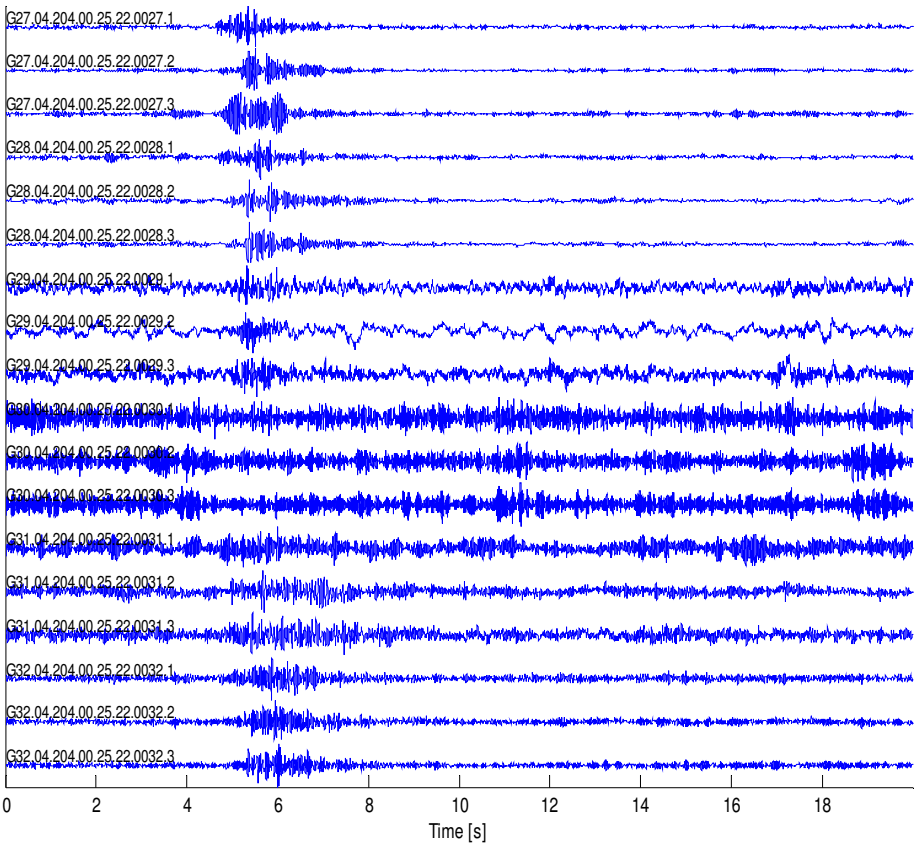

Figure 51: Raw data of one of the earthquake events by 6 seismometers.

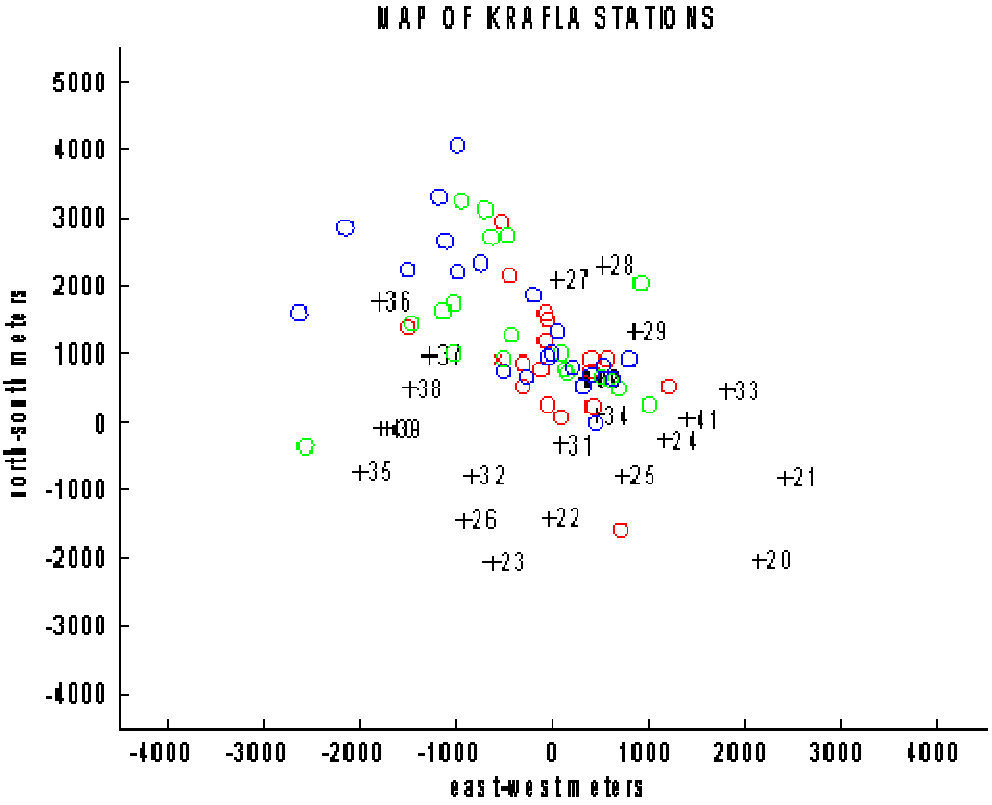

Figure 52: The locations of the epicenters and seismometer stations

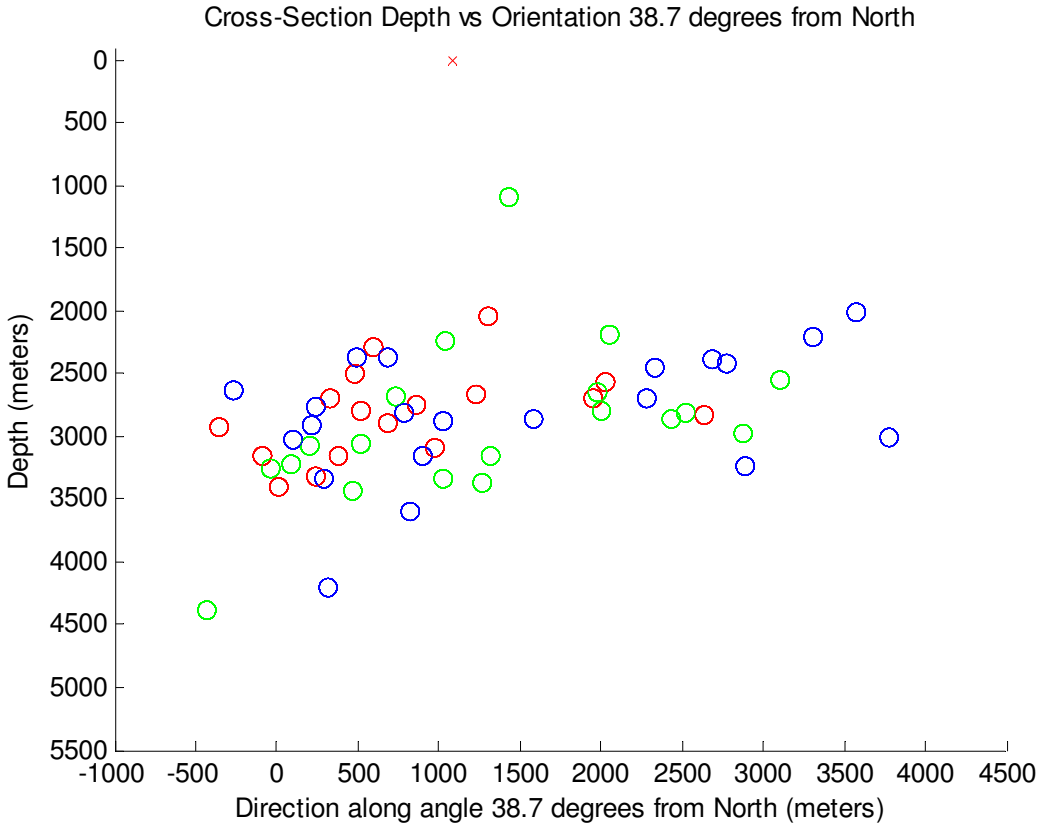

Figure 53: Cross-section of epicenter location
Cross-section of epicenter location along line rotated 38.7 degrees counterclockwise from due North. Red, green, and blue circles correspond to locations found during first third, second third and last third of collecting days, respectively.

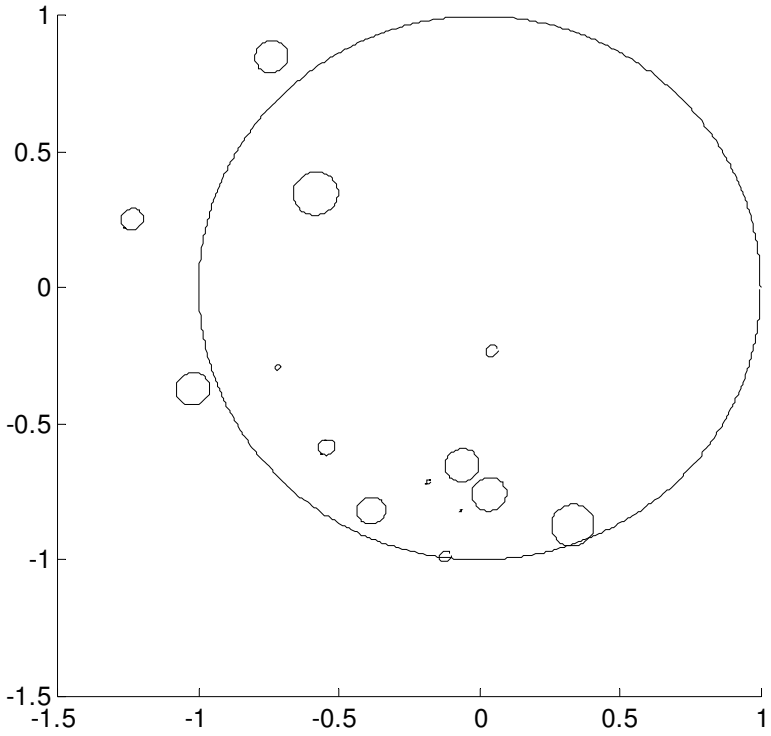

Figure 54: Equal-area projection of epicenter locations for station 28.
Large circle is the shear-wave window. The smaller circles are the epicenter locations showing the direction, angle with respect to the vertical, and (delay time)/ (distance to epicenter). The relative size of circle gives this scaled delay time.

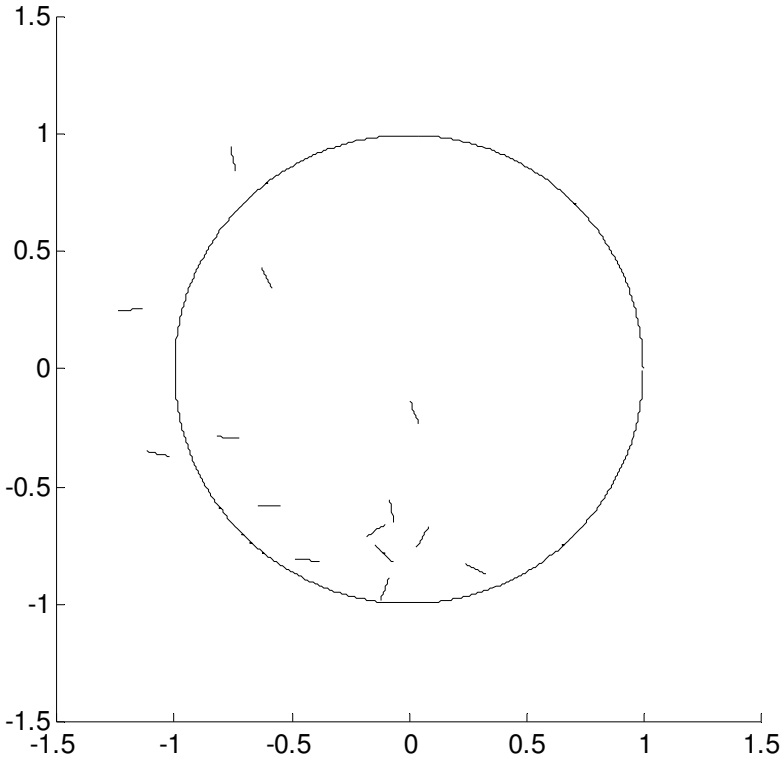

Figure 55: Equal-area projection of epicenter locations for station 28. Lines show the direction of the fast polarization.

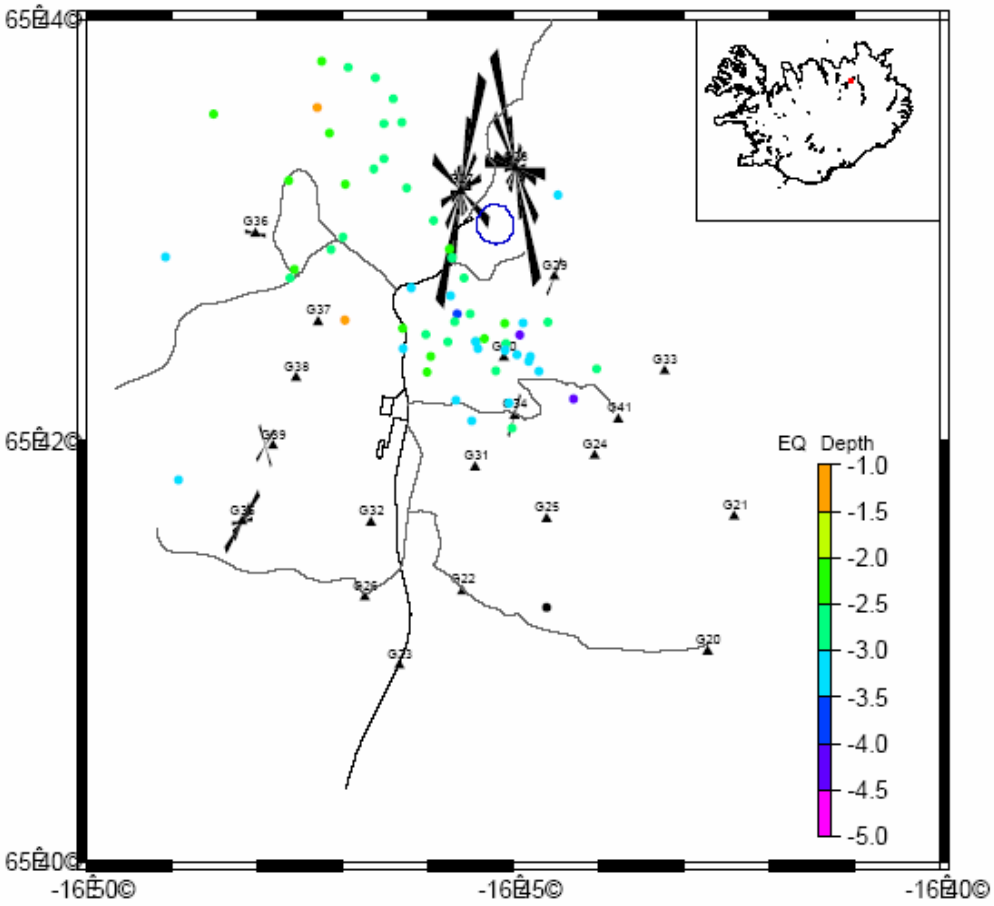

Figure 56: A set of rose diagrams
A set of rose diagrams (polar histograms) is shown superimposed on a map of the seismometer sites and epicenter locations organized by depth

A1.6 Conclusion

The Geospace GS-1 seismometers worked exceptionally well, with only minor time restraints due to weather. They proved to be durable under somewhat extreme conditions. Analysis of the data leads us to conclude that the devices are sensitive and accurate. From the acquired data the locations of the micro-earthquakes, the differential delay time between slow and fast shear-wave propagation, and the polarization of the

wave were determined. Work continues, using this data, to better understand the structure of the medium beneath the Krafla geothermal fields.

Appendix 2: Otterbach 2 - Sonde Design

The depth of 2700 meters at which the Otterbach 2 sonde had to be placed necessitated a different design. The constraints were that: (a) the device be capable of withstanding 5000 psi, that its outside diameter be 3 inches, and that the sensors operate at tilts of up to 8°.

In figure 57 the theoretical response of the HS-1 sensors is displayed.

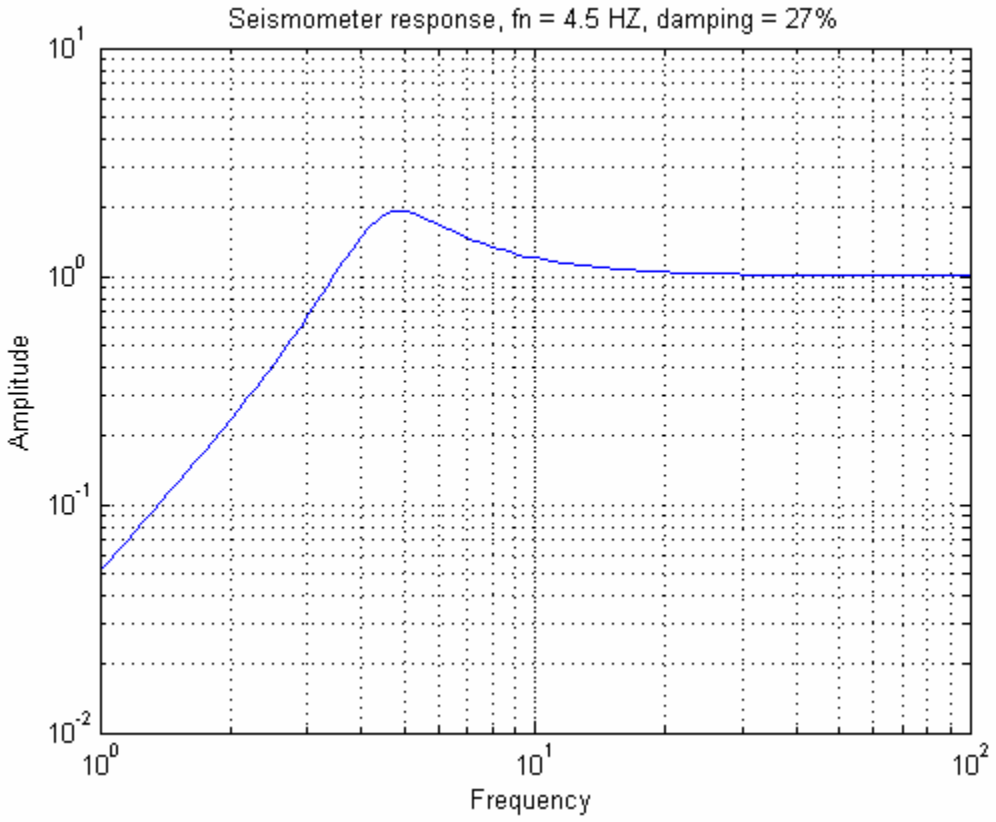

Figure 57: Theoretical response of HS-1 sensor in OT2
Theoretical response of HS-1 sensor in OT2 for resonant frequency 4.5Hz and a damping of 27%.

The theoretical response curve was generated from the formula

$$|T| = \frac{\omega^2}{\sqrt{\left(\omega_o^2 - \omega^2\right)^2 + 4h^2\omega_o^2\omega^2}} \qquad (1)$$

Where ω_o is the resonant frequency ($=2\pi f_o$), and h is the damping constant, which equals 0.27 in this case.

The birddog test of the geophone is shown below.

Birddog test of OT2

From:10-03-2006 00:00:0010-04-2006 23:59:59 SeismicSource GeoTest Report Current Geophone Type: HS-1 4.5 Hz

Comment:

TESTS PERFORMED AT LEAST ONCE: Frequency Damping Sensitivity Resistance Impedance Distortion Polarity

GEOPHONE TESTS RESULT: Tested = 15 Passed all selected Tests = 0 Failed at least one Test = 15

Tolerances ->			35%	25%	10%	10%	5%	0.5%	+	1,000K		
Rec#	Date	Time	Serial String		Fn	Bt	Gs	Res		Zts	Distort	Pol
	mm-dd-yyyy	hh:mm:ss	#		``SxP	`Hz	%	v/cv/cm/s		ohms	%	+/-
4	10-03-2006	18:12:59	OT2V	Single	4.22	29.27	0.582	2260		11815*	0.504*	+
5	10-03-2006	18:15:08	OT2H1	Single	4.42	28.38	0.568	2343		11994*	0.000	+
6	10-03-2006	18:16:22	OT2H2	Single	4.74	27.10	0.576	2438		12109*	0.650*	+
7	10-03-2006	18:19:03	OT2VE	Single	4.18	29.83	0.559*	2434		11672*	0.169	-*
8	10-03-2006	18:20:13	OT2H1E	Single	4.72	28.65	0.634	2398		11489*	0.695*	+
9	10-03-2006	18:21:15	OT2H2E	Single	4.49	26.72	0.591	2256		12607*	0.000	+
10	10-04-2006	14:37:22	OT2Vwel	Single	4.18	29.45	0.580	2264		11681*	0.424	+
11	10-04-2006	14:38:55	OT2HZ1w	Single	4.69	28.65	0.634	2385		11525*	0.387	+
12	10-04-2006	14:41:09	OT2HZ2w	Single	4.71	27.38	0.628	2290		12072*	0.855*	+
13	10-04-2006	14:45:17	OT2V10N	Single	4.21	29.34	0.582	2284		11749*	0.163	+
14	10-04-2006	14:48:22	OT2H110	Single	4.44	28.17	0.602	2280		11979*	0.000	+
15	10-04-2006	14:50:35	OT2H210	Single	4.73	27.53	0.629	2290		12068*	0.875*	+
16	10-04-2006	14:51:55	OT2H210	Single	4.53	26.71	0.579	2335		12595*	0.400	+
17	10-04-2006	14:52:55	OT2H110	Single	4.75	28.87	0.636	2382		11387*	0.350	+
18	10-04-2006	14:54:05	OT2V10E	Single	4.20	29.31	0.582	2292		11740*	0.287	+
	Specifications:				4.50	27.00	0.630	2500		13612		

Current Harmonic Distortion Drive Velocity 1.8cm/s

All 15 Records "> ...*" = Out of Tolerance

After welding

Vertical No tilt

10	10-04-2006	14:37:22	OT2Vwel	Single	4.18	29.45	0.580	2264		11681*	0.424	+

Vertical tilted N

13	10-04-2006	14:45:17	OT2V10N	Single	4.21	29.34	0.582	2284		11749*	0.163	+

Vertical tilted E

18	10-04-2006	14:54:05	OT2V10E	Single	4.20	29.31	0.582	2292		11740*	0.287	+

H1 No tilt

11	10-04-2006	14:38:55	OT2HZ1w	Single	4.69	28.65	0.634	2385		11525*	0.387	+

H1 rotated

17	10-04-2006	14:52:55	OT2H110	Single	4.75	28.87	0.636	2382		11387*	0.350	+

H1 tilted

14	10-04-2006	14:48:22	OT2H110	Single	4.44	28.17	0.602	2280		11979*	0.000	+

H2 No tilt

12	10-04-2006	14:41:09	OT2HZ2w	Single	4.71	27.38	0.628	2290		12072*	0.855*	+

H2 rotated

15	10-04-2006	14:50:35	OT2H210	Single	4.73	27.53	0.629	2290		12068*	0.875*	+

H2 tilted

16	10-04-2006	14:51:55	OT2H210	Single	4.53	26.71	0.579	2335		12595*	0.400	+

The design for the OT2 sonde are given in figures 58 through 61.

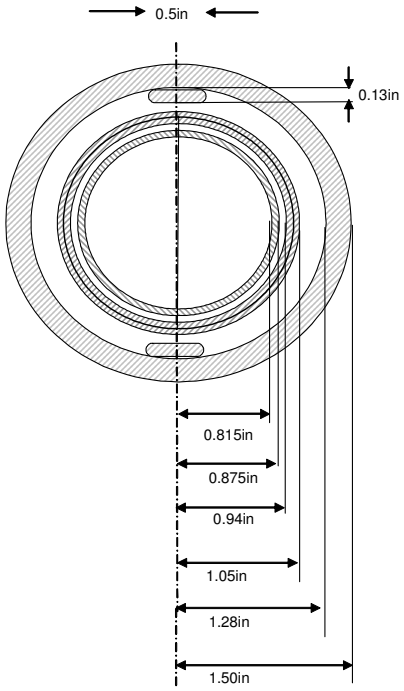

Figure 58: On axis view of housing for OT2 near end caps

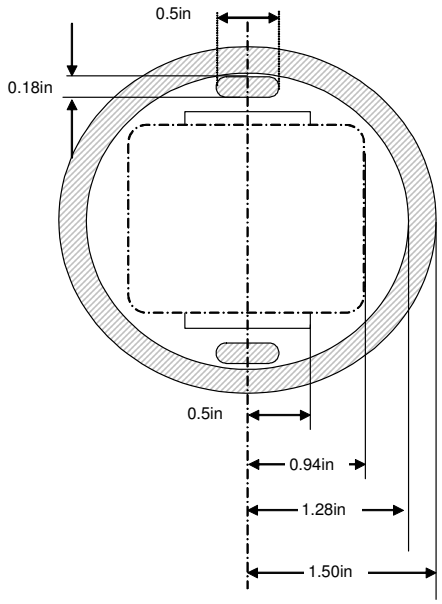

Figure 59: On-axis view of housing for OT2 in center section

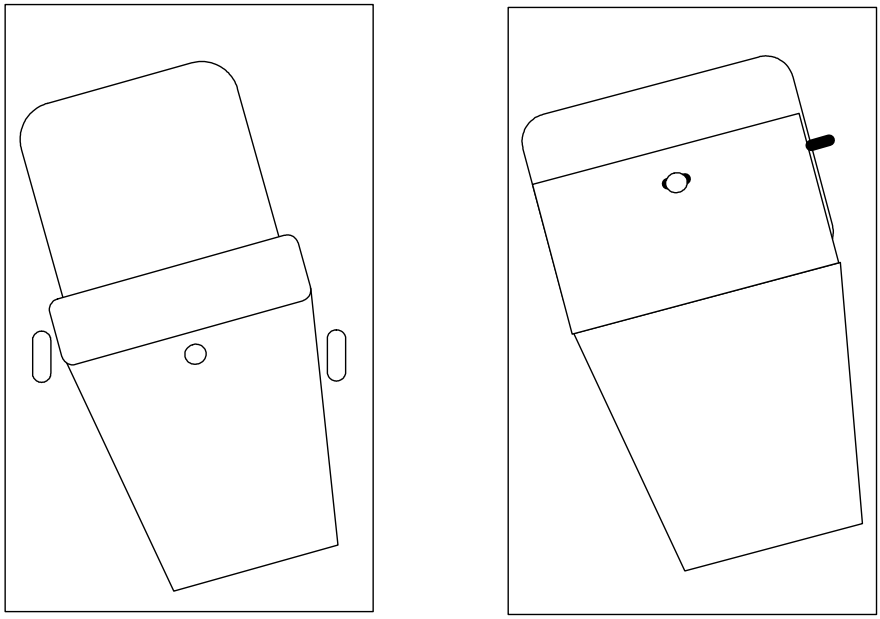

Figure 60: Tilt for sensor in OT2

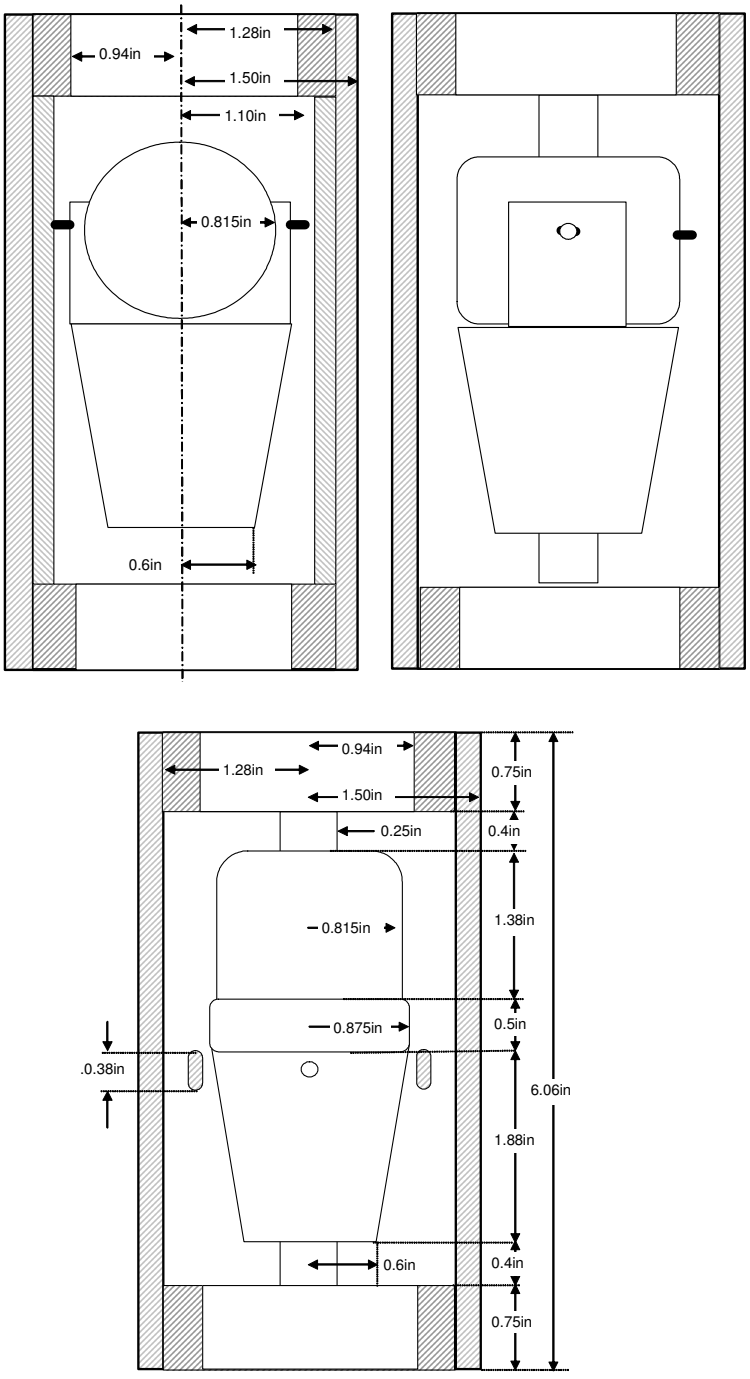

Figure 61: Longitudinal view of housing.

References

Abercrombie, R.E. 1995. Earthquake source scaling relationships from -1 to 5 M_L using seismograms recorded at 2.5-km depth. *J. Geophys. Res, 10*: 24015-24026.

Aki, K. 1972. The upper mantle techtonophysics, *Techtonophysics,13*: 423-446.

Aki, K. and P.G. Richards. 1980. Quantitative Seismology Theory and Methods. San Francisco: W. H. Freeman and Company. pp 557.

Archuleta, R. J., E. Crasnick, C Mueller, and P. Spudnich. 1982. Source parameters, of the 1980 Mammoth Lakes, California, earthquake sequence. *J. Geophys. Res., 87*: 4595-4607.

Arnott, S.K, and G. R. Foulger. 1994. The Krafla spreading segment, Iceland: Three-dimensional crustal structure and the spatial and temporal distribution of local earthquakes. *J.Geophys.Res, 99*:23825.

Boatwright, J. 1980. A spectral theory for circular seismic sources: simpleestimates of source dimension, dynamic stress drop and radiated energy. *Bull.Seismol.Soc.Am. 70*: 1-27.

Boatwright, J. and J. B. Fletcher. 1984. The partition of radiated seismic energy between P and S waves, *Bull.Seismol.Soc.Am. 74*: 361-376.

Bonjer, K.-P. 1997. Seismicity pattern and style of seismic faulting at the eastern borderfault of the southern Rhine Graben. *Tectonophysics 275*.

Booth, D. C. and S. Crampin. 1985. Modern Approaches in Geophysics10. *Seismic anisotropy in the Earth*:217. The Netherlands: Klower Academic Publishers.

Brandsdóttir, B., P. Einarsson, K. Árnason, and H. Kristmannsdóttir. 1994. Refraction measurements and seismic monitoring during an injection experiment at the Svartsengi geothermal field in 1993. Co-operative project of the University Science Institute, Orkustofnun and the Suðurnes District Heating Service on the envronmental impact of geothermal utilization (In Icelandic with English summary).
Orkustofnun OS94016/JHD-05 RH-3-94, 28p.

Brune, J.N. 1970. Tectonic stress and seismic shear wavesfrom earthquakes, *J. Geophys. Res.75*: 4997-5009.

Choy, G.L. and J.L. Boatwright. 1995. Global patterns of radiated seismic energy and apparent stress, *J. Geophys. Res. 100*: 18205-18228.

Courtillot,V., A.Davaille, J.Besse, and J. Stock. 2003. Three distinct types of hotspots in the Earth's mantle. *Earth Planet Sci. Lett*. 205:295-308. www.mantleplumes.org/WebDocuments/Courtillot2003.pdf

Crampin, S. 1981. A review of wave motion in anisotropic and cracked elastic media, *Wave Motion 3*:342-391.

Crampin, S. and S. Zatsepin, S. 1997. Modeling of the compliance of crustal rock-II. Response to temporal changes before an earthquake. *Geophysics J. Int. 129*:495-506.

Davis, S.D. and C. Frohlich. 1993. Did (or will) fluid injection cause earthquakes? - Criteria for rational assessment. *Seismological Research letters 64*: 207-224.

Du, Z.J. and G.R.Foulger. 1999. The crustal structure beneath the northwest fjords, Iceland, from receiver functions and surface waves. *Geophys. J.Int.139*:419-432.

Eshelby, J. D. 1957. The determination of the elastic field of an ellipsoidal inclusion and related problems, *Proc. R. Soc. London A, 241*:376-396.

Foulger, G.R., B.R. Julian, A. M. Pitt, D.P. Hill, P.E. Malin, and E. Shalev. 2003. Three-dimensional crustal structure of Long Valley caldera, California, and evidence for the migration of CO2 under Mammoth Mountain. *J Geophys. Res. 108*:2147.

Foulger, G.R., M.J. Pritchard, B.R. Julian. J.R. Evans, R. M. Allen. G. Nolet, W. J. Morgan, B.H.Bergsson, P. Erlendsson, S. Jakobsdottir, S. Ragnarsson, R. Steffansson, and K.S.Vogfjord. 2000. The seismic anomaly beneath Iceland extends down to the mantle transition and no deeper. *Geophys. J.Int.142*:F1-F5. (www.dur.ac.uk/g.r.foulger/offprints/transzone.pdf)

Foulger, G.R., M.J. Pritchard, B.R. Julian. J.R. Evans, R. M. Allen. G. Nolet, W. J. Morgan, B.H.Bergsson, P. Erlendsson, S. Jakobsdottir, S. Ragnarsson, R. Steffansson, and K.S.Vogfjord. 2001. Seismic tomaography shows that upwelling beneath Iceland is confined to the upper mantle. *Geophys. J. Int.146*:504-530. (www.dur.ac.uk/g.r.foulger/offprints/big.pdf)

Genmo, Z., C. Huaran, M. Shuquin, and Z. Deyuan. 1995. Research on Earthquakes Induced by Water Injection in China. *Pure & Applied Geophys.145*:59.

Guo, H. A., A. Lerner-Lam, and S.E. Hough. 1992. Empirical Greeen's function study of Loma Prieta aftershocks: Evidence for fault zone complexity (abstract), *Seismol. Res. Lett., 63*:76.

Hardebeck, J.L. and P. M. Shearer. 2002. A new method for determining first-motion focal mechanisms, *Bull. Seism. Soc. Am.92*: 2264-2276.

Hardebeck, J.L. and P. M. Shearer. 2003. Using S/P ratios to constrain the focal mechanisms of small earthquakes, *Bull. Seism. Soc. Am.93*: 2434-2444.

Haring, M.O. 2004. Deep heat mining: Development of a cogeneration plant from an enhanced geothermal system in Basel, Switzerland. *IGA News 58*. http://www.geothermie.de/iganews/no58/deep_heat_mining.htm

Haring, M. O., F. Ladner, U. Schanz, and T. Spillman. 2007. Deep heat mining Basel, preliminary results, European Geothermal Conference. http://www.geothermal.ch/downloads/dhm_egc300507.pdf

Healy, J. W. Rubey, D.Griggs, C Raleigh. 1968. Increasing fluid pressure along pr-existing fractures can cause a reduction of the effective normal stress and initiate the release of tectonic stress. *The Denver Earthquakes, Science 161*:1301-1310.

Holbrook, S.W., H.C. Larsen, J. Korenaga, T. Dahl-Jensen, I.D. Reid, P.B. Kelemen, J.R. Hopper, G.M. Kent, D. Lizzarralde, S. Berstein, S. and R.S. Detrick. 2001. Mantle structure and active upwelling during continental breakup in the North Atlantic. *Earth Planet. Sci. Lett.190*: 251-266.

Hubbert, M.K., and W.W. Rubey. 1959. Role of fluid pressure in mechanics of overthrust faulting, I. Mechanics of fluid-filled porous solids and its application to overthrust faulting. *Geol. Soc. America Bull. 70*:115-166.

Ide, S. and G.C. Beroza. 2001. Does apparent stress vary with earthquake size?, *Geophys. Res. Lett. 28* :3349-3352..

Ide, S., G.C. Beroza, S.G. Prejean and W. L. Ellsworth. 2003. Apparent break in earthquake scaling due to pathe and site effects in deep borehole recordings. *J. Geophys. Res.108(B5)*:2271.

Imanishi, K. and W.L. Ellsworth. 2006. Earthquakes: Radiated Energy and the Physics of Faulting . AGU Monograph 170. Edited by R. Abercrombie, A. McGarr, G. Di Toro and H. Kanamori.*Source scaling relationships of microearthquakes at Parkfield, CA, determined using the SAFOD pilot hole seismic array*.

Izutani, Y. and H. Kanamori. 2001. Scale-dependence of seismic energy-to-moment ratio for strike-slip earthquakes in Japan, *Geophys. Res. Lett. 28*:4007-4010.

Julian, B. R. and G. R. Foulger. 1996. Earthquake mechanisms from linear-programming inversion of seismic wave amplitudes, *Bull. Seism. Soc. Am.86*:972-980.

Julian, B.R., G.R. Foulger, K. Richards-Dinger. 2005. The Coso Geothermal area: A laboratory for advanced MEQ studies for geothermal monitoring. *http://www.dur.ac.uk/g.r.foulger/Offprints/PalmSprings.pdf*

Kanamori, H., and D.L. Anderson. 1975. Theoretical basis of some empirical relations in seismology, *Bull. Seism. Soc. Am. 65*:1073-1095.

Kanamori, H., E. Hauksson, L.K. Hutton, and L. M. Jones. 1993. Determination of earthquake energy release and ML using TERRAscope, *Bull. Seism. Soc. Am.* 83:330-346.

Kanamori, H. and T. H. Heaton. 2000. GeoComplexity and the Physics of Earthquakes. edited by J. B Rundle, D.L. Turcotte, and W. Klein. *Microscopic and macroscopic physics of earthquakes.* Washington, D.C.: AGU:147-163.

Keilis-Borok, V. I. 1960. Investigation of the mechanism of earthquakes, *Soviet Research in Geophysics (English Translation)* [4], American Geophysical Union, Consultants Bureau, New York:201.

Kisslinger, C. 1980. Evaluation of S to P amplitude ratios for determining focal mechanisms from regional network observations, *Bull. Seism. Soc. Am.70*: 999-1014.

Luis, J.F. 2007. Mirone: A multi-purpose tool for the explorating grid data. *Computers & Geosciences 33*: 31-41.

Madariaga, R.1976. Dynamics of an expanding circular fault, *Bull. Seism. Soc. Am.*:639-666.

Mayeda, K., and W.R. Walter. 1996. Moment, energy, stress drop, and source spectra of western United States earthquakes from region coda envelopes. *J. Geophys, Res.*101:11195-11208.

McGarr A.1999. On relating apparent stress to the stress causing earthquake fault slip, *J.Geophys. Res.104*:3003.

Medici, F. and L. Rybach. 1995. Geothermal map of Switzerland 1995(Heat Flow Density). *Materiaux pour la Geolologie de la Swisse de Geophysique*:35.

Meghraoui, M., B. Delouis, M. Ferry, D. Giardini, P. Huggenberger, I. Spottke, and M. Granet. 2001. Active Normal Faulting in the Upper Rhine Graben and Paleoseismic Identification of the 1356 Basel Earthquake. *Science 293*:2070-2073.

MIT-led Interdisciplinary Study, Tester, J. W., Chair, 2007. The future of geothermal energy: Impact of enhanced geothermal systems (EGS) on the United States in the 21st century. http://geothermal.inel.gov

Onacha, S., D. Kahn D., P. E. Malin, and E. Shalev,E. 2005. Resisitivity amd Microearthquake imaging of Krafla Geothermal Field, NE Iceland. *GRC*.

Ohtake, M. 1974. Seismic Activity Induced by Water Injection at Matsushiro, Japan, *J. Phys. Earth 22*:163.

Page, C.C. and M.A. Saunders. 1982. LSQR: an algorithm for sparse linear equations and sparse least squares. *ACM Transactions on Mathematical Software 8*:48-71.

Prejean, S.G. and W.L. Ellsworth. 2001. Observations of earthquake source parametersat 2km depth in the Long Valley Caldera, Eastern, California, *Bull. Seism. Soc. Am. 91*:165-177.

Rau, R.-J., F.T. Wu, and T.-C. Shin. 1996. Regionalnetwork focal mechanismdetermination using 3D velocity model and SH/P amplitude ratio, *Bull. Seism. Soc. Am.86*:1270-1283.

Reasenberg, P., and D. Oppenheimer, 1985. FPFIT, FPPLOT, and FPPAGE: FORTRAN computer programs for calculationg and displaying earthquake fault-plane solutions, *U.S.Geol. Surv. Open-File Rept109*: 85-739.

Reinecker, J., O. Heidbach, and B. Mueller, 2003. The 2003 release of the World Stress Map (available online at www.world-stress-map.org).

Richardson, E. and T. H. Jordan.2002. Seismicity in deep gold mines of south Africa: implications for tectonic earthquakes, *Bull. Seism. Soc. Am. 92*:1766-1782.

Roark, R. J. and W. C. Young. 1975. Formulas for Stress and Strain, 5th Edition. New York:McGraw-Hill. pp.624.

Ryerson, R., W. Walter, and K. Mayeda, 2003. Earthquake Energy Scaling Workshop. https://eed.llnl.gov/scaling-workshop/overview.php

Schaff, D.P., G.H.R.Bokelmann, W.L. Ellsworth, E. Zanzerkia, F. Waldhauser, and G. C. Beroza. 2004. Optimizing Correlation Techniques for Improved Earthquake Location. *Bull. Seismological Soc. Amer.94*:705-721.

Schulte-Theis Hartwig. 1995. Cluster Analysis and Location of Seismic Events Induced by Fluid Injection in the KTB-Borehole, Bavaria, Germany, EOS, *Trans. Am. Geophysical Union F559*.

Scherbaum, F.1996. Of Poles and Zeros: Fundamentals of Digital Seismology. The Netherlands: Kluwer Academic Publishers,.

Singh, S. K. and M. Ordaz. 1994. Seismic energy release in Mexican subduction zone earthquakes, *Bull. Seism. Soc. Am. 84*:1533-1550.

Stober, I., and K. Bucher. 2007. Hydraulic properties of the crystalline basement. *Hydrogeology 15*:213 - 224.

Tadokoro,K., Y. Kano, K. Nishigami, and T. Mizuno, T. 2001. Repeated water injection experiments at the Nojima fault zone, Japan: Induced earthquakes and temporal change in fault zone permeability. *Chikyu Monthly, 262*:264-267.

Tenzer, H. 2001. Development of Hot Dry Rock Technology*, GHC Bulletin*, December, 14-22.

Vassiliou, M.S. and H. Kanamori. 1982. The energy release in earthquakes, *Bull. Seism. Soc. Am., 72*:371-387.

Waldhauser, F. and W. L.Ellsworth. 2000. Double-difference Earthquake Location Algorithm: Method and Application to the Northern Hayward Fault, California*. Bull. Seismological Soc. Amer.90*:1353-1468.

Weidmann, M. 2002. Erdbeben in der Schweiz. Verlag Desertina, Chur.

Wyss, M. and J.N. Brune. 1968. Seismic moment, stress, and source dimensions for earthquakes in the California-Nevada region, *J. Geophys. Res. 73*:4681-4694.

Wu, Z.L. 2001. Scaling of apparent stress from broadband radiated energy catalogue and seismic catalogue and its focal dependence, *Earth Planets Space 53***:**943-948.

Biography

Daniel Scott Kahn was born in Charlottesville, Virginia and grew up in South Kingstown, Rhode Island. He graduated with high honors from South Kingstown High School in 1997. Dan attended Brown University and graduated with honors (Sc.B.) in May 2001, completing a concentration in Geology-Physics/Mathematics. His Senior Honors Thesis was titled: *El Nino Activity and the Production of Chlorophyll: A case study of phytoplankton production near the Southern Californian Coast, 1997-2000.* While at Brown, he was a University Teaching and Research Assistant (UTRA) and a Space Grant Award Recipient. He also interned at Williams Corporation in Tulsa, Oklahoma, where he worked on the Energy Trading Floor. From August 2001 to May 2004, Dan was a graduate student at Georgia Institute of Technology earning a Masters Degree from the School of Earth and Atmospheric Sciences under the supervision of Professor Daniel Lizarralde. His thesis was titled: *The Blake Ridge: A Study of Multichannel Seismic Reflection Data.* Since July 2004, Dan has been a graduate student at Duke University.